The role of *Wt1os* lncRNA in the pathogenesis of focal segmental glomerulosclerosis (FSGS) and podocyte biology

Doctoral thesis

for

the award of the doctoral degree

of the Faculty of Mathematics and Natural Sciences

of the University of Cologne

submitted by

Samantha Filipów

accepted in the year 2025

Reviewers:

Prof. Dr. Roman-Ulrich Müller

Prof. Dr. Niels Gehring

List of figures

List of tables

Abbreviations

AAV	ANCA-Associated Vasculitis
ACR	Albumin–Creatinine Ratio
ACTN4	Alpha-Actinin-4
ALH	Ascending Limb Of The Loop Of Henle
AMAP	Automatic Morphological Analysis Of Podocytes
BC	Bowman's Capsule
CCAT1-L	Colorectal Cancer Associated Transcript 1, Long Isoform
CD2AP	Cd2 Associated Protein
ceRNA	Competing Endogenous RNA
CNT	Connecting Tubule
COL4A	Collagen Type IV Alpha 4 Chain
CPF	Circulating Permeability Factor
DGE	Differential Gene Expression
DLH	Descending Limb Of The Loop Of Henle
DTU	Differential Transcript Usage
ESRD	End-Stage Renal Disease
FA	Focal Adhesion
FFPE	Formalin-Fixed Paraffin-Embedded
Firre	Functional Intergenic Repeating RNA Element
FP	Foot Processes
FSGS	Focal Segmental Glomerulosclerosis
FPKM	Fragments Per Kilobase Million
GAP	GTPase-accelerating protein
GBM	Glomerular Basement Membrane
GFR	Glomerular Filtration Rate
glomRNAseq	Glomerular RNAseq
GO	Gene Ontology
GPCR	G-protein-coupled receptor
GSEA	Gene Set Enrichment Analysis
H3K27ac	Histone H3 Lysine 27 Acetylation
HK-2	Human Kindey-2 Cells
HSMPs	Heat Sensitive Mouse Podocytes
HULC	Highly Up-Regulated In Liver Cancer
ICW	Co-Detection Workflow
IGV	Integrative Genomics Viewer
INF2	Inverted Formin 2
If	Intermediate Filament
IgAN	Iga Nephropathy
IL-4	Interleukin-4
IL-13	Interleukin-13
ILK	Integrin-Linked Kinase
IP3R	inositol-1,4,5-triphosphate receptor
IMCD	Inner Medullary Collecting Duct
lncRNA	Long Non-Coding RNA
ISH	In Situ Hybridization
kd	Knockdown
m7G	5'-End 7-Methyl Guanosine

MAGI	Membrane-Associated Guanylate Kinase
MAGI2	membrane-associated guanylate kinase inverted 2
MALAT1	Metastasis Associated Lung Adenocarcinoma Transcript 1
MCD	Minimal Change Disease
MN	Membranous Nephropathy
MMPs	Matrix Metalloproteinases
MT	Microtubules
ncRNA	Non-Coding RNA
NES	Normalized Enrichment Score
NDS	Normal Donkey Serum
NEAT1	Nuclear Paraspeckle Assembly Transcript 1
NKILA	NF-Kb Interacting Lncrna
NOS	Not Otherwise Specified
NPHS1	Nephrin
NPHS2	Podocin
OMCD	Outer Medullary Collecting Duct
PAS	Periodic Acid–Schiff
PCA	Principal Component Analysis
PC2	Second Principal Component
PEC	Parietal Epithelial Cell
PLC	Phosphoinositide phospholipase C
PPARγ	Peroxisome Proliferator–Activated Receptor Γ
RT-PCR	Reverse-Transcription Polymerase Chain Reaction
PTC	Proximal Tubules Convolute
ROS	reactive oxygen species
scRNA	Single Cell RNAseq
SD	Slit Diaphragm
sgRNA	Single guide RNA
siRNA	Small interfering RNA
SLE	Systemic Lupus Erythematosus
SPA	Synthetic Polyadenylation Site
STED	Stimulated Emission Depletion Microscopy
suPAR	Soluble Urokinase Plasminogen Activator Receptor
SYNPO	Synaptopodin
RGS1	Regulator of G-protein signaling
TARID	TCF21 Antisense RNA Inducing Promoter Demethylation
TNF-α	Tumor Necrosis Factor-Alpha
TRPC6	Transient Receptor Potential Canonical 6
TSS	Transcription Start Site
Tug1	Taurine-Upregulated Gene 1
uACR	Urinary Albumin–Creatinine Ratio
WT	Wild Type
WT1	Wilms' Tumor Suppressor 1
WT1-AS	Wt1 Antisense RNA
Wt1os	WT1 Transcription Factor, Opposite Strand
XIST	X-Inactive Specific Transcript
ZO-1	Zonula Occludens-1

Abstract

LncRNAs (long non-coding RNAs) are a diverse class of regulatory RNAs that influence gene expression by modulating chromatin activity, transcription, RNA splicing, and translation. Their dysregulation has been implicated in various human diseases, including cancer, neurological disorders, and kidney diseases. Previous studies have shown that the lncRNA Tug1 (taurine up-regulated gene 1) protects against podocyte loss by regulating PPARy (peroxisome proliferator–activated receptors) and mitochondrial function, while LOC105374325 overexpression induces an FSGS-like phenotype in mice. However, in general, studies on lncRNAs in the glomerulus remain limited, and their role in podocyte biology is largely unexplored.

Using RNAseq, we identified 241 lncRNAs associated with FSGS in mouse models, including *Wt1os*, an lncRNA which was significantly downregulated in several of the models. *Wt1os* is transcribed from a bidirectional promoter shared with *Wt1*, a gene encoding for a transcription factor essential for podocyte biology. *Wt1os* is conserved with its human orthologue, *WT1-AS*, in a syntenic manner. *WT1-AS* has been implicated in cancer biology, where it appears to regulate tumor growth, metastasis, and invasion. However, the role of *Wt1os*/*WT1-AS* in kidney physiology, FSGS and podocyte biology remains elusive.

Here, we shown that loss of *Wt1os* in mice led to podocyte foot process effacement and proteinuria. Transcriptomic analysis of glomeruli from *Wt1os*-deficient mice revealed significant gene expression changes. Gain-of-function experiments in cultured mouse podocytes, demonstrated that *Wt1os* localizes to the nucleus, has pro-migratory effect and regulated calcium signaling in a *Rgs1*-dependent manner. Using human podocyte cells, we confirmed the conserved nuclear localization of *WT1-AS* and, through loss-of-function experiments, demonstrated its crucial role in cell viability. *RGS1* is consistently downregulated upon loss of *Wt1os* across all cell culture models and in the mouse line, implicating its potential role as a downstream mediator of *Wt1os* in podocytes.

Our findings highlight *Wt1os* as a novel regulator of podocyte biology, making a substantial contribution to the limited knowledge on lncRNAs with a clear-cut implication in glomerular pathophysiology.

1. Introduction

1.1. Podocyte biology

1.1.1. Kidney: structure and function

The kidneys are paired excretory organs located in the retroperitoneum [1]. They play a crucial role in waste elimination and the regulation of whole-body homeostasis by maintaining blood pH and pressure, controlling extracellular fluid volume, and regulating fluid and electrolyte levels of the body [1,2]. Anatomically, the kidney is divided into three main parts: the cortex, medulla, and renal pelvis. Nephrons, which are the functional and structural units of the kidney, carry out its essential processes [1,2]. Healthy humans typically have about one million nephrons per kidney [3,4], while mice develop around 14,000 nephrons per kidney [3], each comprising a glomerulus and a tubular system [3] (Figure 1).

Actual filtration of the blood and generation of primary urine occurs in the glomeruli, located in the kidney cortex [1,2] . The resulting glomerular ultrafiltrate progresses to the proximal tubules, where ions, water, and nutrients are reabsorbed back into the bloodstream [1,2] . In the descending limb of the loop of Henle, water reabsorption occurs, while the ascending limb concentrates the filtrate further by reabsorbing sodium and chloride ions [1]. The distal convoluted tubules then reabsorb various ions, including sodium, chloride and calcium [5]. The filtrate is then processed into urine and expelled through the collecting duct, which regulates its volume and osmolality [1,2].

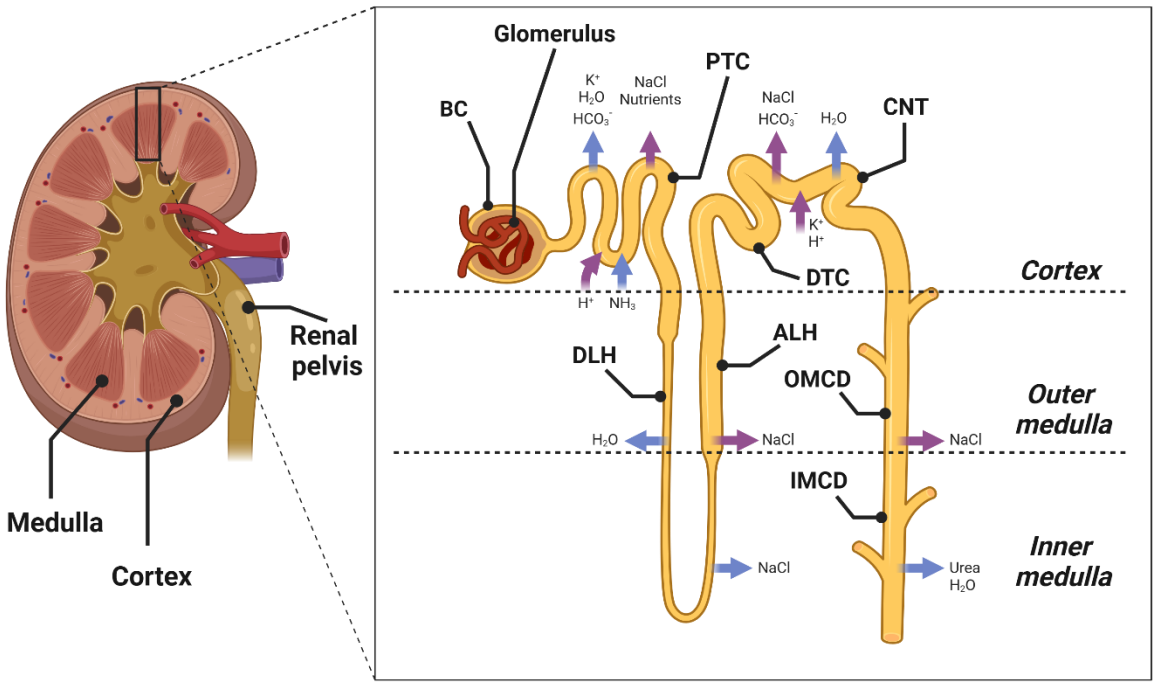

Figure 1. Representation of kidney and nephron structure.

The kidney is a complex organ consisting of the cortex, the medulla and the renal pelvis (left). A human kidney contains approximately one million nephrons, complex structural and functional units (right). Each nephron is made of a glomerulus with a Bowman's capsule (BC), proximal tubules convolute (PTC), descending limb of the loop of Henle (DLH), ascending limb of the loop of Henle (ALH), distal tubules convolute (DTC), connecting tubule (CNT), outer medullary collecting duct (OMCD), and inner medullary collecting duct (IMCD). Created with BioRender.com

1.1.2. Podocytes and their role in the glomerulus

In humans, each glomerular tuft is estimated to contain 500 to 600 podocytes [4], while adult mouse glomeruli have about 70 to 75 podocytes [6,7]. Podocytes are specialized, terminally differentiated visceral epithelial cells essential for maintaining the integrity of glomerular structure (**Figure 2 a**) [8,9]. Together with the glomerular basement membrane (GBM) and the fenestrated endothelium, podocytes form the permselective glomerular filtration barrier, a complex structure governing the kidney's filtration, a process that is critical for preventing the loss of plasma protein into the urine (**Figure 2 b**) [10]. Glomerular filtration occurs first through the fenestrated endothelium of the capillary wall, then the glomerular base membrane and the podocyte foot processes with the slit diaphragm (**Figure 2 b**) [8]. The process is driven by a hydrostatic pressure

gradient: the difference between the glomerular capillary pressure and Bowman's space pressure, opposed by the oncotic pressure of capillary plasma [11]. Podocytes wrap around the glomerular capillaries, playing a critical role in the filtration barrier of the kidney (**Figure 2 a**) [9,4]. These cells develop primary processes that branch into 20-40 secondary and tertiary foot processes (FP), which interdigitate with the foot processes of adjacent podocytes to form a complex network (**Figure 2 a**) [12]. Anchored firmly to the glomerular basement membrane (GBM) by integrins, dystroglycan, and podoplanin, podocytes contribute to the composition of the underlying GBM by secreting essential components such as laminin and type IV collagen, and by producing metalloproteinases (MMPs) involved in extracellular matrix remodeling (**Figure 2 b**) [8,13]. Thomas Benzing's biophysical model of glomerular ultrafiltration highlights the crucial role of podocytes foot processes in counteracting the glomerular capillary pressure, compressing the GBM, and therefore restricting its permeability and preventing albumin loss [11].

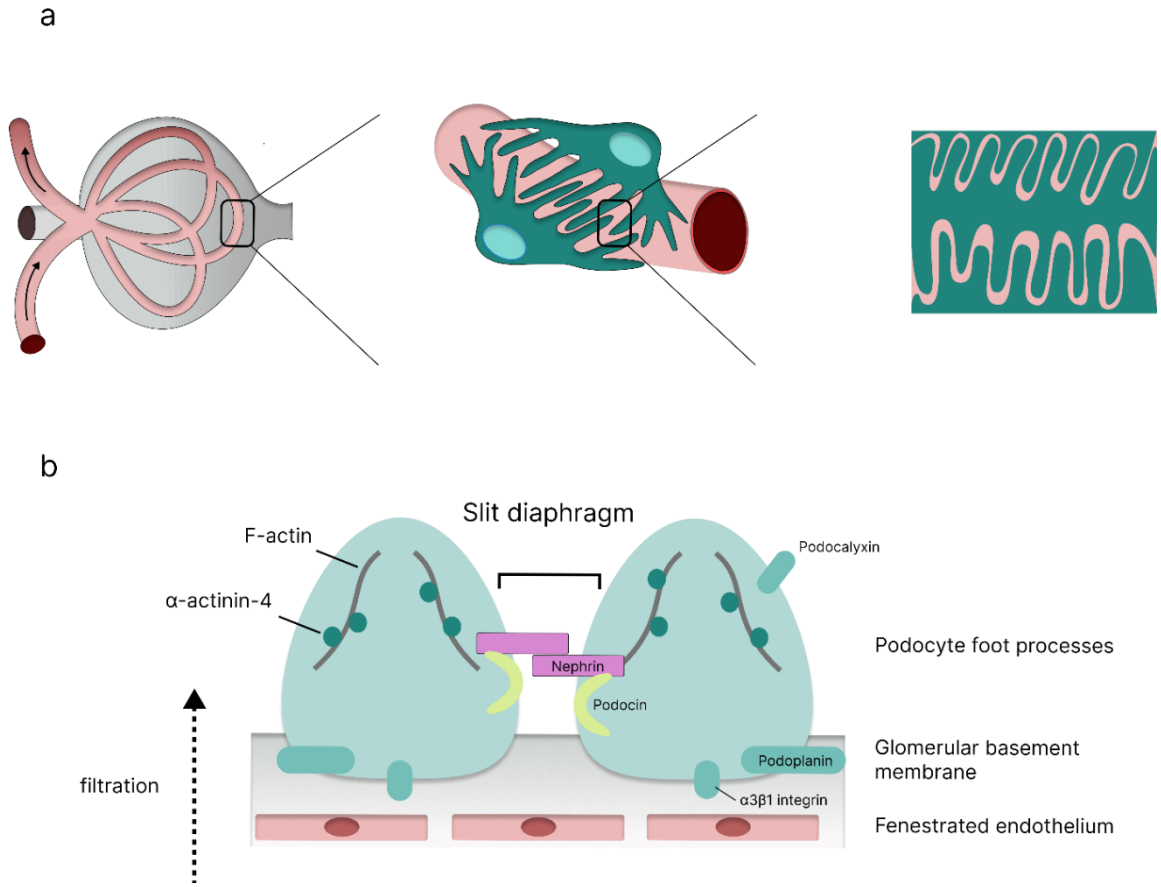

Figure 2. Schematic representation of podocytes and slit diaphragm structure.

a. The glomerulus contains a network of capillaries, forming a tuft located at the beginning of each nephron.

continued on next page

Podocytes wrap around the glomerular capillaries creating a complex network with their interdigitating primary and secondary foot processes. **b. The glomerular filtration occurs through the filtration barrier made of three layers: first through the fenestrated epithelium of the capillary wall, then the glomerular basement membrane and the podocyte foot processes with the slit diaphragm.** The dashed arrow indicates the direction of filtration. The podocytes are anchored to the GBM through various proteins, including integrins and podoplanin. The neighboring podocytes are interconnected by a structure known as the podocyte slit diaphragm (SD), a complex cell junction that links the foot processes of adjacent podocytes. The SD is comprised of multiple proteins, both on the extracellular and cytoplasmic sides. Key proteins depicted include nephrin and podocin. Nephrin forms zipper-like structures bridging the gap between neighboring cells. Podocin, on the other hand, adopts a hook-like configuration, with its transmembrane domain localized within lipid rafts. Additionally, the negatively charged podocalyxin on the surface of podocytes repels other proteins, further enhancing the efficiency of filtration process. Black dotty arrow indicates the direction of filtration. SD viewed perpendicular to the foot processes.

1.2. Slit diaphragm and cytoskeleton

1.2.1. Slit diaphragm

The slit diaphragm (SD) is a specialized 40 nm wide cell-cell junction located between the foot processes of neighboring podocytes [4,13,14]. This structure has a complex architecture, featuring an extensive network of associated proteins [15]. Several extracellular components, such as nephrin [16], NEPH1 [17], P-cadherin [18], FAT [19], and ephrin [20] have been identified as structural proteins that form the sieve of the SD. On the cytoplasmic side, proteins such as ZO-1 (Zonula occludens-1) [21], podocin [22], CD2AP (CD2 Associated Protein) [22], MAGI (Membrane-associated guanylate kinase) proteins, synaptopodin [23] and Par-complex molecules [24] facilitate interaction of the SD with the podocyte actin cytoskeleton [25].

The role of the SD extends beyond the structural functions as it has been demonstrated to act as an important antiapoptotic signaling platform [26,27]. Tyrosine phosphorylation of nephrin by Fyn kinase has been shown to stabilize the nephrin-podocin complex and initiate signal transduction in podocytes [28]. Subsequent research from Huber *et al.* demonstrated that nephrin and CD2AP activate PI3K (Phosphoinositide 3-kinase) and stimulate AKT activity leading to a reduction in apoptosis rates [29].

1.2.2. Cytoskeleton

Due to their complex architecture, podocytes rely on their dense cytoskeleton to construct the slit diaphragm (SD) and maintain its integrity, which is fundamental to their function [30,31]. The primary foot processes are predominantly composed of intermediate filaments (IFs) and microtubules (MT), whereas actin filaments are the main components of secondary foot processes [31]. These actin filaments are connected, with a range of linker proteins, to both the SD and the GBM meaning that the function of filtration barrier strongly relies on maintaining a highly ordered structure of the cytoskeleton [13].

At the interface with GBM, the cytoskeleton of the foot processes is anchored to the extracellular matrix through focal adhesion (FA) protein complexes, including talin1 and integrin-linked kinase (ILK) [32]. The podocyte cytoskeleton controls the cell's shape, adhesion, and plasticity, and it modulates active response to environmental stimuli [31]. The interaction between podocytes and GBM contributes to the regulation of capillary width and therefore has an impact on the glomerular filtration rate [26]. Cytoskeletal rearrangements leading to foot processes lengthening have been also demonstrated to be crucial in the adaptive stress response [33].

1.2. Podocytopathies

Glomerular disorders can generally be categorized into two groups: those confined to the kidneys, such as minimal change disease (MCD), primary and genetic focal segmental glomerulosclerosis (FSGS), and membranous nephropathy (MN), and those that are part of systemic conditions affecting multiple organs, like ANCA-associated vasculitis (AAV), diabetic nephropathy (DN) or systemic lupus erythematosus (SLE) [34,35]. The prevalence of these diseases varies with age [34]. For example, minimal change disease is the most common cause of nephrotic syndrome in children,[35] whereas MN and FSGS are more frequently seen in adults [36]. Podocytopathies refer to a group of kidney disorders where damage to the podocytes, either directly or indirectly, leads to proteinuria or nephrotic syndrome [4,8]. This podocyte damage can present with a variety of histological patterns in kidney biopsy samples of patients with nephrotic diseases, including FSGS, MCD, and MN[4,8]. Additionally, podocyte injury is also seen in nephritic conditions like IgA nephropathy (IgAN) and lupus nephritis (LN) [4]. Approximately 80% of proteinuric kidney diseases resulting from

glomerular injury have the potential to progress to kidney failure, leading to a renal replacement therapy [32]. FSGS, in particular, is a significant cause of nephrotic syndrome and is known for its varied clinical presentations and response to treatment [37].

1.2.1. Focal segmental glomerulosclerosis (FSGS)

FSGS describes a histopathological pattern of glomerular sclerosis associated with many proteinuric kidney diseases that share podocyte damage as a primary feature [9,38]. The term “focal” refers to the heterogeneous involvement of the glomeruli within the kidney cortex [8,39], while “segmental” indicates that only a fraction of the glomerulus is affected [37,39]. As the disease progresses, the damage can affect the entire glomerulus, eventually leading to global glomerulosclerosis and kidney failure [26]. Experimental data indicate that losing more than 20% of podocytes per glomerulus can trigger glomerulosclerosis [26]. A loss of more than 40% of the total podocyte population leads to an irreversible decline in renal function [26,40]. FSGS has been categorized into three main forms: genetic, secondary, and primary (often referred to as idiopathic) [39]. Mutations in podocyte genes (see Section: Pathogenesis of podocyte injury: Genetic causes of FSGS) and specific risk variants contribute to the genetic form of FSGS. This form is associated with diseases of varying severity, typically present in early childhood and often resistant to corticosteroid treatment [39]. Secondary FSGS can be either maladaptive, resulting from an increased stress on a reduced nephron number, caused by other non-glomerular diseases, associated with a viral infections or drug induced [39]. Primary FSGS, frequently referred to as idiopathic, is a type of chronic, progressive renal fibrosis with no identifiable cause [41]. The condition is presumably caused by an unknown circulating podocyte-toxic factor [39]. Primary FSGS is a leading cause of idiopathic nephrotic syndrome (iNS), and its often unclear origin makes diagnosis and treatment particularly challenging [39].

1.2.2. Pathogenesis of podocyte injury

Podocytes are postmitotic cells with a limited capacity to divide as they exit the cell cycle to stay in the G_0 phase [4,42]. Despite studies suggesting the trans-differentiation of parietal epithelial cells (PECs) into podocytes after glomerular injury, there is a lack of convincing evidence supporting the podocyte-replacement hypothesis [43]. The loss of podocytes can occur due to either cell death or detachment. However, studies have shown that podocytes are generally lost as viable cells in urine due to detachment from the glomerular basement membrane [26,44]. Numerous potential causes for podocyte injury have been identified, including podocyte gene mutations, metabolic and mechanical stressors, immunological mediators and viruses [8].

1.2.2.1. Genetic causes of podocyte injury

Since *NPHS1* (gene encoding nephrin), mutations were identified in 1998 as a causal factor for nephrotic syndrome, more than 60 genes have been implicated in the pathogenesis of podocyte diseases [8]. It is estimated that almost 100% of patients with congenital nephrotic syndrome carry a pathogenic mutation [45]. Mutations in genes encoding components of the SD, actin regulators or transcription factors have been associated with FSGS [8]. Mutations in *NPHS1* (nephrin), *NPHS2* (podocin) and *CD2AP* cause an autosomal recessive FSGS. In contrast, FSGS caused by mutations in *ACTN4* (Alpha-actinin-4), *TRPC6* (Transient Receptor Potential Canonical 6) or *INF2* (Inverted Formin 2) show an autosomal dominant pattern of inheritance [45]. In cases of early-onset FSGS, mutations in the podocin gene are the most prevalent, with the R138Q variant being commonly observed in European patients [45]. In adult-onset FSGS, the most common podocin polymorphism is R229Q [45,46].

A wide spectrum of renal manifestations as FSGS is caused by mutations in *WT1* (Wilm's tumor) gene [47]. The *WT1* gene encodes a transcription factor, which plays a crucial role in kidney development [48]. Although it was first described in the context of a childhood malignancy of the kidneys, the protein it encodes acts as a master regulator of gene expression in podocytes [48]. Genes encoding SD components (e.g. *NPHS1, NPHS2* or *MAGI2* encoding Membrane-associated guanylate kinase inverted 2), cytoskeleton regulators (e.g. *ACTN4* or *SYNPO* encoding protein synaptopodin), and adhesion-related proteins were identified as WT1 targets [49]. Mutations in exons 8 and 9 of the *WT1* gene can lead to nephrotic syndrome with FSGS, which typically

manifests within the first year of life [46]. In the study by Lipska *et al*., 90% of the patients with *WT1 a*ssociated glomerulopathy carried a mutation in the hotspot region of the *WT1* gene, with the highest number of mutations affecting the DNA-binding region [47]. The range of genetic mutations associated with FSGS highlights the complexity of podocyte biology and demonstrates how disruptions in cellular components and regulatory pathways can contribute to podocyte disease. Besides, research indicates that podocyte injury often results from a combination of genetic predisposition and environmental factors that lead to podocyte dysfunction [50].

1.2.2.2. Mechanical damage

Podocytes lining the GBM are continuously exposed to high physical forces and under normal conditions they need to withstand biomechanical stress to avoid detachment and loss into the urine [4]. The hydrostatic pressure gradient between the glomerular capillaries and the Bowman space surrounding the capillaries induces circumferential stress on the podocyte foot processes. The filtration of fluid through the glomerular barrier results in shear stress on the lateral surfaces of the foot processes. The lateral flow of filtrate across the podocyte cell body imposes additional shear stress [4]. High mechanical stress due to increased pressure affects the processes, podocyte cell body and SD protein complexes which may compromise the glomerular filtration barrier [4,33]. Work from Puelles and colleagues shown a direct correlation of podocyte depletion with hypertension and older age independently from kidney disease [51]. Sharma *et al.* demonstrated that physical stress leads to the release of fatty acids from podocyte membrane phospholipids, which in turn activates pro-inflammatory signaling [52]. Podocytes possess mechanosensing capabilities [53], and prolonged exposure to elevated biomechanical stress disrupts the organization of the actin cytoskeleton, resulting in the loss of stress fibers [52]. Any type of cell injury that causes podocyte loss further increases mechanical stress on the remaining podocytes [4].

1.2.2.3. Circulating permeability factors

Post kidney-transplant recurrence of primary FSGS suggests its pathogenesis to be associated with an unknown circulating factor, which selectively targets the filtration barrier inducing podocyte damage leading to increased permeability and proteinuria [4,54]. Despite extensive research, the exact nephrotoxic molecule remains unidentified. Studies pointed towards the potential role of immune cells, such as B cells, T cells and

the complement system. Several reports described changes in subsets of circulating T cells and cytokine profiles in patients with podocytopathies with interleukin-4 (IL-4) and interleukin-13 (IL-13) proposed as potential circulating permeability factors [55,56]. A case-control study by Youssef *et al.* reported elevated serum tumor necrosis factor-alpha (TNF-α) levels in patients with NS indicating that TNF-α may be a central pathogenic factor [57]. Furthermore, a few clinical studies demonstrated successful treatment of NS using anti-TNF-α antibodies [58,59]. Further, evidence suggests that soluble urokinase plasminogen activator receptor (suPAR) could be a promising circulating factor candidate [60]. In the study of Wei and colleagues suPAR serum levels were found elevated in two-thirds of patients with primary FSGS, but not in individuals with other glomerular conditions [61]. Additionally, uPAR knockout mice treated with the recombinant suPAR exhibited foot process effacement (FPE) and proteinuria [61]. Evidence for a circulating permeability factor is further supported by studies reporting remission of proteinuria following plasma exchange [62]. Recent studies highlighted the pathogenic role of autoantibodies against nephrin [63–65]. Antinephrin autoantibodies have been detected in plasma of patients with minimal change disease and FSGS [65]. Moreover, the antibodies level correlate with the disease activity and they were significantly decreased during remission [64]. Mice immunized with a recombinant antinephrin antibody exhibited podocyte injury and developed nephrotic syndrome [65]. The antibodies were shown to bind the slit diaphragm, resulting in altered nephrin signaling. [65].

1.2.3. Clinical manifestation of FSGS

Damage to podocytes significantly impairs the functionality of the glomerular filtration barrier, leading to protein leakage into the urine. The hallmark clinical feature of FSGS is proteinuria, which can develop suddenly and reach high levels, sometimes exceeding 20 g/day [39]. In kidney biopsy analysis, glomerular damage is observed under light microscopy as local scarring, which can present in various histological patterns [38,9]. Based on these patterns, in 2004 Fogo *et al.* proposed a classification of FSGS into five variants: cellular, collapsing, tip, perihilar, and not otherwise specified (NOS) [38]. At the cellular level, podocyte injury can be identified under transmission electron microscopy (TEM) or high-resolution immunofluorescence microscopy by assessing ultrastructural changes in the morphology of secondary foot processes [66].

The earliest indicator of podocyte damage is the simplification of foot processes termed foot process effacement (FPE) seen as shortening, widening and eventually loss of foot processes along with reduction of SD length [67]. FPE and podocyte hypertrophy by cell enlargement serve as adaptation responses to podocyte injury, reinforcing cell attachment to the GBM and ensuring its complete coverage [33].

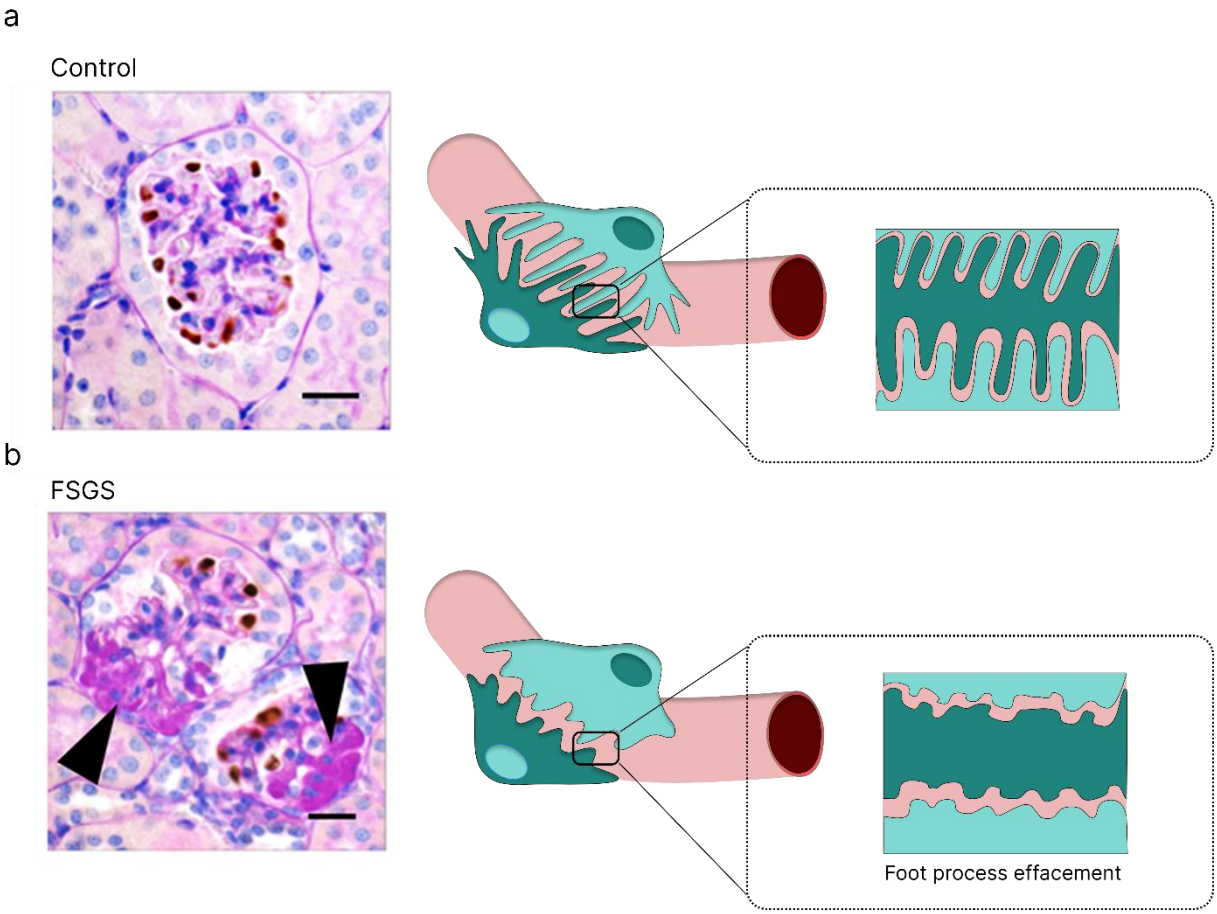

Figure 3. Structural changes in FSGS.

a. Representation of a healthy kidney tissue. On the left, a PAS staining of a mouse kidney tissue shows a healthy glomerulus, with brown immunohistochemistry staining of p57 indicating podocytes. The scheme on the right illustrates a healthy podocyte characterized by the presence of the interdigitating foot processes. **b. Representation of kidney tissue with the typical FSGS changes.** On the left, a PAS staining of a mouse kidney tissue shows glomeruli displaying FSGS lesions and scar tissue formation. The two black arrowheads indicate glomerulosclerosis. The diagram on the right depicts a podocyte with an altered morphology showing foot process effacement. Scale bars: 20 µm. Histology panels a and b adapted from Kawashima *et al*. [68].

1.2.4. Animal models of FSGS

To allow for studying FSGS, various animal models have been developed and many of them induce secondary forms of the disease [69]. Each model presents unique strengths and limitations in mimicking human FSGS. To advance research on idiopathic FSGS, an optimal animal model would need to develop the condition spontaneously and exhibit a slow progression to closely mimic the human form of primary FSGS [69]. Given that the primary cause of FSGS remains unknown, there is no standardized protocol for inducing this specific type of podocyte damage in animal models. To overcome this limitation, researchers typically rely on established agents and models that replicate the histological features of human disease. The following paragraphs will provide a detailed analysis of the advantages and disadvantages of selected mouse models used in FSGS research.

1.2.4.1. Genetic models

Podocin is a critical structural component of the SD where it interacts with nephrin to facilitate cellular signaling events [70,71]. Genetic mutations in the *NPHS2* gene, which encodes podocin, are known to cause nephrotic syndrome in patients. It has been demonstrated that a podocyte-specific podocin conditional knockout in adult mice results in proteinuria, hypercholesterolemia and hypertension. The progressive loss of podocin leads to renal failure and FSGS, similar to what is seen in patients [70]. To model the late onset of hereditary nephrotic syndrome with FSGS, Butt *et al.* utilized a compound-heterozygous $Pod^{R231Q/A286V}$ mouse line, which mimics the single-base-pair changes in the *NPHS2* gene observed in patients [71]. In this model, one allele carries an A286V change, resulting in the substitution of alanine with valine at position 286, corresponding to the p.A284V mutation (c.851C>T) in patients. The other allele carries an R231Q variant, leading to the exchange of arginine at position 231 with glutamine, mirroring the patient mutation p.R229Q (c.686G>A) [71]. These mice resemble the human genetic glomerular disease with progressive proteinuria from the second week, FPE and loss of podocytes by week 4, and pronounced FSGS lesions around week 8, ultimately resulting in kidney failure by 20 weeks of age [71]. Another gene targeted to study FSGS in animals is *WT1*. Wt1 protein is not only a master regulator of podocyte genes, but also an important transcription factor in kidney development. Since a complete knockout of *Wt1* is lethal, it is widely studied in heterozygosity [72]. Mice carrying a missense R394W point mutation (arginine to tryptophan as position 394) in

the *Wt1* gene serve as a murine FSGS model mirroring the situation in patients [72]. Heterozygous *Wt1*$^{+/R394W}$ males developed glomerulosclerosis accompanied with proteinuria at the age of 4 weeks [72]. The study of Menke and colleagues demonstrated that heterozygous whole-body *Wt1* knockout mice shown increased mortality, glomerulosclerosis with proteinuria, elevated urea and creatinine plasma levels and FPE [73].

1.2.4.2. Pharmacological models

Inducing glomerular disease through the administration of podocyte-toxic drugs is a classic method for studying FSGS [74]. Adriamycin (doxorubicin) and puromycin aminonucleoside (PAN) are the most commonly used drugs in this research field [69]. Adriamycin is an oncolytic antibiotic which intercalates DNA and inhibits macromolecular synthesis [69,74,75]. The drug can be administered intravenously to rats, mice, and zebrafish [75,76]. When injected into rats at a dose of 2 mg/kg with a 3-week interval between infusions, Adriamycin induces proteinuria starting from the second dose, leading to glomerulosclerosis after 16 weeks [69]. In mice, the require dosage varies depending on the strain and sex, ranging from 5.5 mg/kg for male BALB/c SCID mice, to 25 mg/kg for the highly resistant C57BL/c strain [75]. Adriamycin-treated animals exhibit excessive proteinuria, hypercholesterolemia, hypertension, and histological changes observed in human primary FSGS [74]. PAN is an antibiotic that prematurely terminates ribosomal protein translation. The drug induces massive proteinuria in rats within 10 days after administration after only a single injection at a dose of 50mg/kg. By week 18, rats exhibit FSGS lesions [74].

1.3. Long non-coding RNAs

1.3.1. General features and classification

Accumulating evidence over the last few decades revealed that more than half of the eukaryotic genome is transcribed into RNA [77]. With only 2% of DNA accounting for protein coding sequences, the genome gives rise to a large and heterogeneous class of non-coding RNAs (ncRNAs) [77]. The literature offers several methods to further divide non-coding RNAs (ncRNAs) into subgroups. A common classification system divides ncRNAs into two main categories: structural non-coding RNAs and regulatory non-coding RNAs [78]. Structural non-coding RNAs include ribosomal RNAs (rRNAs) and

transfer RNAs (tRNAs) [78]. The regulatory ncRNAs can be further categorized into small, medium, and long non-coding RNAs (lncRNAs) [78]. The latter have attracted significant attention due to their extensive range of actions and largely uncharacterized functions [79]. Structurally indistinguishable from coding transcripts, the first lncRNA gene *H19* was discovered in the 1980s in a large-scale sequencing of full-length murine cDNA libraries [80]. LncRNAs are defined by length of at least 200 nucleotides and the lack of protein-coding potential [81,82]. Similarly to protein coding genes their transcription is primarily mediated by RNA polymerase II, and most lncRNAs undergo co-transcriptional processing involving splicing, 5'-7-methylguanosine (m7G) capping, and 3'-end polyadenylation [77]. Increasing depth and sensitivity of RNA sequencing methods coupled with improved epigenetic technologies and *in silico* predictions, have begun to unravel unique features of lncRNAs, distinguishing them from mRNA [83]. Transcriptome-wide studies have shown that lncRNAs exhibit exceptional specificity to cell type, state, and disease, while being less evolutionary conserved and having lower expression levels than mRNAs [84]. Actively expressed lncRNA genes generally show a similar pattern of active histone modifications to the coding protein genes. However, it has been shown that lncRNA promoters are more enriched in the histone H3 Lysine 27 acetylation (H3K27ac) and they respond more strongly to the repressing chromatin remodeling complexes, such as Swr1 or Rsc [84]. The most common and intuitive classification of lncRNAs is based on their genomic location in relation to the nearby protein coding gene, subgrouping the class into intergenic, intronic, exonic, divergent and antisense RNAs [85]. A large fraction of annotated lncRNAs is under the regulation of bidirectional promoters and are divergently transcribed with a protein coding gene oriented in a head-to-head fashion [84,86]. A genome-wide analysis of cultured Neuro-2a cell line demonstrated shorter half-lives of lncRNAs in comparison to coding transcripts [87,88]. Moreover lncRNA stability seems to be related to its class, with intergenic, antisense and intronic lncRNAs being the least stable (half-life < 2h), and localization, with nuclear lncRNAs being less stable than cytoplasmic [87,89].

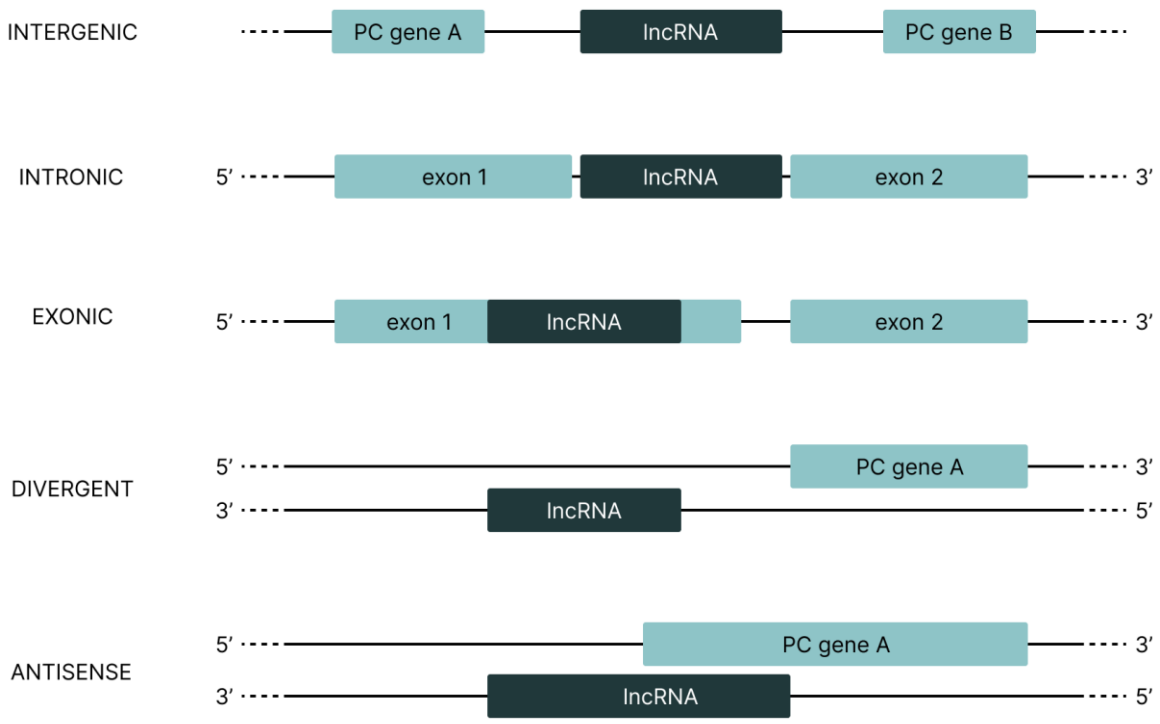

Figure 4. Classification of long non-coding RNAs.

Classification of lncRNAs based on their genomic location. Intergenic lncRNAs are positioned between two protein-coding genes, these lncRNAs can be transcribed in both sense and antisense direction. Intronic lncRNAs are located within an intron of a protein-coding gene, while exonic lncRNAs are positioned entirely within the exons. Divergent lncRNAs are found on the antisense strand relative to a protein-coding gene typically within 1 kb from the promoter region. The two genes are often under the regulation of the same promoter. Antisense lncRNAs are transcribed from the opposite strand of the protein-coding gene, partially or entirely overlapping with exons or introns of that gene. Protein-coding genes and their exons are depicted in light blue, lncRNAs are represented by the dark blue color.

1.3.2. Biological functions of lncRNAs

Although mammalian lncRNA genes significantly outnumber the protein-coding genes (over 100,000 annotated human lncRNAs vs. 20,000 protein-coding genes), only 1-5% have been functionally characterized [90,91]. LncRNAs can influence chromatin activity, control the formation and function of membraneless nuclear bodies, affect the stability and translation of cytoplasmic mRNAs, and disrupt signaling pathways based on their

subcellular localization and interactions with DNA, other RNA species, and proteins [89] [83,79].

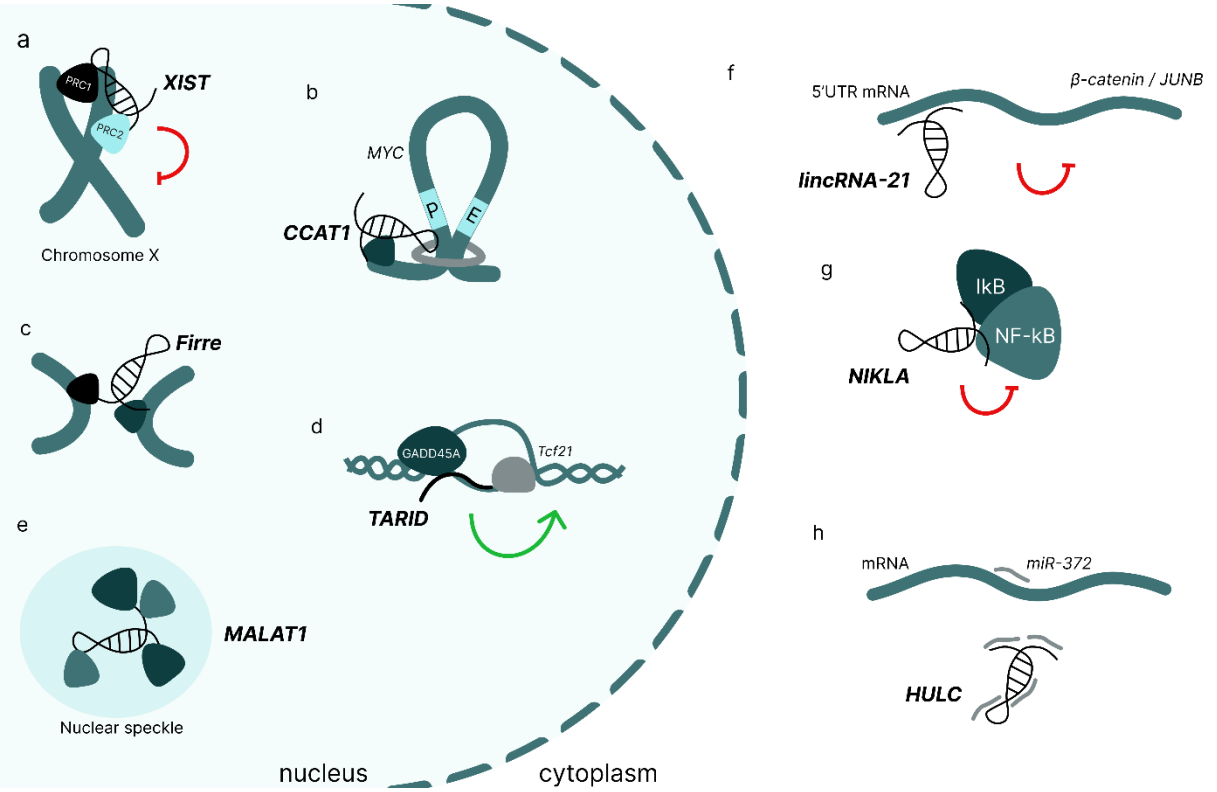

Figure 5. Functions of lncRNAs in the nucleus and cytoplasm.

Based on their cellular localization and interaction partners, lncRNAs can influence chromatin state (a-d), control the formation and function of nuclear speckles (e), affect the stability and translation of cytoplasmic mRNAs (f), impact protein modifications (g) and mRNA-miRNA interactions (h).

1.3.2.1. Nuclear lncRNAs

Nuclear lncRNAs were reported to be involved in multiple layers of gene expression regulation, including chromatin state modulation, facilitating transcription factor-DNA interactions or influencing splicing [92,93]. One of the mostly studied lncRNAs, *XIST* (X-inactive specific transcript), plays a major role in chromosome X inactivation through the interaction with cohesion and recruitment of polycomb complexes PRC1 and PCR2 to facilitate heterochromatin formation and gene silencing along the whole chromosome (**Figure 5**) [94]. ncRNAs have been reported to modulate inter- and intrachromosomal interactions [92]. *CCAT1*-L (colorectal cancer associated transcript 1, long isoform) regulates expression of *MYC* by facilitating intrachromatin loops

formation. The RNA accumulates in *cis* and enables the interaction between MYC promoters and enhancers (**Figure 5 b**) [95]. *Firre* (functional intergenic repeating RNA element) is a scaffold RNA acting in *trans* by modulating interchromosomal interactions. It was detected in five distant chromosomal regions and the studies suggest its function in their topological organization (**Figure 5 c**) [96]. Numerous studies demonstrated that nuclear localized long non-coding RNAs can affect transcription directly [92]. One way is through a local formation of R-loops, three-stranded RNA-DNA hybrids, which promote transcription factors recruitment to a promoter region [92]. A well-characterized example is *TARID* (TCF21 antisense RNA inducing promoter demethylation), an antisense lncRNA which creates an R-loop at the *TCF21* (Transcription factor 21) promoter leading to its demethylation and active transcription of the gene (

Figure 5 d) [97]. LncRNAs were also widely described to function at the post-transcriptional level [98]. *MALAT1* (metastasis associated lung adenocarcinoma transcript 1) is one of the most highly expressed genes in mouse and human [99]. The lncRNA encoded by *MALAT1* is localized to nuclear speckles and acts as a regulator of chromosome segregation during cell division [100]. A study by Tripathi *et al*., has shown the role of *MALAT1* in regulating the phosphorylation levels of serine/arginine (SR) splicing factors within the speckles suggesting its impact on alternative splicing (

Figure 5 e) [101].

1.3.2.2. Cytoplasmic lncRNAs

A large fraction of lncRNAs is exported to the cytosol where it functions in various modes of action regulating translation or protein modification. LncRNAs were observed to be bound to the ribosomes [102,103], residing in mitochondria [104], at the plasma membrane [105], and even secreted in exosomes [106]. One well-described cellular context in which lncRNAs play an important role is the modulation of translation. Huarte *et al.* demonstrated that *lincRNA*-21 can repress translation of β-catenin and JUNB by binding the mRNAs 3' and 5' untranslated regions (**Figure 5 f**). The RNA-mRNA complex enhances the interaction with translational repressors leading to the dissociation of ribosomes [107]. Another described mechanism of action is the modulation of cytoplasmic protein modifications by interaction with their functional domains. *NKILA* (NF-κB interacting lncRNA) was reported to play an important role in

the breast cancer metastasis suppression. *NKILA* directly interacts with NF-kB/IkB complex and masks its phosphorylation motifs (**Figure 5 g**). This inhibits IκB kinase phosphorylation and activation [108]. In the recent years, a new subgroup of cytoplasmic lncRNAs was identified: competing endogenous RNAs (ceRNAs). ceRNAs harbor multiple miRNA response elements and are able to regulate the protein coding transcripts indirectly by competing for miRNA binding. *HULC* (Highly Up-regulated in Liver Cancer), a lncRNA involved in tumorigenesis, was shown to sequester miR-372 and preventing it from binding and repressing translation of its target mRNA (**Figure 5 h**) [109].

1.3.3. lncRNAs in podocytes and glomerular diseases

To date, most research on lncRNAs in the field of glomerular diseases focuses on diabetic nephropathy (DN) [110,111]. Using a murine model of DN, Long *et al.* discovered that the lncRNA Tug1 (Taurine Up-Regulated 1) plays a protective role against podocyte loss. Their study demonstrated that Tug1 regulates the function of peroxisome proliferator-activated receptor γ (PPARγ) and mitochondrial oxygen consumption, mitochondrial reactive oxygen species (ROS), and mitochondrial complex activity. Furthermore, mice with podocyte-specific overexpression of Tug1 shown improvements in the histological features associated with DN [112]. In contrast, data on the function of lncRNAs in FSGS are limited. Non-diabetic patients with biopsy-confirmed FSGS demonstrated decreased levels of urinary Tug1 compared to healthy individuals. Additionally, its expression shown a positive correlation with mRNAs known to indicate podocyte loss, highlighting the potential of this lncRNA as a biomarker for podocytopathy [113]. Another lncRNA, LOC105375913 was significantly upregulated in the tubulointerstitial tissue of FSGS patients, with its level correlating with the fibrosis score [114]. Additionally, cell culture experiments demonstrated that overexpression of LOC105375913 in HK-2 (human kidney-2) cells induced the expression of fibrotic factors. This suggests that LOC105375913 lncRNA may be a key factor in promoting tubulointerstitial fibrosis [114 115]. In their work Hu *et al*. identified the lncRNA LOC105374325, which was found to be elevated in the biopsies of patients with FSGS. Overexpression of this lncRNA in mice led to proteinuria and an FSGS-like phenotype, and *in vitro* experiments suggested that LOC105374325 might contribute to podocyte injury by modulating the expression of apoptotic regulators [116]. Nuclear

paraspeckle assembly transcript 1 (NEAT1), another example of a pro-apoptotic lncRNA in podocytes, shown promotion podocyte injury by targeting miR-23b-3p/BNIP3L axis [117]. Research on CCAT1 lncRNA revealed that its expression levels are significantly lower in podocytes stimulated with TNF-α, indicating a role in podocyte viability by contributing to the inhibition of autophagy [118]. While these studies provide valuable insights, the role of lncRNAs in podocytes remains largely unknown. In particular, the contribution of lncRNAs to the pathomechanisms underlying FSGS remains unclear. Further research is crucial to fully understand their function and potential as therapeutic targets in glomerular diseases.

2. Thesis aims

The discovery of lncRNAs with their diverse functions had added a new layer of complexity to our molecular understanding of human disease [79,119]. Studies indicate that lncRNAs play a role in the pathogenesis of various disorders, including kidney diseases [112,114]. However, with only 5% functionally annotated lncRNAs, significant gaps still remain in our knowledge of lncRNA functions in podocytes, underscoring the need for further research to deepen our understanding of their role in the kidney function. Investigating *Wt1os* in podocytes may provide novel insights into FSGS pathophysiology and suggest new therapeutic strategies.

This thesis aims to identify the FSGS-associated lncRNAs and elucidate the role of the key candidate in podocytes biology by addressing the following objectives:

I. Identify the FSGS-associated lncRNAs

To determine lncRNAs associated with FSGS, we analyzed glomerular RNAseq data obtained from three different FSGS mouse models. We used two genetic models: $Wt1^{-/+}$ - heterozygous Wt1 deletion mutant and $Pod^{R231Q/A286V}$ - compound heterozygous *Nphs2* mutant. Adriamycin treated mice were used as a pharmacological FSGS model. Using the CALINCA pipeline, we identified 879 lncRNA transcripts from 757 genes that were podocyte-specific, and conserved between mice and humans. Within this group, we found 241 genes were differentially regulated in FSGS mouse models [120]. This part of the thesis has been published (DOI: 10.3390/cells10030692).

II. Define the function of *Wt1os in vivo*

Among the identified lncRNAs was *Wt1os*, transcribed from a gene with a bidirectional promoter shared with Wt1, a transcription factor crucial for podocyte function [72]. To investigate its role in kidney function and podocyte biology, we generated a novel $Wt1os^{-/-}$ mouse line. The transgenic animals were phenotyped with particular focus on glomerular function and podocyte morphology. Additionally, transcriptomic analysis of isolated glomeruli from $Wt1os^{-/-}$ mice was performed to identify differentially expressed genes (DEGs) following *Wt1os* loss of function.

III. Define the molecular function of *Wt1os*

To investigate the molecular function of *Wt1os*, we utilized both mouse and human cultured podocyte cell lines.

In mouse podocytes we employed the CRISPRa system to induce the *Wt1os* expression. We determined its subcellular localization and analyzed its impact on the expression of genes identified as DEGs in $Wt1os^{-/-}$ glomeruli. Furthermore, using a scratch assay, we assessed how *Wt1os* influences podocytes migration behavior.

In human podocytes, we performed a loss-of-function experiment using GapmeRs—mediated knockdown of *WT1-AS*, the human orthologue of *Wt1os*. We determined its

subcellular localization, evaluated the impact of *WT1-AS* loss on cell viability, and analyzed the expression levels of DEGs identified in the *Wt1os*$^{-/-}$ glomeruli.

3. Materials

3.1. Chemicals and Reagents

Table 1 List of chemicals and reagents used within this work.

Chemical / Reagent	**Product no.**	**Provider**
1-Thiglycerol	M1753-100ML	Sigma-Aldrich
Acetic acid	7332.1	Carl Roth
Acetonitrile	701881	AppliChem
Acrylamide	161-0140	BioRad
Agarose	A9539	Sigma-Aldrich
Albumin from mouse Serum	A3139	Sigma-Aldrich
Ammonium persulfate (APS)	A0834	AppliChem
Boric Acid	B0252-500G	Sigma-Aldrich
Bovine Serum Albumin (BSA)	1066	Gerbu
Blasticidine	Ant-bl-1	Invitrogen
Bromphenol Blue	A512	Carl Roth
Calcium chloride ($CaCl_2$)	HN04.2	Carl Roth
Citric acid monohydrate	27490	Fluka
D-fructose	M1753-100ML	Sigma-Aldrich
Dimethyl sulfoxide (DMSO) Hybri-Max	D2650	Sigma-Aldrich
Dithiothreitol (DTT)	6908.1	Carl Roth
DIYO-1	ABD-17580	Biomol
DMEM/F12	D6421	Sigma-Aldrich
DNase/RNase-Free Distilled Water	15657708	Thermo Fisher Scientific
dNTP Mix (10 mM each)	R0191	Thermo Fisher Scientific
Dulbecco's Modified Eagle Medium (DMEM)	D6429	Sigma-Aldrich
Ethanol (99.8%)	9065.3	Carl Roth
Ethidium bromide solution	2218.1	Carl Roth
Ethylenediaminetetraacetic acid (EDTA)	15575020	Thermo Fisher Scientific
Fetal Bovine Serum (FBS)	S 0115	Biochrom AG
Fluo-4, AM, cell permeant	F14217	Invitrogen
GeneRuler 1kb DNA Ladder	SM0311	Thermo Fisher Scientific
GeneRuler 50bp DNA Ladder	SM0372	Thermo Fisher Scientific
Glycerol	3783	Carl Roth
Heparin Natrium solution	15782698	Braun
HEPES	H0887	Sigma-Aldrich

Histomount	HS-103	National Diagnostics
Hoechst 33342 Solution (20 mM)	62249	Thermo Fisher Scientific
Hydrogen chloride (HCl)	T134	Carl Roth
Hydrogen Peroxide (H_2O_2) 30%	107209	Merck
Isopropanol	5752.3	Carl Roth
LB Medium	X964.2	Carl Roth
LB-Agar	X965.1	Carl Roth
Lipofectamine RNAiMAX	13778100	Thermo Fisher Scientific
Luer-Lock syringe Lok 20ml	300629	BD-Luer
Luminol	9253	Fluka
Magnesium chloride ($MgCl_2$)	1.05833.0250	Merck
Methanol	4627.5	Carl Roth
Meyer's hematoxylin solution	A0884	AppliChem
Magnesium sulphate heptahydrate ($MgSO_4$)	P027.2	Carl Roth
N,N,N´,N´-tetramethylethylenediamine (TEMED)	2367.3	Carl Roth
Normal Donkey Serum (NDS)	017-000-121	Dianova
Opti-MEM	31985-047	Thermo Fisher Scientific
PageRuler Plus Protein Ladder	26620	Fermentas
Paraplast Plus	39502004	VWR
Paraformaldehyde (PFA)	P6148	Sigma-Aldrich
Polybrene 1000x		
Periodic acid (99%)	3257	Carl Roth
Phenylmethylsulfonyl fluoride (PMSF)	A0999	AppliChem
Phosphate buffered saline	15374875	Thermo Fisher Scientific
Pluronic® F-127	P2443	Sigma-Aldrich
Polybrene	TR-1003-G	Sigma-Aldrich
Potassium chloride	6781.1	Carl Roth
ProLong™ Gold Antifade Mountant	P36930	Thermo Fisher Scientific
Protease Inhibitor Cocktail III	539134-1ML	Merck
PVDF filter 0.45 µm	P667.1	Carl Roth
Schiff's reagent	1.090.330.500	VWR
Sodium chloride (NaCl)	3957.1	Carl Roth
Sodium deoycholate	D6750	Sigma-Aldrich
Sodium dodecyl sulfate (SDS) pellets	CN30.3	Carl Roth
Sodium dodecyl sulfate (SDS) powder	L3771-500G	Sigma-Aldrich
Sodium fluoride (NaF)	S1504	Sigma-Aldrich
Sodium hydrogen phosphate (Na_2HPO_4)	S9390	Sigma-Aldrich
Sodium hydroxide (NaOH)	A3910.1000	AppliChem
Sodium orthovanadate (Na_3VO_4)	S6508	Sigma-Aldrich

TaqMan™ Universal PCR Master Mix	4304437	Thermo Fisher Scientific
Tetrasodium pyrophosphate ($Na_4P_2O_7$)	106591	Merck
TRI Reagent®	T3934-200ML	Sigma-Aldrich
Tris Hydrochloride (Tris-HCL)	9090.3	Carl Roth
TritonX-100	3051.2	Carl Roth
TriTrack DNA Loading Dye (6X)	R1161	Thermo Fisher Scientific
Trizma base	T1503	Sigma-Aldrich
Trypsin-EDTA Solution (1X), cell culture	T3924	Sigma-Aldrich
Tryptone	1010817	MP Biomedicals
Tween20	3472	Caesar & Loretz
VA-044 initiator	017-19362	Nordic Biolabs (Wako)
VECTASTAIN® Elite® ABC-HRP	PK-7100	Vector laboratories
Xylene	371.5	Th. Geyer
Yeast Extract	2363.1	Carl Roth

3.2. Assays and Kits

Table 2 List of kits and assays used within this work.

Assay / Kit	**Product no.**	**Provider**
Avidin/Biotin Blocking Kit	SP-2001	Vector laboratories
Creatinine (urinary) Colorimetric Assay Kit	500701	Cayman
Dako Liquid DAB+ Substrate Chromogen System	K3468	Dako
Direct-zol RNA Miniprep Kit	R2052	Zymo Research
GeneJet Gel Extraction Kit	K0692	Thermo Fisher Scientific
GeneJet Plasmid Miniprep Kit	K0503	Thermo Fisher Scientific
High-Capacity cDNA Reverse Transcription Kit	4368814	Applied Biosystems
High-Performance GoTaq® G2 DNA Polymerase with Mg-Free Buffer System	M7801	Promega
Opal™ 520 Reagent Pack	FP1487001KT	Akoya Biosciences
PCR Mycoplasma Test Kit I/C	PK-CA91-1096	PromoKine
Qubit™Broad Range (BR) Assay Kit	Q10211	Thermo Fisher Scientific
Quick-DNA Miniprep Plus Kit	D4069	Zymo Research
RNA Clean & Concentrator-5 (DNase not Included)	R1016	Zymo Research
RNA-Protein Co-Detection Ancillary kit	323180	ACD
RNAscope® H_2O_2 and Protease Reagents	322381	ACD

RNAscope® 2.5 HD Detection Reagents-RED	322360	ACD
RNAscope® Multiplex Fluorescent Reagent Kit v2	323100	ACD
RNAscope® Multiplex TSA Buffer	322809	ACD
RNAscope® 50X Wash Buffer	310091	ACD
SuperSignal West Femto Chemiluminescent Substrate	34095	Thermo Fisher Scientific
VECTASTAIN® Elite® ABC-HRP kit	PK-4000	Vector laboratories

3.3. Buffers and solutions

Table 3 List of buffers and solutions used within this work.

Buffer / Solution	**Composition**
Base solution (50x)	12.5 ml NaOH (5N) 1 ml EDTA (0.5 M) 36.5 ml ddH_2O
Blocking solution	50 mMTris 0.14 m NaCl 0.05% Tween-20 pH 8.0
Citric acid buffer (10x)	87.4 mM $Na_3C_6H_5O_7$ 12.6 mM citric acid monohydrate pH 6
Clearing solution	12.36 g Boric acid 40 g Sodium Dodecyl Sulfate (SDS) Fill up to 1 l with dH_2O Set pH to 8.5 using NaOH
Coating buffer	0.05 M carbonate-bicarbonate pH 9.6
Digestion Solution	1 mg/mL Worthington Collagenase Type II 0.75 mg/mL Pronase E (Sigma-Aldrich P6911) DNase I 100 U mL–1 In 1x HBSS
Diluent buffer	50 mM Tris 0.14 M NaCl 0.05% w/v Tween-20 1% w/v BSA pH 8.0
Enhanced Chemiluminescence Solution (ECL)	100 mM Tris (pH 8.5) 1.25 mM Luminol 0.2 mM Coumaric acid 0.75% (vol/vol) H_2O_2 pH 8.5
HBSS	5.4 mM KCl 0.3 mM Na2HPO4

	0.4 mM KH2PO4 4.2 mM NaHCO3 137 mM NaCl 5.6 mM d-glucose 1.3 mM CaCl2 0.5 mM MgCl2 0.6 mM MgSO4
Hydrogel solution	100 mM Tris (pH 8.5) 1.25 mM Luminol 0.2 mM Coumaric acid 0.75% (vol/vol) H_2O_2
Laemmli (5x)	62.5 mM Tris pH 6.8 10% (wt/vol) Glycerole 2% SDS 50 mM DTT Bromphenolblue
Modified RIPA buffer	10 mM Tris, pH 8 1 mM EDTA 0.5 mM EGTA 1 % Triton-X100 0.1% Sodiumdeoxycholate 44 µg/µl PMSF 2 mM Na3VO4
Neutralization solution (50x)	15.75 g Tris-HCl in 50 mL of H_2O
PBT-X	0.1 % Triton X-100 in PBS
Phosphate Buffered Saline (PBS)	137 mM NaCl 2.7 mM KCl 10 mM Na_2HPO_4 2 mM KH_2PO_4
Protein wash buffer	30 mM Tris 300 mM NaCl 0.3% Tween20 pH 7.5
Ringer's buffer	115 mM NaCl 0.4 mM KH_2PO_4 1.6 mM $K_2HPO_4 \cdot 3\ H_2O$ 5 mM glucose 1 mM $MgCl_2 \cdot 6\ H_2O$ 5 mM HEPES 25 mM Na-Gluconat 3 mM Ca-Gluconat $\cdot$ 1 H_2O pH 7.4
SDS-PAGE running buffer	25 mM Trizma base 192 mM Glycine

	0.1% (wt/vol) SDS pH 8.3
Saturated Fructose Solution	20.25g Fructose 100 µl 1- thioglycerol 5 ml H_2O
Separating gel buffer	750 mM Tris 10% (vol/vol) PAA 0.2% (wt/vol) SDS pH 8.8
SOC medium	2% (wt/vol) Tryptone 0.5% (wt/vol) Yeast Extract 8.6 mM NaCl 2.5 mM KCl 20 mM $MgSO_4$ 20 mM Glucose
Stacking gel buffer	250 mM Tris 5% (vol/vol) PAA 0.2% (wt/vol) SDS pH 6.8
Stop solution	0.18 M sulfuric acid
Substrate solution	100 µg/ ml TMB 48 mM sodium acetate 0.01% (vol/vol) H_2O_2 pH 5.2
TAE buffer (1x)	40 mM Tris (pH 8.5) 20 mM Acetic Acid 1mM EDTA
Tris Buffered Saline (TBS) (20x)	300 mM Tris-HCl 92.5 mM Tris Base 3 M NaCl pH 7.6
Transfer buffer	25 mM Tris 188 mM Glycine 20% methanol 0.1% (wt/vol) SDS pH 8.3
Tris-EDTA buffer (10x)	100 mM Tris Base 12.7 mM EDTA 0.05% Tween-20 pH 9
Wash solution	50 mM Tris 0.14 M NaCl 0.05% Tween-20 pH 8.0

3.4. Oligonucleotides

Table 4 List of oligonucleotides used within this work.

Name	Sequence 5'→ 3'	Application
Wt1os F	attgtacttctttcctgtggtggg	Genotyping PCR
Wt1os R	acttcctccctaaccttcaagtg	Genotyping PCR

Table 5 List of Taqman assays used for qPCR.

Gene	Taqman assay ID	Provider
hHPRT	Hs.PT.58v.45621572	IDT
mHPRT	Mm.PT.39a.22214828	IDT
hRGS1	Hs.PT.58.4402257	IDT
mRgs1	Mm.PT.58.10210812	IDT
mWt1	Hs.PT.58.22879267	IDT
hWT1	Mm.PT.58.31523371	IDT

Table 6 List of CRISPR components for *Wt1os*$^{-/-}$ mouse line generation.

Name	Sequence 5'→ 3'
crRNA	atgcagggatttgtacaagc(tgg)
ssODN repair template	g*t*tgtgtaaactcactgttgcaggttgggaaggcgagtcagtgggcagcattcccatctcca gctccccctcccccgactcgattgtacgtgaagctccccctcccccgatcaagcacacaaaa aaccaacacacagatctaatgaaaataaagatcttttatttgtacaaatccctgcatcccatctc cagccctgc*c*g

* = phosphorothioate bonds

Table 7 List of sgRNAs used for CRISPRa.

Name	Sequence 5'→ 3'	Provider
*Wt1os*_1	mA*mG*mU*rCrCrArGrGrArUrCrGrCrGrGrCrGrArGrGr GrUrUrUrUrArGrArGrCrUrArGrArArArUrArGrCrArArGr UrUrArArArArUrArArGrGrCrUrArGrUrCrCrGrUrUrArUr CrArArCrUrUrGrArArArArArGrUrGrGrCrArCrCrGrArGr UrCrGrGrUrGrCmU*mU*mU*rU	IDT
*Wt1os*_2	mA*mA*mG*rCrCrGrGrCrUrCrCrUrGrCrGrArCrArGrGr GrUrUrUrUrArGrArGrCrUrArGrArArArUrArGrCrArArGr UrUrArArArArUrArArGrGrCrUrArGrUrCrCrGrUrUrArUr CrArArCrUrUrGrArArArArArGrUrGrGrCrArCrCrGrArGr UrCrGrGrUrGrCmU*mU*mU*rU	IDT

Nontargeting control sgRNA	Product no. U-009501-01-02	Dharmacon

* = 2′-O-methylation of RNA bases

Table 8 List of oligonucleotides used for knockdown.

Name	Product No.	Type	Provider
WT1AS-201	LG00848364-DDA	GapmeR	Qiagen
WT1AS-210	LG00844250-DDA	GapmeR	Qiagen
Negative control	LG00000002-DDA	GapmeR	Qiagen
RGS1	L-044134-00-0005	siRNA	Dharmacon
Scramble control	U-009501-01-02	siRNA	Dharmacon

Table 9 List of probes used for RNAscope.

Name	Product No.	Provider
RNAscope™ Positive Control - Mm-Ppib-C3	313911-C3	ACD
RNAscope™ Negative Control Probe - DapB-C3	310043-C3	ACD
RNAscope™ Positive Control Probe - Hs-POLR2A-C3	310451-C3	ACD
RNAscope® Probe - Hs-WT1-AS	560781	ACD
RNAscope® Probe - Mm-*Wt1os*	577401	ACD

3.5. Plasmids

Table 10 List of plasmids used within this work.

Name	Vector	Provider
plenti dCAS-VP64_Blast	pLenti	Addgene #61425
pMD2 vsv g	pMD	Addgene #8454
pMDL g/p	pMD	Addgene #12251
pRSV rev	pRSV	Addgene #12253

3.6. Cell lines

Table 11 List of cell lines used within this work.

Name	Species
HSMPs	mouse
HSMPs.dCas9.VP64	mouse
AB8	human
AB8.dCas9.VP64	human
HEK293T	human

Table 12 The composition of cell culture media.

Cell line	Component	Amount	
HSMPs HSMPs.dCas9.VP64 (mouse podocytes)	RPMI-1640 medium		
	fetal bovine serum	10	%
	HEPES buffer	20	mM
	IFN-δ	0.25	µl/ml
AB8 (human podocytes)	RPMI-1640 medium		
	fetal bovine serum	10	%
	Insulin-Transferrin-Selenium	5	%
Hek293T	DMEM with GlutaMAX	5	µl
	fetal bovine serum	10	%

3.7. Antibodies

Table 13 List of primary antibodies used within this work.

Epitope	Application	Material	Host	Product no.	Provider
Albumin	ELISA	Urine	goat	A90-134A	Bethyl
Cas9	WB	Cells	rabbit	26758-1-AP	Proteintech
Nephrin	IF	Optically cleared tissue	goat	AF4269	R&D Systems
Phalloidin647	IF	Cells	-	647P1-33	Dyomics
RGS1	IF	Cells, FFPE tissue	rabbit	AV42844	Sigma-Aldrich
WT1	IF, RNAscope	FFPE tissue	rabbit	Ab89901	Abcam

Table 14 List of secondary antibodies used within this work.

Epitope	Product no.	Coupled with	Application	Provider
AffiniPure donkey anti-rabbit	711-065-152	Biotin-SP	IHC	Jackson ImmunoResearch
Donkey anti rabbit	711-165-152	Cy3	IF	Jackson ImmunoResearch
Donkey anti rabbit	711-545-152	A488	IF	Jackson ImmunoResearch
Donkey anti sheep	713-005-147	STAR635P	IF	Jackson ImmunoResearch
Goat anti mouse	A90-134P	HRP	ELISA	Bethyl
anti-rabbit IgG (H+L)	111-035-003	HRP	WB, RNAscope	Jackson ImmunoResearch

3.8. Enzymes

Table 15 List of enzymes used within this work.

Enzyme	Product no.	Provider
Collagenase IV	LS004186	Worthington
DNase	9003-98-9	Worthington
ExoSAP-IT™ PCR Product Cleanup Reagent	78201.1.ML	Thermo Fisher Scientific
GoTaq® G2 Hot Start Polymerase	M7401	Promega
Protease	P5147	Sigma

3.9. Consumables

Table 16 List of consumables used within this work.

Consumable	Product no.	Provider
10 cm dish for Agar Plates	82.1473	Sarstedt
384 well plates	785290	Greiner BioOne
96-well plate, sterile, f-bottem, with lid	655180	Greiner BioOne
Adhesive qPCR tape	951.999	Sarstedt
Advanced PAP Pen	Z672548	Merck
AMPure XP Reagent	A63881	Beckman Coulter
Biosphere Filter Tip 10 µl, sterile	70.1116.210	Sarstedt
Biosphere Filter Tip 1000 µl, sterile	70.762.211	Sarstedt
Biosphere Filter Tip 20 µl, sterile	70.1116.215	Sarstedt

Biosphere Filter Tip 200 µl , sterile	70.760.211	Sarstedt
Blotting paper (Type BF4, 580 x 580)	FT-2-521	VWR
Cell culture dishes (10-cm)	430167	Corning
Cell culture primaria dishes (10-cm)		Falcon
Cell culture dishes (6-well)	3516	Corning
Cell lifter	3008	Corning
Combs (12 well, 1 mm) for acrylamide gels	NC3012	Thermo Fisher Scientific
Coverslips (round 18 mm Nr. 1.5)	631-0153	VWR
Eppendorf tubes (1.5 mL)	72.690.001	Sarstedt
Gel cassette (1 mm)	NC2010	Invitrogen
Histosette® I	M499-11	Simport
Luer slip syringe (2 mL)	300185	BD
Luer slip syringe (3 mL)	309658	BD
Microfuge Tube Polypropylene (1.5 mL)	357448	Beckman Coulter
Millipore Immobilon-P Transfer Membranes	T831.1	Carl Roth
Mini Trans-Blot® Filter Paper	1703932EDU	Bio-Rad
Needle 23 G x 1	305762	BD
PCR Soft-tubes 0.2 mL	710970	Biozym
Polypropylene conical tube (15 mL)	227261	Greiner BioOne
Polypropylene conical tube (50 mL)	227261	Greiner BioOne
Protran Nitrocellulose Membranes	16533	Schleicher & Schuell
Safe Lock 1,5 mL Eppendorf tubes	211-2130	VWR
Screw cap tubes	72.692.005	Sarstedt
Strip only MAXISORP, flat bottom well F8	055159	NUNC
Stripettes (10 mL)	4101	LMS
Stripettes (25 mL)	4251	LMS
Stripettes (5 mL)	4051	LMS
Stripettes (50 mL)	4501	LMS
SuperFrost®/Plus microscope slides	7695002	Th.Geyer Group

3.10. Equipment

Table 17 List of equipment used within this work.

Equipment	**Model/Product no.**	**Provider**
96S Super Magnet	A001322	Alpaqua
Autoclave	V-150	Systec
Centrifuge (refrigerated)	5810 R	Eppendorf
DynaMag™-2 Magnet	12321D	Thermo Fisher Scientific
Fusion Solo chemiluminometer	60-FU-SOLO	PeqLab
Heatingblock	TH 21	Ditabis
Homogenizer	Precellys® 24	Bertin instruments

HybEZ™ II Hybridization System	PN 321710/321720	Biotechne
Incubator	BD 115	Binder
IncuCyte®	S3	Sartorius
Laminar Flow Cabinet	HS12	Heraeus
Microcentrifuge	5424	Eppendorf
Microcentrifuge (refrigerated)	5415 R	Eppendorf
Microtome	RM2235	Leica
Nanodrop Spectrophotometer	1000	PeqLab
Pipetman Pipette set (P2, P10, P100)	F167500	Gilson
Pipetman Pipette set (P20, P200, P1000)	F167300	Gilson
Powerpac 200 Power supply	1655052	Bio-Rad
Real-time PCR System	QuantStudio 12K Flex	Thermo Fisher Scientific
Semidry Electroblotting System	Owl™ HEP-1	Thermo Fisher Scientific
Shaker	KS 260	IKA
Slidescanner	S360	Hamamatsu
Suction pump	181-0067DE	VWR
Suction pump (cell culture)	HLC	DITABIS
TapeStation	Agilent 4200	Agilent technologies
TCS SP8 gSTED	-	Leica
Thermal Cycler	C1000 Touch	Bio-Rad
Thermomixer Comfort 1.5 mL Thermoblock	5360 000.011	Eppendorf
UV Transilluminator system	MW312	Intas
Vertical Electrophoresis Cell	Mini-PROTEAN® Tetra	Bio-Rad
Vibratome	VT1200S	Leica
Vortex Mixer	444-1372	VWR
Water bath	WNB 22	Memmert
Water bath (for histology)	HI1210	Leica

3.11. Software and online tools

Table 18 List of software used within this work.

Software	**Version**	**Provider**
AMAP		Bozek Lab, CMMC, University of Cologne
Figma Design		Figma
GraphPad Prism9	9.1.0	GraphPad Software Inc.
ImageJ/Fiji	v1.54b	Wayne Rasband
LAS	4.13	Leica
Mausoleum	7.3.8 b4	Dr. H.-E. Stöffler

Mendeley	1.19.8	Elsevier
Microsoft Office Suite	Professional Plus 2016	Microsoft
Nanodrop 1000	3.8.1	Thermo Scientific
TapeStation		Agilent
QuantStudio	1.4.1	Applied Biosystems
ZEN Blue	3	Zeiss

Table 19 List of online tools used within this work.

Online Tool	**Website**
Benchling	https://www.benchling.com/
Biorender	https://www.biorender.com/
CALINCA	https://calinca.dieterichlab.org/
CRISPR ERA	http://crispr-era.stanford.edu/
CRISPick	https://portals.broadinstitute.org/gppx/crispick/public
Ensembl	https://www.ensembl.org
GTEx Portal	https://www.gtexportal.org/home/
NCBI	https://www.ncbi.nlm.nih.gov/
NCBI PubMed	https://pubmed.ncbi.nlm.nih.gov/
NCBIPrimerBlast	https://www.ncbi.nlm.nih.gov/tools/primer-blast/
The Human Protein Atlas	https://www.proteinatlas.org/

4. Methods

4.1. Animal procedures

4.1.1. Mouse housing

Experimental animals were housed in the specific-pathogen-free animal facility (CECAD Research Center, University of Cologne, Germany), in individually ventilated group cages (Greenline GM500m Tecniplast) at 22 °C and 55% humidity under a 12-hour light rhythm. The animals had unrestricted access to food and water. Breeding and genotyping followed conventional protocols. The mouse line establishment was conducted in the in vivo research facility (CECAD Research Center University of Cologne, Germany). All experiments were carried out using pure C57BL/6N lineage, incorporating both male and female mice. Animals were weighed on a weekly basis and urine was collected upon request. The ages of the animals used for the respective experiments are specified in the figures and/or figure captions. All mouse procedures were authorized by the State Office of North Rhine-Westphalia, Department of Nature, Environment and Consumer Protection (LANUV NRW, Germany; animal approval AZ 81-02.04.2019.A335).

4.1.2. Mouse line generation

Wt1os$^{-/-}$ transgenic mice were generated in the C57BL/6 background using a CRISPR-Cas9 genome-editing system. The gene was modified by introducing a synthetic polyadenylation construct derived from the rabbit β-globin gene, along with enhancer elements (MAZ), into the second exon [121]. For homologous recombination, a phosphorothioate-modified ssODNs (single-stranded oligo DNA nucleotides) repair template (200 nt) containing two homology arms (50 nt each), a polyadenylation site (49 nt), and two MAZ sites (Levitt et al, 1989; Yonaha & Proudfoot, 2000) was synthetized by IDT. Cas9 and crRNAs (IDT) were microinjected into the cytoplasm of fertilized eggs of C57BL/6 mice. CRISPR-Cas9 components used for mouse line generation are listed in Table 6. To obtain homozygous *Wt1os*$^{+/+}$ and *Wt1os*$^{-/-}$ animals, heterozygous *Wt1os*$^{-/+}$ mice were crossed. The animals were backcrossed with wild type C57BL/6 breeder animals from the CECAD *in vivo* facility to maintain the line.

4.1.3. Genotyping

Genomic DNA was isolated from ear biopsies using HotSHOT (hot sodium hydroxide and Tris) extraction method. The ear biopsies were incubated in 75 µl 1x base solution at 95°C for 30 minutes. The samples were cooled down on ice and 75 µl of 1x neutralization solution were added. Genotyping PCR was carried out using the GoTaq® G2 Flexi DNA polymerase kit. Details of PCR and cycling parameters are provided in Table 20 and 21. PCR products were analyzed through 2% agarose gel electrophoresis. For *Wt1os*$^{-/-}$ the PCR products were excised from the gel using a scalpel under UV light. DNA was isolated using the GeneJET Gel Extraction Kit according to manufacturer's protocol and eluted in 12 µl H_2O. To the purified DNA, 3 µl of *Wt1os* F primers (10µM) (Table 4**)** was added. For the Podocin.A286V allele, the PCR product was purified with ExoSAP™ and incubation at 37°C for 15 minutes. 3 µl of DNA was mixed with 7 µl of H_2O and 3 µl of Podocin.A286V.seq primers (10µM) (Table 4)**.** The samples were analyzed by Sanger sequencing at the Microsynth Seqlab GmbH.

Table 20 List of genotyping PCR compositions.

Gene	Component	Volume	
Wt1os	Green GoTaq® Flexi Buffer, 5x	5.0	µl
	$MgCl_2$, 25mM	1.5	µl
	dNTPs, 25mM	0.2	µl
	Wt1os F, 10µM	1.0	µl
	Wt1os R, 10µM	1.0	µl
	GoTaq® G2 Flexi DNA Polymerase	0.2	µl
	H_2O	15.1	µl
	DNA	1	µl

Table 21 List of genotyping PCR cycling conditions.

Gene/allele	Step	Temperature [°C]	Duration [s]	Number of cycles
Wt1os	Initiation	95	180	go to step 2, 35 times
	Denaturation	95	45	
	Annealing	56	60	
	Extension	72	30	
	Final extension	72	180	
	Final hold	15	∞	

4.1.4. Tissue collection

Mice were euthanized by cervical dislocation. The abdominal cavity was opened, and the blood was withdrawn with a heparin coated syringe. The organs were harvested, washed with 1x PBS and fixed in 4% formaldehyde for 24 h at 4°C. Fixed tissue was washed with 1x PBS, dehydrated and embedded in paraffin. For RNA extraction the organs were harvested, washed with 1x PBS and frozen in liquid nitrogen.

4.1.5. Blood analysis

Blood was withdrawn via cardiac puncture of the right ventricle after euthanizing the animals. Blood was centrifuged at 10000 g for 10 minutes at room temperature and the plasma was collected. Plasma urea and creatinine were measured by the central laboratory of the University Hospital of Cologne using a Cobas C 702 (Roche Diagnostics).

4.1.6. Urine analysis

4.1.6.1. Albumin ELISA

A 96 well plate was coated with 100 µl of anti-mouse albumin antibody (1:10,000 dilution in 1x coating buffer) for 1 h at room temperature, then washed 5x with 200 µl of 1x wash solution. All wash steps were performed using the Microplate Wellwash Versa (Thermo Scientific). Each well was blocked with 200 µl of 1x blocking solution overnight at 4°C. The wells were washed again 5x with 200 µl of 1x wash solution. 100 µl of serial dilution of mouse albumin as a standard and samples (samples: 1:2000 dilution in 1x diluent buffer) were added to the wells and incubated for 1 h at room temperature. The plates were washed 5x with 200 µl of 1x wash solution before

incubation with 100 µl of HRP detection antibody (dilution 1:25,000 in 1x diluent buffer) for 1 h at room temperature. The antibodies used for the ELISA are listed in Table X. The plates were washed 5x with 200 µl of 1x wash solution and developed with 100 µl of 1x substrate solution for 15 min at room temperature in the dark. The reaction was stopped by pipetting 100 µl of 1x stop solution. Absorbance was measured at 450 nm using a plate reader (Perkin Elmer). The standards and samples were measured in triplicates.

4.1.6.2. Creatinine measurement

The urinary creatinine was measured using the Creatinine (urinary) Colorimetric Assay Kit (Cayman). Urine samples were diluted 1:20 in water and processed according to the manufacturer's instructions. Absorbance was measured at 450 nm using a plate reader (Perkin Elmer). The standards and samples were measured in triplicates. All steps were carried out at room temperature.

4.1.7. RNA isolation from tissue

Frozen tissue was transferred into a screw cap tube with 1 mm silica beads and 1 ml of TRI Reagent™ Solution. The tissue was homogenized using the Precellys® 24 at 4000 rpm 3x 20 seconds with 5 seconds pauses between the cycles. Tissue lysates were centrifuged at 11000 rfc for 5 minutes at 4°C and the supernatant was transferred to a new 2 ml safe-lock tube. RNA was extracted with the Direct-zol™ RNA Miniprep Plus kit according to the manufactures protocol. The RNA concentrations were measured using the Invitrogen™ Qubit™ RNA Broad Range assay kit. The quality was validated using Nanodrop 1000 spectrophotometer and RIN was determined by RNA separation using High Sensitivity RNA ScreenTape according to manufacturer's instructions.

4.1.8. Transcriptome analysis

Isolated RNA was handed over to the Cologne Center for Genomic RNA Team, who performed the libraries preparation and sequencing. The libraries were prepared with the Illumina® Stranded TruSeq® RNA sample preparation Kit according to manufacturer's instructions. 200 ng of RNA were used as input material. cDNA libraries were validated using HS dsDNA Qubit and by cDNA separation on TapeStation with D1000 DNA ScreenTape (Agilent TapeStation). Equimolar amounts of each library were pooled. The pool was quantified using the Peqlab KAPA Library

Quantification Kit and the Applied Biosystems 7900HT Sequence Detection System. Sequencing was performed on an Illumina NovaSeq6000 instrument with a PE100 protocol.

4.1.9. Reverse transcription

cDNA synthesis was performed using the High-Capacity cDNA Reverse Transcription kit according to manufacturer's protocol. The reaction compositions are listed in the Table 22 and the reaction conditions are listed in the Table 23.

Table 22 cDNA synthesis reaction compositions.

Method	Component	Volume	
Reverse transcription	10X RT Buffer	2.0	µl
	25X dNTP Mix (100 mM)	0.8	µl
	10X RT Random Primers	2.0	µl
	MultiScribe™ Reverse Transcriptase	1.0	µl
	H_2O	4.2	µl

Table 23 cDNA synthesis conditions.

Settings	Step 1	Step 2	Step 3	Step 4
Temperature [°C]	25	37	85	4
Time [min]	10	120	5	Hold

4.1.10. qPCR with SybrGreen

qPCR reactions were performed with Power SYBR™ Green PCR Master Mix. qPCR primers (IDT) used for thw qPCR are listed in Table 4. qPCR compositions and cycling conditions are listed in the Table 24. qPCR was run using the samples in technical triplicates and genomic DNA, -RT (sample lacking the reverse transcriptase), and H_2O as controls. The reaction was performed using the QuantStudio 12K Flex Real-time PCR System and data was analyzed with Quantstudio and Prism software.

4.1.11. qPCR with TaqMan probes

qPCR reactions were performed with TaqMan™ Universal PCR Master Mix. PrimeTime™ qPCR Probes (IDT) are listed in Table 5. qPCR compositions and cycling conditions are listed in the Table 25. qPCR was run using the samples in technical triplicates and genomic DNA, -RT (sample lacking the reverse transcriptase), and H_2O

as controls. The reaction was performed using the QuantStudio 12K Flex Real-time PCR System and data was analyzed with Quantstudio and Prism software.

Table 24 qPCR reaction compositions.

Method	Component	Volume	
SybrGreen	SYBR™ Power SYBR™ Master Mix	5.0	µl
	Primer forward	0.035	µl
	Primer reverse	0.035	µl
	H_2O	3.93	µl
	cDNA	2	µl
TaqMan	TaqMan™ Gene Expression Master Mix	5.0	µl
	TaqMan probe	0.5	µl
	H_2O	3.5	µl
	cDNA	2	µl

Table 25 List of qPCR cycling conditions.

Method	Stage	Step	Temperature [°C]	Duration [s]	Number of cycles
SybrGreen	Hold	1	50	120	go to step 1, 39 times
		2	95	600	
	PCR	1	95	15	
		2	60	60	
	Melt Curve	1	95	15	
		2	60	60	
TaqMan	Hold	1	50	120	go to step 1, 39 times
		2	95	600	
	PCR	1	95	15	
		2	60	60	

4.1.12. RNA in situ hybridization on FFPE tissue

The paraffin-embedded tissue (Section: Tissue collection) was sectioned into 5 µm thick slices on a Microtome, mounted on glass slides and dried overnight. RNAScope Integrated Co-Detection Workflow (IWC) was applied according to manufacturer's protocol. The tissue was deparaffinized in xylol (2x 5 min) and 100% ethanol (2x 2 min) and dried for 5 min in room temperature. Blocking was performed by incubation with RNAscope® Hydrogen Peroxide solution for 10 min in room temperature. After

washing with H_2O, the epitope was retrieved by boiling slides in RNAscope® 1X Co-Detection Target Retrieval for 15 min. The tissue was washed first with H_2O and then with 1x PBS-T. Then, the primary antibody incubation was performed (1:500 dilution in Co-Detection Antibody Diluent) overnight at 4°C. The slides were washed with 1x PBS-T and fixed with 10% Neutral Buffered Formalin (NBF) for 30 min at room temperature. After 3 washes with 1x PBS-T, the protease treatment was done with RNAscope™ Protease Plus Reagent for 30 min at 40°C in the HybEZ™ Oven. The slides were washed in 1X Wash Buffer and the specific RNAscope probe was applied and hybridized for 2h at 40°C in the HybEZ™ Oven. All RNAscope probes are listed in Table 9. The sections were washed in 1X Wash Buffer, and the signal amplification was performed by sequential incubation of the tissue with RNAscope® 2.5 HD Detection Kit (Red) reagents: AMP1 (30 min at 40°C in the HybEZ™ Oven), AMP2 (15 min at 40°C in the HybEZ™ Oven), AMP3 (30 min at 40°C in the HybEZ™ Oven), AMP4 (15 min at 40°C in the HybEZ™ Oven), AMP5 (30 min at 40°C in the HybEZ™ Oven), AMP6 (15 min at 40°C in the HybEZ™ Oven). The slides were washed after each amplification step in 1X Wash Buffer. Signal detection was accomplished by incubation of the sections in RED working solution, prepared by mixing Fast RED-B to Fast RED-A reagents in the 1:60 ratio, for 10 min at room temperature. After washing with H_2O, the Co-Detection Blocker was applied, and the tissue was incubated for 15 min at 40°C in the HybEZ™ Oven. Slides were washed with 1x PBS-T and secondary antibody incubation was performed (1:500 dilution in Co-Detection Antibody Diluent) for 1 min at room temperature. Primary and secondary antibodies used for RNAscope are listed in Table 13. After washing the slides with 1x PBS-T, the IHC signal was detected. Equal volumes of BROWN-A and BROWN-B reagents were mixed, and the tissue was incubated for 10 min at room temperature. Slides were washed with H_2O and counterstained with hematoxylin for 3 seconds. After rinsing the slides with H_2O, the slides were washed with 0.02% Ammonia water for 10 sec, then again with pure H_2O. The slides were embedded in EcoMount mounting medium, mounted with a cover slip and dried overnight. The tissue was imaged using the Hamamatsu Slidescanner S360 with the 40x objective.

4.1.13. Optical Clearing of Kidney Tissue

Formaldehyde fixed tissue (**Section**: Tissue collection) was washed in 1x PBS and a 1-2 mm thick chunk was immersed in hydrogel solution overnight at 4°C. Then, the gel

was polymerized by incubating for 3 h at 37°C. After that, the tissue was washed 3x with 1x PBS to remove the remaining gel and embedded in 3% agarose. The kidney was sectioned into 200 µm thick slices on a Vibratome and transferred to the clearing solution, where it was incubated overnight at 50°C gently shaking at 300 rpm. The samples were washed once with 1x PBT-X for 5 min and the primary antibody was applied (dilution 1:100 in 1x PBT-X). Primary antibody incubation was carried out overnight at 37°C shaking at 300 rpm. After washing the samples once with 1x PBT-X for 5 min, the secondary antibody was added (dilution 1:100 in 1x PBT-X) and the tissue was incubated overnight at 37°C shaking at 300 rpm. The sections were washed once with 1x PBT-X for 5 min and embedded in a saturated (80.2% w/w) fructose solution. The tissue was imaged using the TCS SP8 Gsted 3X Superresolution and Confocal Microscope (Leica) with the 100x objective. Image analysis was performed with ImageJ/Fiji and AMAP software.

4.1.14. FFPE tissue sectioning, deparaffinization and rehydration

The paraffin-embedded tissue (**Section**: Tissue collection) was sectioned into 2 µm thick slices on a Microtome, mounted on glass slides and dried overnight. Tissue was deparaffinized in xylene (2x 2 min) and hydrated by incubation in a descending ethanol row (2x2 min 100% ethanol, 2x2 min 95% ethanol, 2x2min 70% ethanol, and 2min H_2O).

4.1.15. Periodic acid–Schiff (PAS) staining on tissue

The paraffin-embedded tissue (**Section**: Tissue collection) was pretreated as described above (**Section**: FFPE tissue sectioning, deparaffinization and rehydration). Sections were oxidized using 0.9% periodic acid, washed with H_2O and incubated with Schiff's reagent for 10 minutes. The slides were rinsed in running tap H_2O for 2 minutes and then incubated with Meyer's hematoxylin for 10 seconds. The tissue was washed with H_2O for 3 minutes and dehydrated by incubation in an ascending ethanol row (2x2 min 70% ethanol, 2x2 min 95% ethanol, 2x2min 100% ethanol, and 2x2min xylene). The sections were embedded with Histomount, mounted with a cover slip and dried overnight. All steps were carried out at room temperature. The tissue was imaged using the Hamamatsu Slidescanner S360 with the 40x objective. Tissue histology was evaluated by an experienced clinical nephropathologist at the University Hospital of Cologne.

4.1.16. Immunohistochemistry staining on tissue

Sectioning, deparaffinization and rehydration were performed as described above (**Section**: Periodic acid–Schiff (PAS) staining). Antigen retrieval was performed by boiling in 10 mM citric acid buffer pH 6 (RGS1) or 10 mM Tris-EDTA buffer pH 9 (WT1, Abcam) for 10 minutes. The tissue was cooled down to room temperature and washed 1x 5min in 1x TBS. Then the sections were incubated in 3% H_2O_2 for 15 minutes to block endogenous peroxidases. Avidin/Biotin blocking step was performed by incubation the slides in the avidin solution for 15 minutes, washing with 1x TBS for 5 minutes and incubation with the biotin solution for 15 minutes. All steps were carried out at room temperature. The tissue was washed in 1xTBS for 5 minutes and then incubated with the primary antibodies (1:500 dilutions in 1% BSA/TBS) overnight at 4°C. The samples were washed 3x 5 minutes in 1x TBS and incubated with secondary antibodies (1:500 dilutions in 1% BSA/TBS) for 1 h at room temperature. Primary and secondary antibodies used for immunohistochemistry staining are listed in Tables 13 and 14. The sections were washed 3x 5 minutes with 1x TBS and then incubated with the ABC kit for 30 minutes at room temperature. The chromogenic signal development was performed by applying the DAB chromogen mixture in substrate buffer (Dako) for 1 minute. Slides were washed H_2O for 5 minutes and then incubated with Meyer's hematoxylin for 10 seconds. The tissue was washed with H_2O for 3 minutes and dehydrated by incubation in an ascending ethanol row (2x2 min 70% ethanol, 2x2 min 95% ethanol, 2x2min 100% ethanol, and 2x2min xylene). The sections were embedded with Histomount, mounted with a cover slip and dried overnight. The tissue was imaged using the Hamamatsu Slidescanner S360 with the 40x objective.

4.1.17. Immunofluorescence staining on tissue

The paraffin-embedded tissue (**Section**: Tissue collection) was pretreated as described above (**Section**: FFPE tissue sectioning, deparaffinization and rehydration). The sections were washed in 1x PBS and then blocked in 5% NDS/PBS for 1 hour at room temperature. The tissue was washed with 1x PBS 3x 5 minutes and incubated with the primary antibodies (1:500 dilution in 5% BSA/PBS) overnight at 4°C. The samples were washed with PBS 3x 5 minutes and incubated with fluorescently labeled secondary antibodies together with Hoechst (antibodies: 1:500 dilutions, Hoechst: 1:1000 dilution in 5% BSA/PBS) for 1 h in room temperature. The samples were

washed with PBS 3x 5 minutes followed by embedding with ProLong Diamond antifade reagent and mounting with a cover slip. The tissue was imaged using the TCS SP8 confocal microscope (Leica) with the 40x objective. Image analysis was performed with ImageJ/Fiji.

4.1.18. Polyacrylamide gel preparation

12% resolving gel was prepared by mixing 20 ml of separating gel buffer, 200 µl of 10% ammonium persulfate (APS) and 30 µl of tetramethylethylenediamine (TEMED) (see Table 1). The solution was then poured into a gel cassette and covered with 1ml of isopropanol. After allowing the gel to polymerize for 30 minutes, the isopropanol was removed. The stacking gel was prepared by combining 5 ml of stacking gel buffer (see Table 3) with 50 µl of 10% APS and 7.5 µl of TEMED. A 12-well comb was placed into the gel, and the stacking gel was allowed to polymerize for 30 minutes. All steps were carried out at room temperature.

4.2. Cell culture

4.2.1. Culturing of immortalized cell lines

Heat-sensitive mouse podocytes (HSMPs), HSMPs.dCas9.VP64, and AB8 (human podocytes) were grown at 33°C and 5% CO_2 in standard CO_2 incubators. HSMPs were cultured in Collagen I-coated primaria dishes (Corning). To differentiate HSMPs and AB8 cells, at 60% confluence the dishes were incubated in the 37°C standard incubators. Cells were incubated for 10 days with medium being changed every second day. Human embryonic kidney cells HEK293T were grown at 37°C and 5% CO2 in standard CO2 incubators. All cell lines were handled under sterile conditions in the laminar-flow cell culture hoods. The composition of cell culture media is listed in Table 12.

4.2.2. GapmeR-mediated knockdown

AB8 cells were seeded a day before treatment to a confluency of 60% in a 6-well plate. Cells were transfected with a mix of custom WT1AS GapmeRs reaching 150 pmol concentration using Lipofectamine™ RNAiMAX transfection reagent according to manufacturer's instructions. GapmeRs used in the knockdown experiments are listed in Table 8.

Table 26 Composition of GapmeR transfection reactions.

Components	Solution A	Solution B
LipoRNAiMAX	6 µl	-
GapmeRs	-	4 µl
Opti-MEM®	200 µl	200 µl

Solutions A and B (see Table 26) were prepared and incubated at room temperature for 5 minutes. Then, they were combined and incubated for another 20 minutes at room temperature. The mixture was added dropwise to the wells and after 24h the cells were harvested.

4.2.3. siRNA-mediated knockdown

The HSMPs cells were seeded a day before the procedure to a confluency of 60% in a 6-well plate. The medium was replaced with the fresh HSMPs growth medium. The cells were transfected with 40 nM siRNA (ON-TARGETplus SMARTpool) or (ON-TARGETplus Non-targeting Control pool) using Lipofectamine™ RNAiMAX transfection reagent according to manufacturer's instructions. siRNAs used in the experiments are listed in Table 8.

Table 27 Composition of siRNA transfection reactions.

Components	Solution A	Solution B
LipoRNAiMAX	6 µl	-
siRNA	-	4.8 µl
Opti-MEM®	200 µl	200 µl

Solutions A and B (see Table 27) were prepared and incubated at room temperature for 5 minutes. Then, they were combined and incubated for another 20 minutes at room temperature. The mixture was added dropwise to the wells and after 24 the cells were harvested.

4.2.4. HSMPs.dCas9.VP64 and AB8.dCas9.VP64 stable cell line generation

4.2.4.1. Lentivirus production

To produce the lentivirus, the 3rd generation pLenti6.3 vector carrying dCas9 fused with the VP64 activation domain, and a blasticidin resistance cassette was co-transfected along with the helper packaging and envelope plasmids into the packaging cell line HEK293T. 500 µl of $CaCl_2$ was combined with the helper plasmids and the dCas9 pLenti6.3 construct. While vortexing, 500 µl of 2x HEBS solution was added dropwise to the mixture. A plasmid carrying GFP was used as a positive transfection control to assess the transfection efficiency. The plasmids used for lentivirus production are listed in Table 10. Five hours after the transfection, the HEK293T medium was replaced with HSMPs or AB8 medium containing 20 mM HEPES. The composition of cell culture media is listed in table 12. The cells were cultured under standard conditions (**Section**: Culturing of immortalized cell lines) for three days before the lentivirus was harvested. To collect the virus, the medium was collected and centrifuged at 200 rfc for 5 min at room temperature. The clear supernatant was then collected using a 20 ml LuerLock syringe and filtered through a 0.45 µm polyvinylidene fluoride (PVDF) filter. The lentivirus was stored at 4°C. All steps were carried out under biosafety level S2 conditions. Components of virus production reactions are listed in Table 28.

Table 28 Composition of reaction for virus production.

Components	Amount
pRSV rev	2.5 µg
pMD2 vsv g	3.5 µg
pMDL g/p	6.5 µg
plenti dCAS-VP64_Blast	10 µg
$CaCl_2$	500 µl
2x HEBS	500 µl

4.2.4.2. Lentiviral transduction

To transduce the HSMPs or AB8 cells, the cells were split the day prior to transduction to reach 50% confluency on the day of the procedure. First, the cell medium was replaced with 5 ml of lentivirus mixed with 5 µl of Polybrene (Hexadimethrin bromide, 8 mg/ml). The cells were incubated with the lentivirus for 24 hours under normal culture conditions. Then the virus-containing medium was replaced with 10 ml of fresh HSMPs medium. 48 h later, the cells were split at a 1:4 ratio. After an additional 24 hours, cell selection with blasticidin (10 mg/ml) was started. The cells were treated with blasticidin for three days. In parallel, a selection control dish containing wild-type, non-transduced HSMPs or AB8 cells was treated with blasticidin.

4.2.3. CRISPRa-mediated gene expression activation

The HSMPs.dCas9.VP64 and and AB8.dCas9.VP64 cells were seeded a day before the procedure to a confluency of 60% in a 6-well plate. The medium was replaced with the fresh growth medium. The cells were transfected with a mix of custom sgRNA targeting the *Wt1os* promoter using Lipofectamine™ RNAiMAX transfection reagent according to manufacturer's instructions. sgRNAs used in the CRISPRa experiments are listed in Table 7.

Table 29 Composition of CRISPRa transfection reactions.

Components	Solution A	Solution B
LipoRNAiMAX	6 µl	-
sgRNA mix (1:1)	-	4 µl
Opti-MEM®	200 µl	200 µl

Solutions A and B (see Table 29) were prepared and incubated at room temperature for 5 minutes. Then, they were combined and incubated for another 20 minutes at room temperature. The mixture was added dropwise to the wells and after 48 the cells were harvested.

4.2.4. Cell lysis for western blot

The growth medium was aspired, and the cells were washed with PBS. After removing the washing PBS, 1 ml of cold PBS was added, and cells were collected using a scraper. The cell suspension was transferred into a 2 ml tube on ice and pelleted for 5

minutes at 200 rfc in 4°C. The supernatant was removed, and the pellet was resuspended in 80 µl modified RIPA buffer. The cells were incubated on ice for 15 minutes and centrifuged for 20 minutes at 11000 rfc in 4°C. The cell lysates were transferred into new 1,5 ml tubes and mixed with 16 µl 5x Laemmli sample buffer. The samples were incubated for 5 min in 95°C at a heating block and centrifuged for 2 min at 20000 rfc. Cell lysates were stored at -20°C.

4.2.5. RNA isolation from the cells

HSMPs, HSMPs.dCas9.VP64 and AB8 cells grown in a 6-well plate were resuspended in 1 ml TRI Reagent™ Solution and incubated for 3 minutes at RT. Cell lysate was centrifuged at 11000 rfc for 5 minutes at 4°C and the supernatant was moved to a new 2 ml safe-lock tube. RNA extraction and quality measurement was performed like for the tissue lysate (**Section**: RNA isolation from the tissue).

4.2.6. RNA in situ hybridization on cells

HSMPs, HSMPs.dCas9.VP64 and AB8 cells grown in a 12-well plate on glass coverslips until reaching a confluence of 60-80%. The growth medium was removed, the cells were rinsed with 1x PBS and then fixed in 4% formaldehyde for 30 minutes at room temperature. RNAscope® Multiplex Fluorescent assay was applied following manufacturer's instructions. After washing 3x 5 minutes with 1x PBS the cells were dehydrated by incubation in the ascending ethanol row as follows: 50% ethanol for 5 min, 70% ethanol for 5 min, 100% ethanol for 5 min, 100% ethanol for 10 min. Then, the cells were rehydrated by incubation in the descending ethanol row as follows: 70% ethanol for 2 min, 50% ethanol for 2 min, 1x PBS for 10 min. The cells were blocked by applying RNAscope™ Hydrogen Peroxide Reagent and incubating for 10 min at room temperature, followed by washing in H_2O. Then, the protease treatment was accomplished by incubating cells with RNAscope™ Protease III Reagent (1:15 dilution in 1x PBS) for 10 min at room temperature. After the cells were washed in 1x PBS, the specific RNAscope probe or control probe was applied. Probes used for the RNAscope are listed in Table 9. The coverslips were incubated for 2 h 40°C in the HybEZ™ Oven. After washing in 1x RNAscope® Wash Buffer, signal amplification was performed by sequential incubation of the coverslips with RNAscope™ Fluorescent Multiplex Assay reagents: AMP1 (30 min at 40°C in the HybEZ™ Oven), AMP2 (30 min at 40°C in the HybEZ™ Oven), AMP3 (15 min at 40°C in the HybEZ™ Oven). The cells were washed

with 1x RNAscope® Wash Buffer after each step. HRP-C1 signal was developed by applying MultiplexFL v2 HRP-C1 and incubating for 15 min at 40°C in the HybEZ™ Oven. Coverslips were washed in the 1x RNAscope® Wash Buffer and then incubated with the Opal520 fluorophore (Akoya Biosciences) (1:1000 dilution in RNAscope® Multiplex TSA Buffer) for 30 min at 40°C in the HybEZ™ Oven. The cells were washed with 1x RNAscope® Wash Buffer and then blocked with the RNAscope Multiplex FL v2 HRP blocker for 15 min at 40°C in the HybEZ™ Oven. After washing with 1x RNAscope® Wash Buffer, the coverslips were incubated with RNAscope Multiplex FL v2 DAPI for 30 sec at room temperature. The reagent was removed by tapping and the cells were mounted with Prolong Diamond antifade reagent and dried overnight. Imaging was performed using the TCS SP8 Confocal microscope. Image analysis was performed using ImageJ/Fiji.

4.2.7. Immunofluorescence staining of cultured cells

HSMPs and HSMPs.dCas9.VP64 cells grown in a 12-well plate on glass coverslips until reaching a confluence of 60-80%. The growth medium was removed, the cells were rinsed with 1x PBS and then fixed in 4% formaldehyde for 15 minutes at room temperature. After washing 3x 5 minutes with 1x PBS the cells were blocked in 5% normal donkey serum (NDS) in PBT-X for 1h at room temperature. The cells were washed 3x 5 min with 1x PBS and incubated with the primary antibody (1:500 dilution in 5% NDS/PBT-X) overnight at 4°C. The coverslips were washed once in 1x PBS and then incubated with a fluorescently labeled secondary antibody together with Hoechst (secondary antibody 1:500, Hoechst 1:1000 dilution in 5% NDS/PBT-X) for 45 minutes at room temperature. The cells were washed with 1x PBS, mounted in Prolong Diamond antifade reagent and dried overnight. Imaging was performed using the TCS SP8 Confocal microscope. Image analysis was performed using ImageJ/Fiji. The antibodies used for the staining are listed in Tables 13 and 14.

4.2.8. Wound-healing (scratch) assay

HSMPs.dCas9.VP64 cells grown in a 12-well plate until reaching full confluence. A scratch was introduced in the cells monolayer across the well with a 200 µl pipette tip. The medium was removed, the cells were rinsed with 1x PBS and then fresh medium was added carefully. A picture of the well was taken and the acquired region was

marked on the well bottom. Cells were incubated in the growing conditions for 24 h. After this time the second picture of the marked region was taken.

4.2.9. Calcium imaging

HSMPs.dCas9.VP64 cells grown in a 12-well plate on glass coverslips until reaching a confluence of 60-80%. The growth medium was removed, the cells were rinsed with 1x PBS and then 1 ml of Ringer's buffer, 2 µl of Fluo-4 AM and 2 µl of 10% Pluronic solution were added. Cell were incubated with the probe for 30 min at 33°C and 5% CO_2 in standard CO_2 incubator. After that, the coverslips were washed with Ringer's buffer to remove the dye. The coverslips were inserted in the imaging chamber and 200 µl of Ringer's buffer was added. The cells were imaged using the Axio Observer microscope (Zeiss) with the 10x objective in a time series. First, five frames were taken to define the background fluorescence value, after that 200 µl of 200 µM ATP was added. Pictures were acquired for 120 seconds in 3 seconds intervals. Image analysis was performed with ImageJ/Fiji software.

4.2.10. SDS-PAGE and Western blot

Sodium dodecyl sulfate polyacrylamide gel electrophoresis (SDS-PAGE) was performed in the XCell SureLock Mini-Cell Electrophoresis System, filled with 1x SDS-PAGE running buffer. Samples of cell lysates (Section: cell lysate), were loaded onto the polyacrylamide gel. 5 µl of PageRuler Plus Protein Ladder was used as a molecular mass marker. Separation was conducted at 180 V for 1.5 h. Proteins were subsequently transferred onto a Millipore Immobilon-P polyvinylidene difluoride (PVDF) membrane through the Owl™ HEP-1 semi-dry electroblotting system. Prior to transfer, the PVDF membrane was activated in methanol for 30 seconds, and then washed in 1x transfer buffer. The gel was incubated with filter paper in 1x transfer buffer. The blot assembly was arranged as follows: filter paper, membrane, polyacrylamide gel, filter paper. Protein transfer was performed at 12 V for 1 h. Then the membrane was blocked in a solution of 5% BSA/1x protein wash buffer for 1 h. The membrane was washed 3x 10 minutes with 1x protein wash buffer, then incubated with the primary antibody (1:10000 dilution in 1x protein wash buffer). The membrane was washed 3x 10 minutes with 1x protein wash buffer and then incubated with a horseradish peroxidase (HRP)-conjugated secondary antibody (1:30000 dilution in 1x protein wash buffer). The membrane was washed 3x 10 minutes with 1x protein wash

buffer. Detection of proteins was carried out using chemiluminescence by treating the membrane with ECL detection solution. All steps were carried out at room temperature. The signal was then visualized with the PeqLab Fusion Solo chemiluminometer.

4.3. Data analysis

4.3.1. Automatic Morphological Analysis of Podocytes (AMAP)

The images of tissue (**Section**: Optical Clearing of Kidney Tissue) were analyzed using an automated method described before by our group [67]. Briefly, for SD length per area, the SD pattern was automatically detected and measured within the defined region of interest (ROI). The FP circularity score was calculated using the formula: Circularity = 4 × π × (area / perimeter²), where a value of 1 indicates a perfect circle and values approaching 0 represent more elongated or irregular shapes.

4.3.2. RNA in situ hybridization staining data analysis

The images of the cells (**Section:** RNA in situ hybridization on cells) were analyzed using the ImageJ software. First, the nuclei mask was generated and the total number of dots (RNA signal) was determined. Then, the fraction of signal colocalizing with the nuclei staining was determined (nuclear localization).

4.3.3. Wound-healing (scratch) assay

The images of the cells (**Section:** Wound-healing (scratch) assay) were analyzed using the ImageJ software. First, the region of the introduced scratch was segmented using the polygonal selection tool. Then, the area of the selected region was measured. The measurement for performed for two timepoints: right after introducing the scratch (T_1) and 24 h after (T_2). The scratch closure was calculated using the following formula:

$$\text{Scratch closure} = \frac{T_1 - T_2}{T_1} \text{ x } 100\%$$

4.3.4. Calcium imaging

The images of the cells (**Section:** Calcium imaging) were analyzed using the ImageJ software. First, using the maximum intensity projection, the cell mask was generated. Then, the average fluorescence intensity for each frame was calculated. Average fluorescence intensity of the first five frames acquired before stimulating cells was used

as a background. The signal-to-noise ratio was determined using the background value and the maximum fluoresce value after ATP stimulation.

4.3.5. glomRNAseq data analysis

RNA sequencing data were processed using the nf-core/rnaseq pipeline version 3.13.2 [122] and nextflow version 23.04.1.5866, executed within a singularity container. Default parameters were applied unless otherwise specified. The mouse reference genome (Mus_musculus.GRCm38.dna_sm.primary_assembly.fa) and the corresponding gene annotation (Mus_musculus.GRCm38.102.gtf.gz) were used for alignment and quantification. Trim Galore[123] was used for adapter and quality trimming. Salmon[124] was used for transcript-level quantification, with parameters (--numBootstraps 100, --validateMappings, --gcBias, and --seqBias) applied to improve the accuracy of quantification and reduce potential biases. The resulting transcript abundance estimates were used for downstream analyses. Transcript quantifications were imported using the tximport package[125]. Gene-level quantification was scaled using “length-scaled TPM”, while transcript-level quantifications were scaled using the "dtuScaledTPM". Genes with fewer than three samples exhibiting non-zero expression were excluded from further analysis. The included genes were then normalised and analysed for differential gene expression using DESeq2[126]. Gene Set Enrichment Analysis (GSEA) on KEGG pathways was performed using the clusterProfiler package[127] to identify enriched biological pathways.

5. Results

FSGS remains a major challenge in nephrology, leading to proteinuria and progressive kidney dysfunction with no targeted treatment options available. Despite extensive research on the molecular mechanisms underlying FSGS, most studies have focused on protein-coding genes, leaving the role of non-coding RNAs largely unexplored. LncRNAs represent a diverse and functionally significant class of transcripts that regulate various cellular processes, yet their involvement in FSGS and podocyte biology remains poorly characterized. The limited availability of specialized analytical tools for lncRNA research in kidney disease has further hindered progress in this area.

To address this gap, we present CALINCA, a bioinformatic pipeline designed to systematically analyze lncRNA expression in murine FSGS models. CALINCA (available to the community under the following link: https://calinca.dieterichlab.org/), quantifies both annotated and de novo assembled lncRNAs while providing essential insights into their podocyte specificity, evolutionary conservation, and relevance in human datasets. By integrating multiple layers of information, the pipeline facilitates the identification of lncRNAs with potential roles in podocyte injury and FSGS pathogenesis. The development of CALINCA represents a crucial step toward expanding lncRNA research in kidney disease and may contribute to the discovery of novel molecular mechanisms and therapeutic targets.

In this paper, we describe the methodology behind CALINCA, demonstrate its application to FSGS datasets, and discuss its broader implications for renal research. Furthermore, the insights gained from CALINCA serve as the foundation for the experimental studies presented in the following chapters, where we functionally characterize candidate lncRNAs identified through this approach.

5.1. Publication: CALINCA – a novel pipeline for the identification of lncRNAs in podocyte disease

Sweta Talyan [1,3#], **Samantha Filipów** [2,4#], Michael Ignarski[2,4], Magdalena Smieszek[3], He Chen[2,4], Lucas Kühne[2], Linus Butt[2,4], Heike Göbel[5], K. Johanna R. Hoyer-Allo[2,4], Felix C. Köhler[2,4], Janine Altmüller[6], Paul Brinkkötter[2,4], Bernhard Schermer[2,4], Thomas Benzing[2,4], Martin Kann[2,4], Roman-Ulrich Müller [2,4*+] and Christoph Dieterich [1,3*]

[#, +] equal contribution

[1] German Center for Cardiovascular Research (DZHK), Partner site Heidelberg/Mannheim, Im Neuenheimer Feld 669, 69120, Heidelberg, Germany.
[2] Department II of Internal Medicine and Center for Molecular Medicine, University of Cologne, Faculty of Medicine and University Hospital Cologne, Cologne, Germany.
[3] Section of Bioinformatics and Systems Cardiology, Klaus Tschira Institute for Integrative Computational Cardiology and Department of Internal Medicine III, Im Neuenheimer Feld 669, 69120, Heidelberg, Germany.
[4] Cologne Excellence Cluster on Cellular Stress Responses in Aging-associated Diseases (CECAD), University of Cologne, 50931, Cologne, Germany.
[5] Institute for Pathology, Diagnostic and Experimental Nephropathology Unit, University of Cologne, Faculty of Medicine and University Hospital Cologne, Cologne, Germany.
[6] Cologne Center for Genomics, University of Cologne, 50931, Cologne, Germany.

* Correspondence: christoph.dieterich@uni-heidelberg.de (C.D.), roman-ulrich.mueller@uk-koeln.de (R.-U.M.)

DOI: 10.3390/cells10030692

5.2. Localization of *Wt1os* in the kidney

Our previous RNA sequencing data indicated that *Wt1os* is a podocyte specific lncRNA[120]. This finding was supported experimentally by both qPCR and the RNA *In situ hybridization* staining which demonstrated its localization in the glomerulus. To further pinpoint the localization of *Wt1os* within podocytes, we employed the Integrated Co-detection Workflow (ICW) RNAscope, an RNA In situ hybridization technique that allows RNA visualization together with protein detection via an immunohistochemistry-based approach. We combined *Wt1os* lncRNA staining with immunolabelling of the podocyte marker protein WT1 on wild type mouse kidney tissue. The overlap of the RNA signal and protein staining demonstrated podocyte-specific localization of *Wt1os* (

Figure 6). *Wt1os* was absent from Wt1-negative glomerular cells and from kidney tubules.

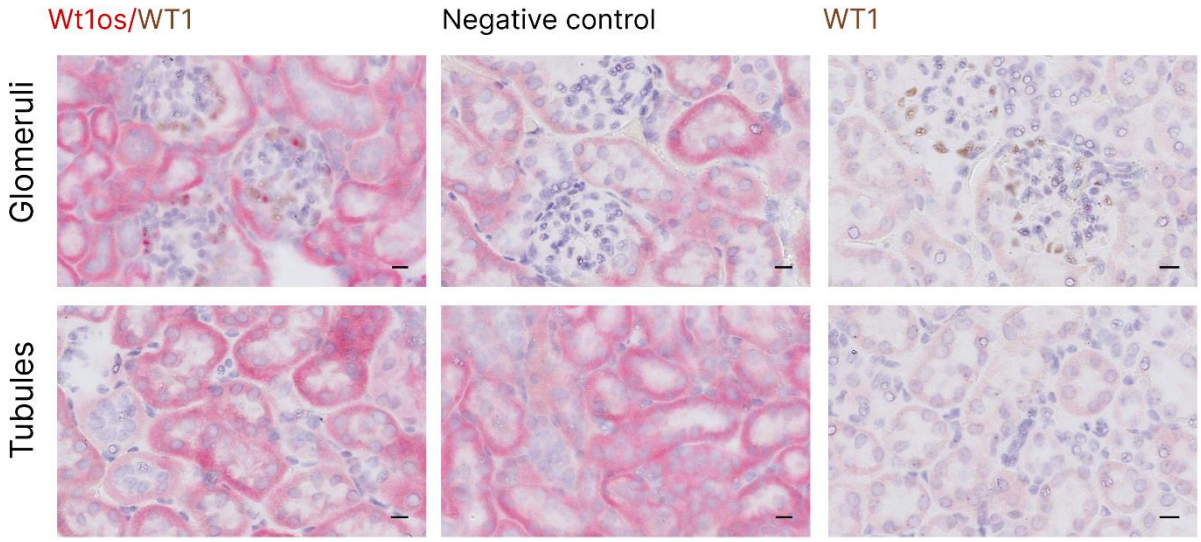

Figure 6. *Wt1os* is a podocyte specific lncRNA.

RNA In situ hybridization coupled with immunohistochemistry staining shown that *Wt1os* is expressed in podocytes but is absent from other glomerular and tubular cell types. Co-staining of *Wt1os* RNA with the podocyte marker protein WT1 on wild type mouse FFPE (formalin-fixed paraffin-embedded) kidney. The colocalization of red (*Wt1os*, RNA) and brown (WT1, protein) signals indicates podocyte specificity of *Wt1os* RNA (left panels). Immunohistochemistry staining of the podocyte marker protein WT1 on the wild type mouse FFPE kidney (middle panels). Negative control treated with an unspecific probe and without primary antibody (right panels). Red tubular background visible due to the endogenous alkaline phosphatase reaction with the red chromogenic substrate. The sections were counterstained with hematoxylin to visualize the nuclei. Brightfield image was acquired with a Hamamatsu S360 slidescanner with a 20x objective. Scale bar: 10 µm.

5.3. Generation and validation of a *Wt1os* loss-of-function mouse line

To elucidate the role of *Wt1os*, we decided to study its function *in vivo*. To ensure an efficient loss of function for *Wt1os* without affecting the adjacent Wt1 gene or their shared promoter, we chose to generate a *Wt1os*$^{-/-}$ mouse line using a CRISPR-Cas9-based approach. This involved introducing into the second exon of the *Wt1os* gene a strong poly(A) polyadenylation signal (SPA) from the rabbit β-globin gene, followed by two MAZ (Myc-associated zinc finger protein) elements. MAZ sites are known to strongly activate cleavage and polyadenylation at an upstream SPA (**Figure 7 a**) [128].

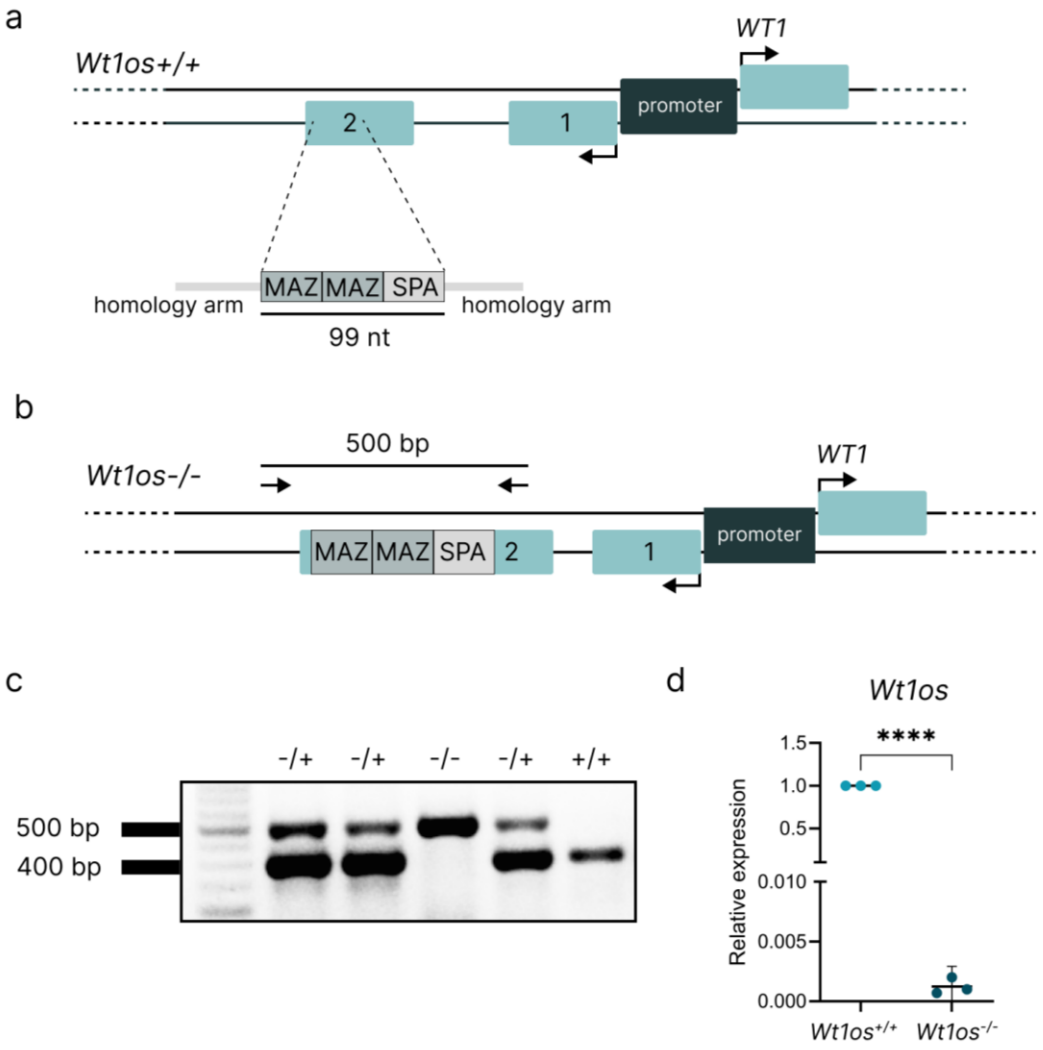

Figure 7. Generation and validation of the *Wt1os*$^{-/-}$ mouse line.

a. Strategy for *Wt1os*$^{-/-}$ mouse line generation. A synthetic polyadenylation site (SPA) followed by two MAZ sites was inserted into the second exon of the *Wt1os* gene using a CRISPR-Cas9-based approach.

continued on next page

A 200 nt ssODN, containing two homology arms (left 36 nt, right 65 nt), a polyadenylation site (49 nt), and two MAZ sites (25 nt each), was used as template for homologous recombination. **b. Genotyping PCR strategy.** Genotyping was performed using primers flanking the insertion site. The expected amplicon size was ~400 bp for the wild type allele and ~500 bp for the allele containing the inserted SPA. Light blue boxes represent exons, thin dark lines connecting exons indicate introns, black arrows at the first exon show the transcription direction, black arrows above the gene mark primer positions, and the black line above represents the resulting PCR product**. c. Validation of the integration of the polyadenylation signal.** The correct genomic modification was confirmed by PCR. The image of a 2% agarose gel shows the amplicons specific for the SPA-containing allele (~500 bp) and the wild-type allele (~400 bp) obtained from genomic DNA of homozygous *Wt1os*$^{-/-}$, heterozygous *Wt1os*$^{-/+}$, and wild-type *Wt1os*$^{+/+}$ animals. **d. Integration of SPA leads to reduction of *Wt1os* expression.** *Wt1os* expression was significantly reduced in *Wt1os*$^{-/-}$ animals. The graph depicts qPCR data showing *Wt1os* expression level in the whole kidney of *Wt1os*$^{-/-}$ animals in comparison to the *Wt1os*$^{+/+}$ controls. Data presented as mean with 95% CI. A two-tailed T-test was performed to determine statistical significance. p-value: **** ≤0.0001).

This strategy was expected to lead to premature transcription termination and transcript polyadenylation, leading to a complete loss of *Wt1os* lncRNA [129]. Given that *Wt1os* is a lncRNA specifically expressed in podocytes within the kidneys, we generated conventional whole-body knockout mice. To validate the genetic manipulation, we performed genotyping of mice using PCR with primers designed to target a region outside the insert, allowing us to distinguish wild-type animals from those carrying the SPA-containing allele (**Figure 7 b**). We confirmed the successful genomic editing in the founder mice (**Figure 7 c**) and by Sanger sequencing (Appendix). Agarose gel electrophoresis of genotyping PCR products shown that heterozygous mice exhibited two amplicons: one specific for the SPA-containing allele (~500 bp) and one for the wild-type allele (~400 bp). Homozygous mice displayed a single band corresponding to the SPA-containing allele at ~500 bp. qPCR performed using RNA isolated from the whole mouse kidneys shown a significant decrease in *Wt1os* expression in the *Wt1os*$^{-/-}$ mice (fold change = 0.001) (**Figure 7 d**).

5.4. *Wt1os*$^{-/-}$ mouse line phenotyping

5.4.1. General features

Wt1os$^{-/-}$ mice were viable and were born at normal Mendelian (1:2:1) and gender (1:1) ratios when bred (**Figure 8 a**). The theoretical probability for the genotypes was: 25% *Wt1os*$^{-/-}$, 25% *Wt1os*$^{+/+}$ and 50% *Wt1os*$^{+/-}$. While female *Wt1os*$^{-/-}$ animals were heavier than wild type controls, male *Wt1os*$^{-/-}$ mice were slightly lighter in comparison to wild type controls (**Figure 8 b**). Interestingly, the survival analysis revealed that *Wt1os*$^{-/-}$ animals have a shortened lifespan, with a median survival of 17 months (**Figure 8 c**).

a

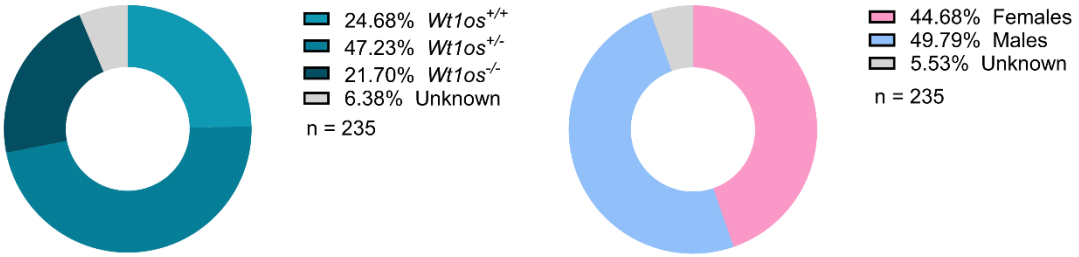

b

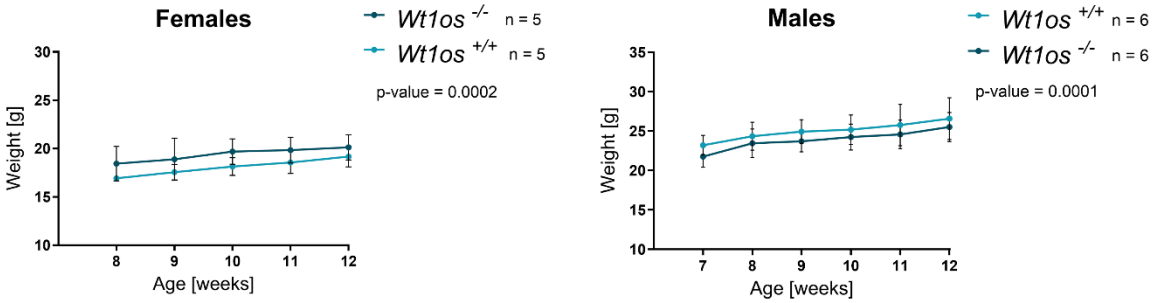

c

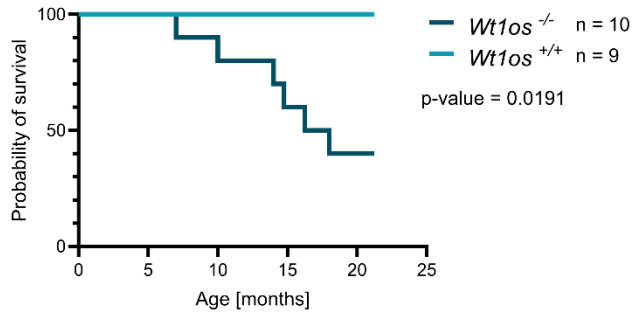

Figure 8. Basic phenotyping of *Wt1os*$^{-/-}$ mouse line.

a. *Wt1os*$^{-/-}$ animals are born at normal Mendelian and gender ratios. Doughnut chart showing the distribution the three possible genotypes and animals of an unknown genotype that died before the age of 3 weeks in percent.

continued on next page

Gender ratios of mice born from breeding of heterozygous *Wt1os*$^{+/-}$ animals. Total animal number: 235. **b. Female homozygous *Wt1os*$^{-/-}$ are slightly heavier than wildtype littermates. While female *Wt1os*$^{-/-}$ animals (dark blue) were slightly heavier than wild type control mice (light blue), male *Wt1os*$^{-/-}$ mice (dark blue) were slightly lighter compared to the controls (light blue).** Two-tailed T test was performed to determine statistical significance: p-value for the female mice: 0.005, p-value for the male mice: 0.0113. **c. *Wt1os*$^{-/-}$ animals show a median lifespan of 17 months.** Survival analysis of *Wt1os*$^{-/-}$ mice. Homozygous *Wt1os*$^{-/-}$ animals show a significantly shorter lifespan compared to the *Wt1os*$^{+/+}$ control mice. Kaplan–Meier curve of *Wt1os*$^{-/-}$ animals and wild type controls. The Gehan-Breslow-Wilcoxon test was performed to determine statistical significance: p-value = 0.0191. Animal number per group: 10.

5.4.2. *Wt1os*$^{-/-}$ mice: kidney morphology and function

To gain insights into kidney morphology and function in the generated *Wt1os*$^{-/-}$ mouse line, we performed kidney tissue analyses along with blood and urine analyses. For this purpose, we used 12- and at least 30-week-old animals. The early timepoint was selected since glomerular development continues postnatally in mice, but kidneys of 12-week-old mice are fully developed, and animals correspond to a young adult human aged 20 to 30 years [130]. By analyzing 30-week-old animals, we aimed to capture any delayed onset of kidney pathology that might not be apparent at an earlier stage.

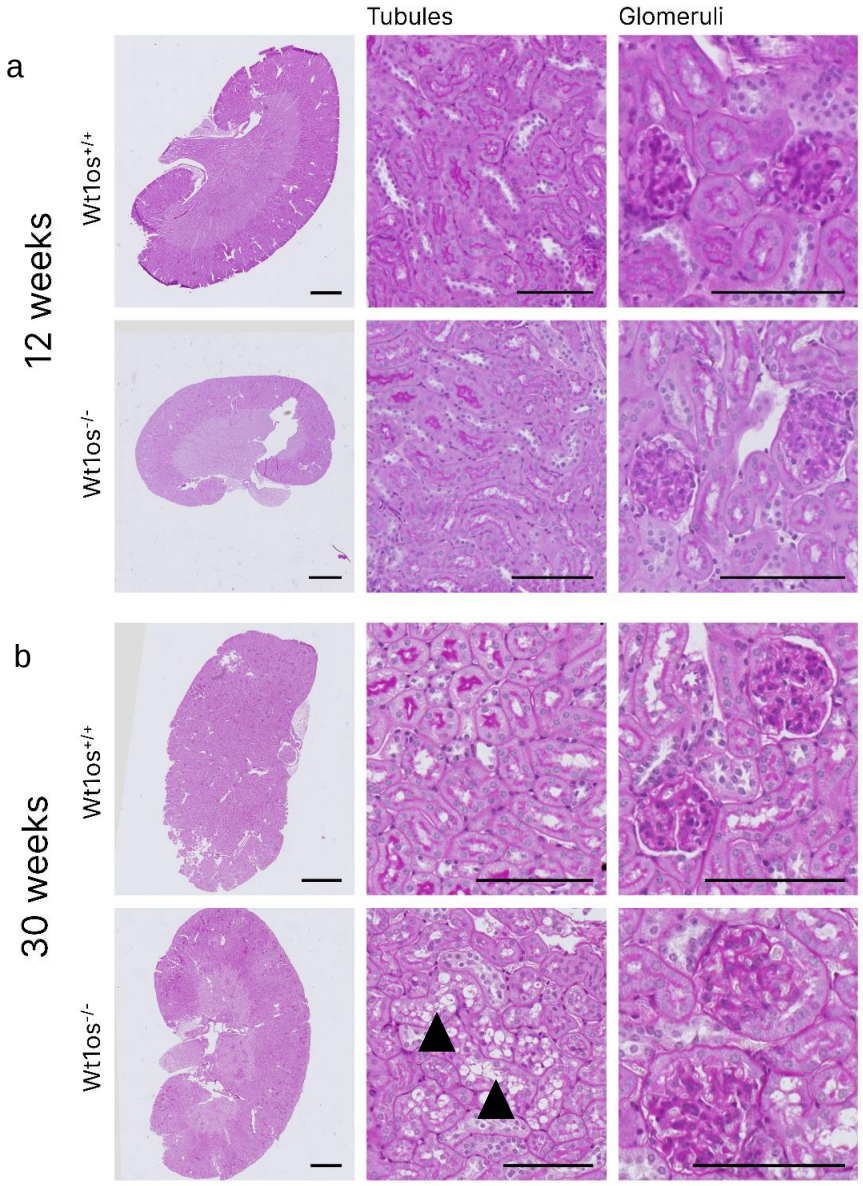

Figure 9. *Wt1os*$^{-/-}$ mice show normal kidney morphology at the age of 12 weeks and mild tubular vacuolization at the age of 30 weeks.

***a*. 12-week-old *Wt1os*$^{-/-}$ mice show healthy kidney morphology.** Histological analysis of 12-week-old *Wt1os*$^{-/-}$ mice shown no difference in kidney morphology, glomeruli distribution and structure compared to control *Wt1os*$^{+/+}$ animals. **b. 30-week-old *Wt1os*$^{-/-}$ mice show altered kidney morphology.** No glomerulosclerosis was observed in the examined tissue sections. Histological analysis indicated tubular vacuolization in the kidneys of 30-week-old *Wt1os*$^{-/-}$ animals. Black arrowheads indicate tubular vacuoles. Brightfield images were acquired with a Hamamatsu S360 slidescanner with a 20x objective. Scale bar on the main picture 1 mm, in ZOOM 100 µm.

Histopathological analysis of PAS (Periodic acid–Schiff) stained kidney tissue sections did not show any morphological abnormalities in the *Wt1os*$^{-/-}$ mice at the age of 12 weeks (**Figure 9 a**). The general morphology, structure, and glomerular distribution in the kidneys of *Wt1os*$^{-/-}$ animals did not differ from ones of the wild type littermates. The analysis of kidney tissue of 30-week-old animals revealed widespread vacuolization in tubular cells throughout the organ (**Figure 9 b**). The phenotype varied among individual animals, with some showing more pronounced changes than others. No glomerular phenotype was observed in the examined PAS-stained tissue sections using standard light microscopy.

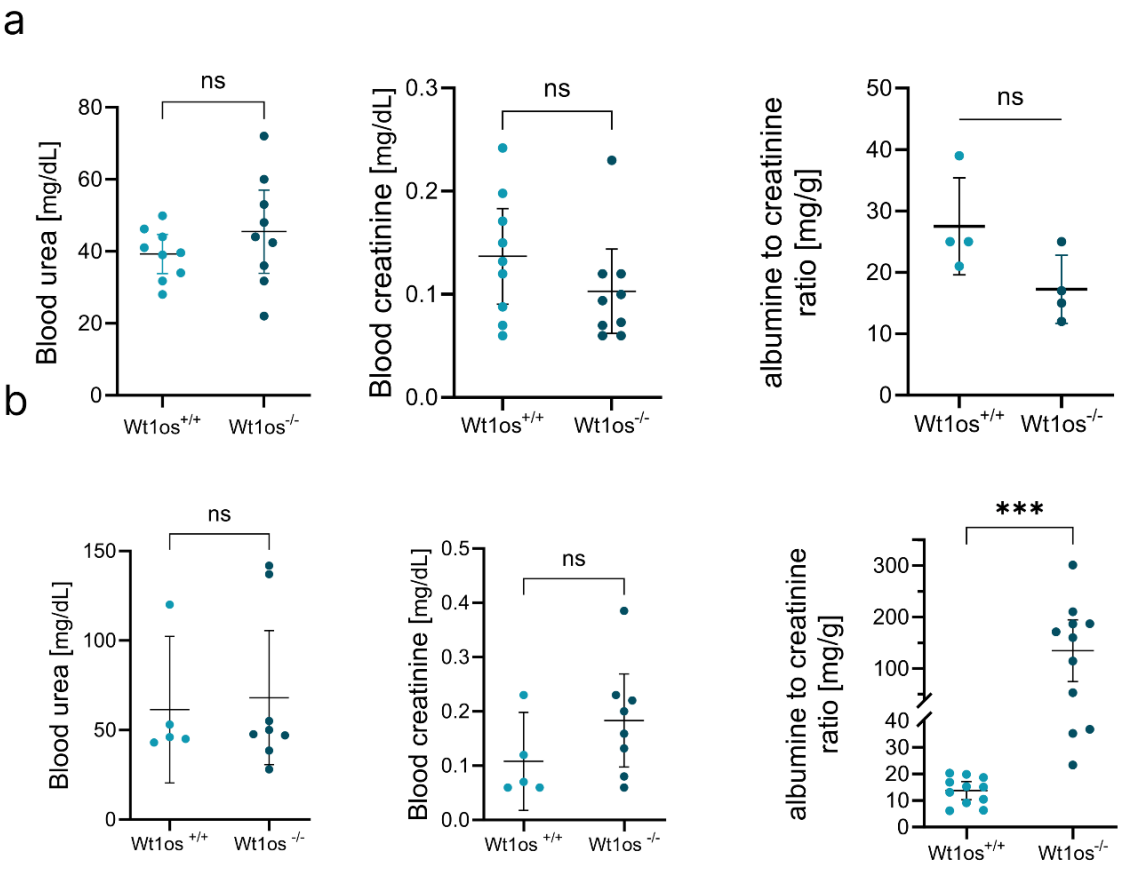

Figure 10. *Wt1os*$^{-/-}$ mice show altered kidney function at the age of 30 weeks.

a. *Wt1os*$^{-/-}$ mice show unaltered kidney function at the age of 12 weeks. Plasma urea and creatinine levels and urine albumin–creatinine ratios (uACRs) indicated that 12-week-old *Wt1os*$^{-/-}$ animals did not show differences in kidney function compared to control *Wt1os*$^{+/+}$ animals. Each dot represents the value originating from 1 mouse. A T-test was performed to determine statistical significance. p-value: ns = not significant). Data are presented as mean with 95% CI.

continued on next page

b**. *Wt1os*$^{-/-}$ mice show altered kidney function at the age of 30 weeks.** While there was no difference in plasma urea and creatinine levels of 30-week-old *Wt1os*$^{-/-}$ animals compared to controls, the *Wt1os*$^{-/-}$ mice shown significantly elevated uACR values indicating increased proteinuria in those animals. Each dot represents the value originating from 1 mouse. A T-test was performed to determine statistical significance. p-value: ns = not significant, *** ≤ 0.001. Data are presented as mean with 95% CI.

We evaluated kidney function by measuring plasma creatinine and urea concentrations and assessed urine albumin-creatinine ratios (uACRs). No significant changes were observed in plasma creatinine and urea levels or uACRs in 12-week-old *Wt1os*$^{-/-}$ animals suggesting no overt phenotype at this stage (
Figure 10. Wt1os-/- mice **show altered kidney function at the age of 30 weeks.**. In contrast, the analysis of 30-week-old mice revealed different findings. Although plasma creatinine and urea levels did not differ between *Wt1os*$^{-/-}$ animals and controls, the *Wt1os*$^{-/-}$ mice exhibited significantly elevated uACRs, which due to its extent reached high statistical significance despite clear interindividual variation (**Figure 10 b**). We didn't observe phenotypic differences between sexes.

5.4.3. In-depth examination of the slit diaphragm in *Wt1os*$^{-/-}$ mice

The significantly elevated uACR pointed towards a relevant podocyte phenotype despite the normal appearance of glomeruli in PAS stainings. This is not unusual and observed clinically in the context of minimal change disease. To examine whether loss of *Wt1os* was associated with changes in podocyte foot process morphology and alterations to the slit diaphragm, we performed immunolabeling of nephrin followed by super-resolution stimulated emission depletion microscopy (STED) imaging of optically cleared kidney samples [67,71]. Nephrin is a crucial component of the SD with the extracellular domain protruding into the gap between adjacent podocytes [16]. STED microscopy enables visualization of proteins like nephrin at the level of individual foot process and allows us to examine the interdigitating pattern of podocyte foot processes and to quantify changes in filtration slit characteristics [67].

In 30-week-old *Wt1os*$^{-/-}$ animals, this approach revealed a mild but clear change in foot process morphology (**Figure 11 a**). FPs of these animals were wider and shortened compared to the control samples which show a regular, uniform SD pattern, a

phenotype in line with podocyte effacement, the paradigmatic morphological pattern in podocyte injury. We used the Automatic Morphological Analysis of Podocytes (AMAP) image quantification tool to analyze the obtained images [67]. SD length per area and foot process circularity were quantified [67]. Morphometric analysis revealed a significantly shortened slit diaphragm length per area, an increased circularity score of the foot processes, and a higher grid index value compared to control animals (**Figure 11 b**). These findings suggest that the loss of *Wt1os* function reduces the filtration surface reflected in the morphological alterations on the level of both global abundance of SD and the individual foot process.

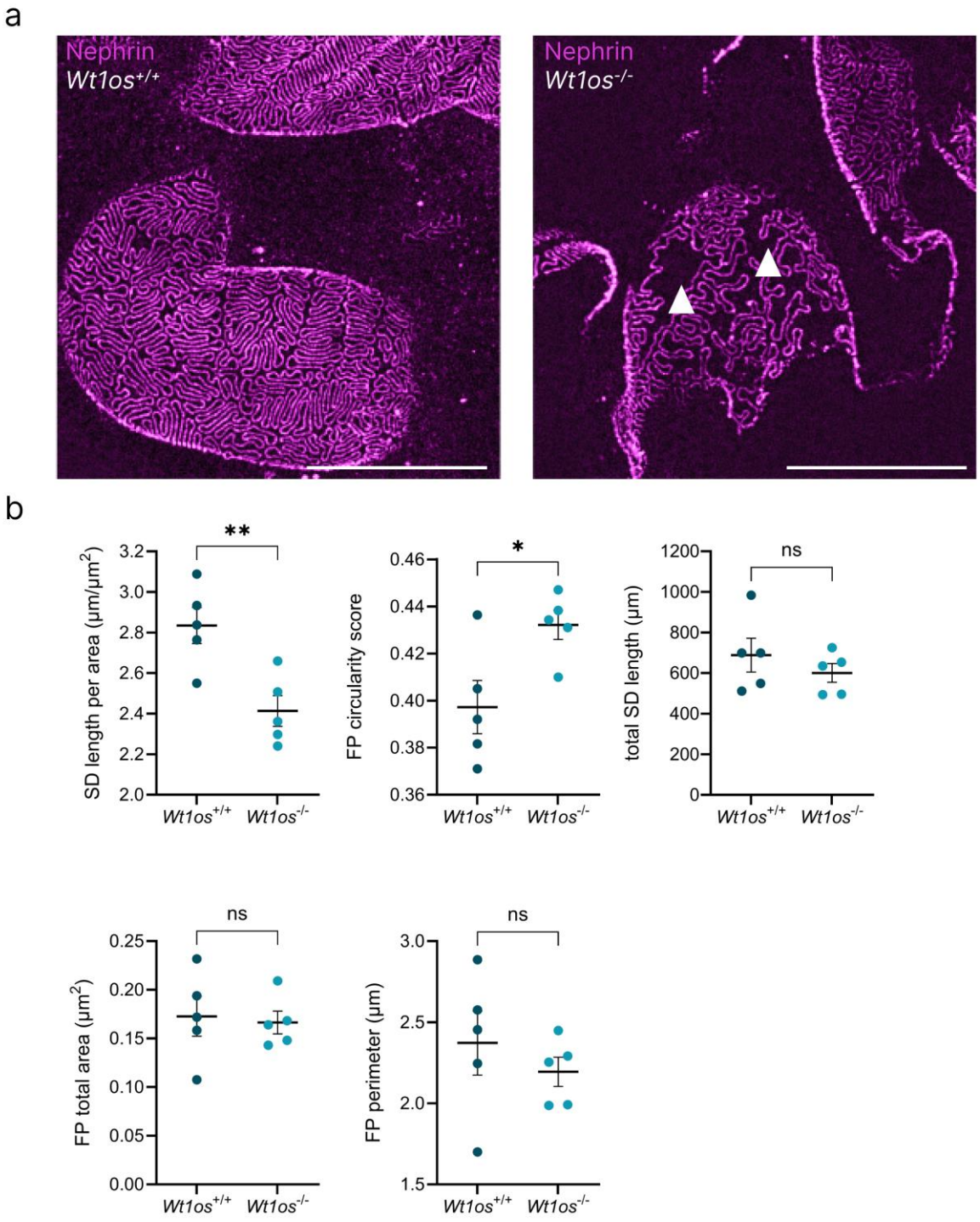

Figure 11. *Wt1os*$^{-/-}$ mice exhibit podocyte foot process effacement at 30 weeks of age.

a. Homozygous 30-week-old *Wt1os*$^{-/-}$ mice show altered podocyte ultrastructure. Following immunolabeling with an anti-nephrin antibody, super resolution microscopy of cleared kidney tissue revealed a regular pattern of the SD in *Wt1os*$^{+/+}$ control animals (left).

continued on next page

In contrast, podocyte foot process effacement is visible in *Wt1os*$^{-/-}$ animals (right). White arrowheads indicate FPE. Images acquired with the TCS SP8 gSTED microscope with a 100x objective. Scale bar: 50 µm. **b. *Wt1os*$^{-/-}$ mice show altered foot process morphology.** Morphometric analysis of SD pattern in STED images demonstrated altered foot processes morphology. SD length per area, foot process circularity, total SD length, FP total area and FP perimeter were quantified: AMAP-based image quantification indicated that *Wt1os*$^{-/-}$ animals shown reduced SD length and increased FP circularity compared to the wild type littermates. Each dot represents the value originating from one mouse. T-test was performed to determine statistical significance. p-value: ns = not significant, * ≤ 0.05, **-≤0.01). Data are presented as mean with SEM.

5.4.4. Characterization of the *Wt1os* transcript isoform pattern in the *Wt1os*$^{-/-}$ mouse line

We confirmed that genomic manipulation was successful and that the SPA was correctly integrated within exon 2 of the *Wt1os* gene. Using qPCR, we demonstrated loss of *Wt1os* in the tissue of *Wt1os*$^{-/-}$ mice (

Figure 7). Considering that lncRNA knockouts cannot be confirmed by checking for loss of protein function, we decided to aim for an in-depth view on alternative transcript isoforms which may result from the mutant locus. To achieve this, we performed a bulk RNA sequencing on isolated glomeruli from *Wt1os*$^{-/-}$ mice and control animals (glomRNAseq). Despite the successful insertion of the SPA and the reduction of *Wt1os* expression in the whole kidney as confirmed by qPCR, transcripts arising from the *Wt1os* locus were still detected in the glomeruli of homozygous *Wt1os*$^{-/-}$ mice. Based on the RNAseq data analysis the global expression level of *Wt1os* was unchanged. Importantly, all *Wt1os* transcripts lacked exon 2 (where the SPA was integrated), which suggested an exon skipping event (**Figure 12 a**). To further investigate these results experimentally, we conducted an end-point RT-PCR experiment using cDNA derived from the whole kidney RNA of *Wt1os*$^{-/-}$ mice and controls. To verify the exclusion of exon 2, we used two primer pairs targeting different regions within exon 2 and exon 3 of *Wt1os* isoforms *Wt1os*-203, *Wt1os*-204 and *Wt1os*-205 (those containing exon 2). The primer pair targeting exon 2 will produce a PCR product only if exon 2 is present. In contrast, the primer pair targeting exon 3 will generate a PCR product regardless of whether exon 2 is skipped, but the product size will vary depending on whether exon 2 is included or excluded (**Figure 12 b**). When amplifying the region exon 1 to exon 2,

shared between the three isoforms, there was no amplicon in the samples from the *Wt1os*$^{-/-}$ animals, whereas samples from the control animals shown a single band at the expected size of around 200 bp. In the PCR reaction targeting the region from exon 1 to exon 3, the control samples displayed two bands: a prominent band at approximately 500 bp and a faint, lighter band at 200 bp. The faint 200 bp band in control animals suggests that the isoform lacking exon 2, undetected in the RNAseq, is present at very low levels also in wildtype animals. The RT-PCR results confirmed the findings from the RNAseq of isolated glomeruli.

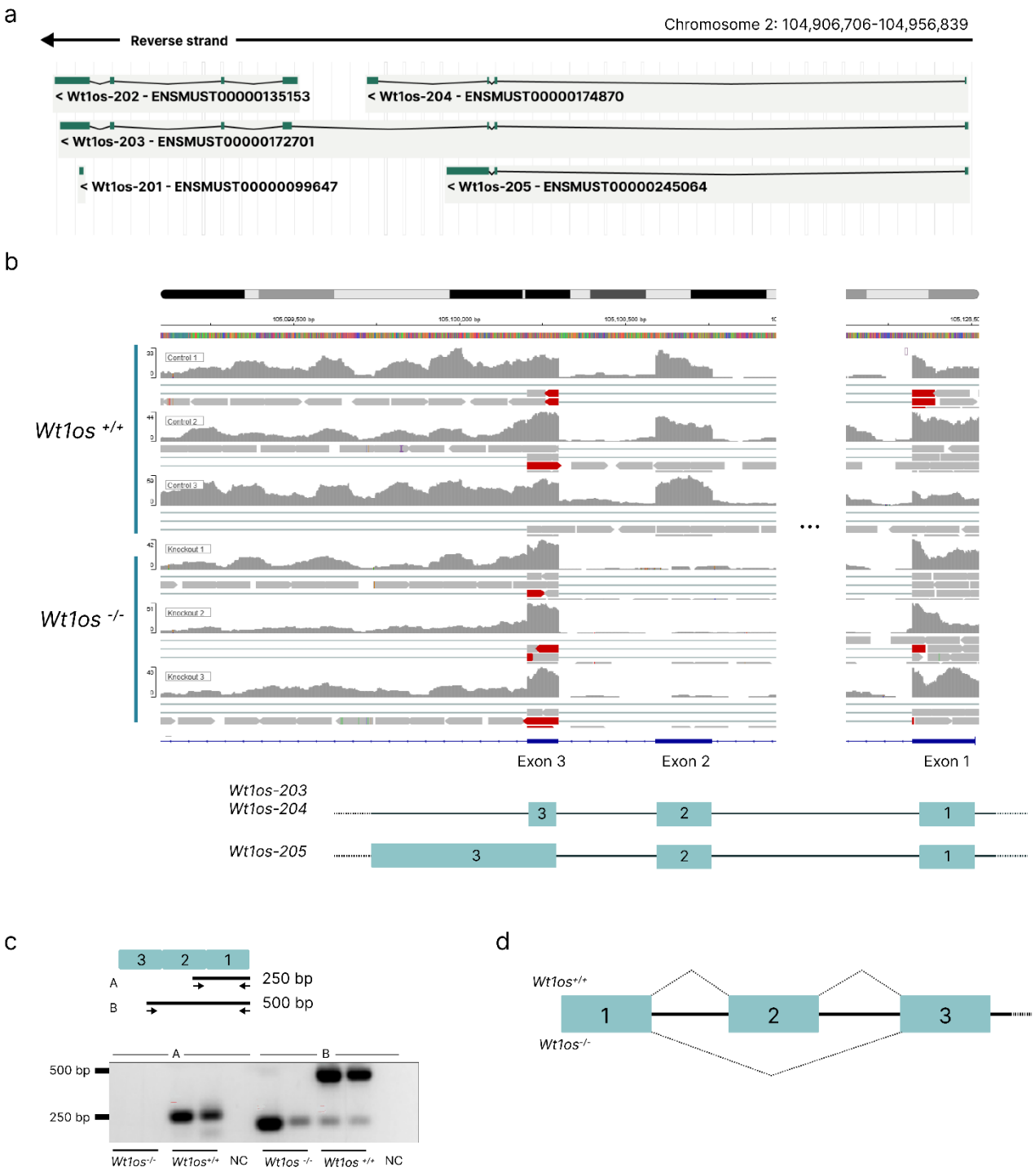

Figure 12. Alternative splicing of *Wt1os* lncRNA in *Wt1os*$^{-/-}$ mice.

a. A schematic representation of *Wt1os* isoforms. Encoded on the reverse strand *Wt1os* has five annotated isoforms named *Wt1os*-201, *Wt1os*-202, *Wt1os*-203, *Wt1os*-204 and *Wt1os*-205. Exons are depicted as blue boxes, connecting black lines represent introns. The figure was based on the Ensembl release 112 - May 2024, gene version: ENSMUSG00000074987.11.

continued on next page

b. RNA sequencing of isolated glomeruli revealed exon 2 skipping event in *Wt1os* lncRNA. Bioinformatic analysis of RNA sequencing data from the glomeruli of *Wt1os*$^{-/-}$ mice shown that nearly no reads mapped to the exon 2 (containing the SPA insert) of the *Wt1os* gene, suggesting an exon 2 skipping event in these animals. The figure depicts a zoomed-in view of the *Wt1os* gene locus, with RNA sequencing reads visualized in the Integrative Genomics Viewer (IGV). The three upper lanes depict results obtained from the control animals; lower three lanes correspond to the *Wt1os*$^{-/-}$ mice. A schematic representation of the *Wt1os* splicing isoforms containing exon 2 is provided below. **c. End-point RT-PCR exon 2 skipping of *Wt1os* in *Wt1os*$^{-/-}$ animals.** To corroborate the RNA sequencing results, we performed RT-PCR using cDNA obtained from the RNA of *Wt1os*$^{-/-}$ mice and control animals. Two primer pairs were designed to target specific regions of the cDNA of isoforms *Wt1os*-203, *Wt1os*-204 and *Wt1os*-205. Primer pair A amplified the region from exon 1 to exon 2 and the region from exon 1 to exon 3 was detected by primer pair B. The blue boxes represent cDNA of *Wt1os* lncRNA. Below, the short black arrows indicate positions of the PCR primers, and the black connecting lines depict the expected PCR products with their sizes expected in the wild type samples. RT-PCR results indicated the absence of the second exon in the *Wt1os* transcript in samples from *Wt1os*$^{-/-}$ animals. The figure shows a 2% agarose gel with amplicons specific to each primer pair. **d. A schematic representation of preferential splicing events in *Wt1os*$^{-/-}$ and control *Wt1os*$^{+/+}$ animals.** Blue boxes represent exons, black connecting lines represent introns. Dashed lines indicate the preferential splicing events in each genotype.

To further investigate the impact of the *Wt1os* mutation on the gene expression profile, we performed a differential transcript usage (DTU) analysis. Firstly, we assessed the expression levels of each splicing isoform of the *Wt1os*. The analysis revealed isoform switching in the isoforms of the *Wt1os.* Specifically, there was a decrease in the expression of the *Wt1os*-204 (ENSMUST00000174870) accompanied by an upregulation of the *Wt1os*-202 (ENSMUST00000135153) in the *Wt1os*$^{-/-}$ animals (**Figure 13 a**). Given the phenotypic changes observed in *Wt1os*$^{-/-}$ mice and the established link of *Wt1* downregulation with FSGS, we aimed to confirm that the observed phenotypic changes were specifically due to *Wt1os* loss. To this end, we assessed *Wt1* expression levels and found no significant differences between *Wt1os*$^{-/-}$ mice and controls (**Figure 13 a**). Gene Ontology (GO) terms related to the genes identified in the DTU analysis indicate an effect on i.a. GTPase regulator and activator activity (**Figure 13 b**).

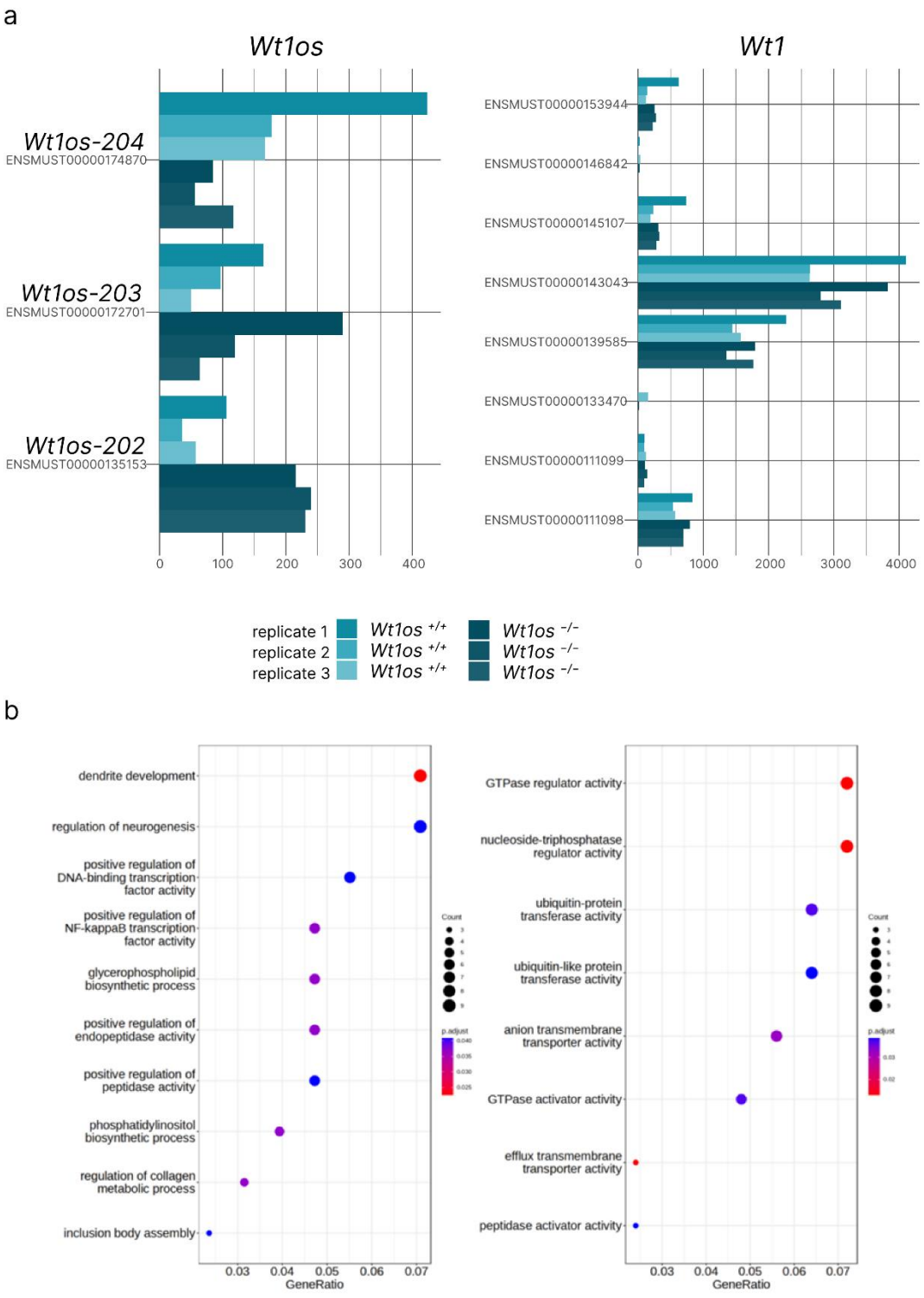

Figure 13. RNAseq reveals differential transcript usage and isoform switching of *Wt1os* lncRNA in *Wt1os*$^{-/-}$ mice.

a. RNAseq analysis revealed isoform switching among *Wt1os* splicing isoforms in *Wt1os*$^{-/-}$ mice. To further investigate the impact on *Wt1os* mutation, we assessed the expression levels of each splicing isoform of the *Wt1os* and the neighboring *Wt1* genes.

continued on next page

DTU analysis detected a downregulation of the *Wt1os-204* isoform and an upregulation of the *Wt1os-202* isoform, with no significant changes in the expression of the *Wt1os-203* isoform. No differences in the expression levels of Wt1 splicing isoforms were observed. Bar plots show the scaled expression (dtuScaledTPM) of the three *Wt1os* isoforms and eight *Wt1* across individual replicates. **b. Differential transcript usage analysis reveals an effect on GTPase regulator activity.** Gene Ontology (GO) terms associated with the genes differentially used transcripts indicate an effect on i.a. GTPase regulator and activator activity. Dot plots show the top 20 GO terms in the GO enrichment analysis. The size of each dot represents the number of genes associated with each term, while the color indicates the adjusted p-value. The Y-axis represents the GO terms, and the X-axis represents the proportion of genes associated with each GO term.

5.5.5. Loss of *Wt1os* has a mild but distinct impact on the glomerular transcriptome

To determine the impact of the *Wt1os* mutation on the glomerular transcriptome, we performed a differential gene expression (DGE) analysis of the glomRNAseq data. In the initial step of the analysis, we conducted principal component analysis (PCA) to assess sample separation. The results revealed clear separation along the second principal component (PC2), which accounts for 21% of the total variance (**Figure 14 a**). Loss of *Wt1os* resulted in dysregulation of a limited number of genes, with 16 genes identified as differentially regulated (with 6 up-, and 10 downregulated genes) (**Figure 14 b**). Gene Set Enrichment Analysis (GSEA) revealed enrichment of various metabolic process-related terms (**Figure 14 c**).

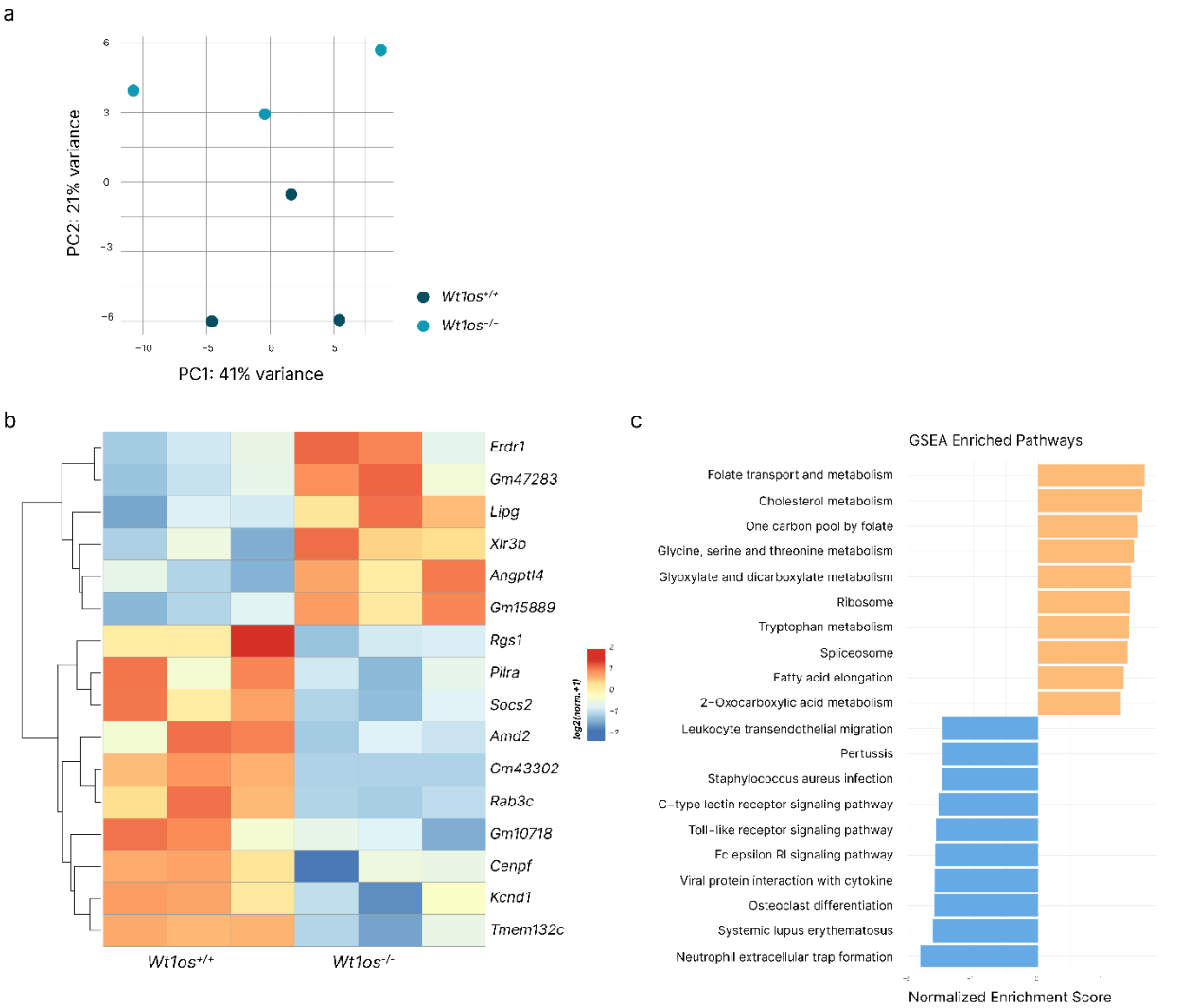

Figure 14. RNAseq reveals mild but distinct transcriptome changes in glomeruli of *Wt1os*$^{-/-}$ mice.

a. RNAseq samples separate according to the second principal component (PC2). Principle Component Analysis (PCA) plot shows separation of glomRNAseq samples by genotype. Samples from *Wt1os*$^{+/+}$ and *Wt1os*$^{-/-}$ genotypes separated along the second principal component (PC2), accounting for 21% of the observed variance. Each genotype is represented by three replicates. **b. 16 genes were significantly regulated in the *Wt1os*$^{-/-}$ animals.** A heatmap displaying the results of differential gene expression (DGE) analysis performed using the DESeq2 package. 16 genes were found to be differentially expressed in the glomeruli of *Wt1os*$^{-/-}$ mice compared to control animals. Among these, six genes were upregulated (depicted in red), and ten genes were downregulated (depicted in blue). Gene expression levels are presented as $\log_2$ (normalized counts+1).

continued on next page

c. Differentially regulated genes in *Wt1os*$^{-/-}$ mice are related to spliceosome, metabolism, and immune pathways. Two-side bar plot of the top enriched pathways associated with the differentially regulated genes identified in the Gene Set Enrichment Analysis (GSEA). Terms with positive Normalized Enrichment Score (NES) relate to the upregulated gene sets (orange bars), terms with a negative NES correspond to the downregulated gene sets in the *Wt1os*$^{-/-}$ mice (blue bars).

5.5. Characterization of mouse *Wt1os* and human *WT1-AS* lncRNAs in cultured podocytes

5.5.1. *WT1-AS* is a nuclear lncRNA

To explore the function of *Wt1os in vitro*, we employed two immortalized podocyte cell lines, mouse (HSMP – Heat Sensitive Mouse Podocytes) and human (AB8) cultured podocytes. We generated bulk RNAseq data of both differentiated cell lines and we discovered that while the human podocytes expressed the human lncRNA *WT1-AS* on a decent level, mouse cultured podocytes demonstrated very low expression of *Wt1os* (Table 30 *Wt1os* and *WT1-AS* expression in the cultured podocyte cell lines).

Table 30 *Wt1os* and *WT1-AS* expression in the cultured podocyte cell lines.

			Normalized read count	
Cell line	Gene name	Ensembl ID	Replicate 1	Replicate 2
HSMP (mouse)	*Wt1os*	ENSMUSG00000074987	3.1	1.2
AB8 (human)	*WT1-AS*	ENSG00000183242	59.5	63.9

To further characterize *WT1-AS* in cultured human podocytes, we first performed an RNAScope in situ hybridization staining to define its subcellular localization. The quantification of the RNA staining indicated that *WT1-AS* is present nearly exclusively in the nucleus (**Figure 15 a-b**).

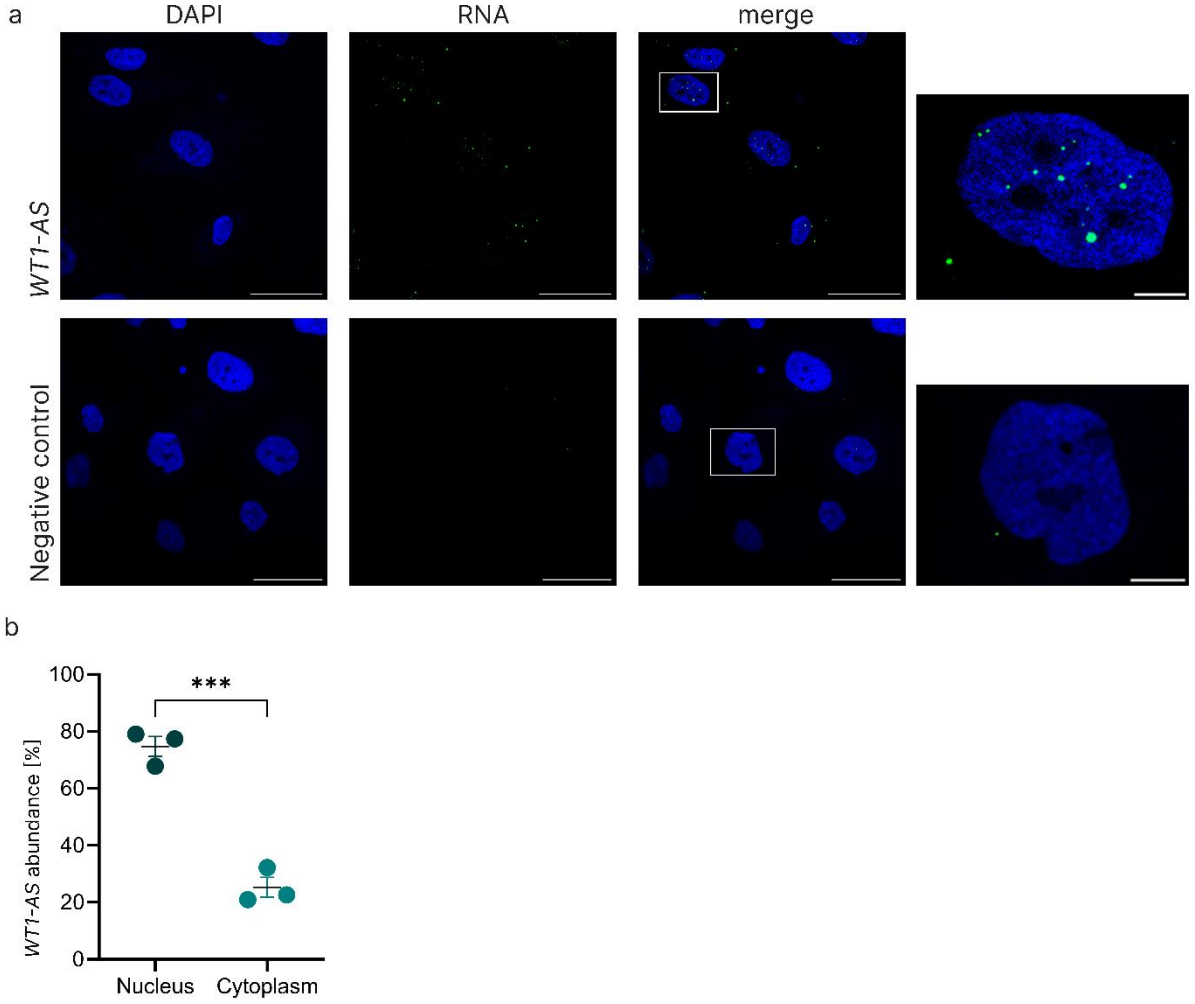

Figure 15. *WT1-AS* is a nuclear lncRNA.

a. *WT1-AS* is present in the nucleus. RNAScope In situ hybridization (ISH) staining of *WT1-AS* in human cultured podocytes demonstrated primarily nuclear localization of the lncRNA. A probe targeting a bacterial RNA served as a negative control. Nuclei were counterstained with DAPI. Scale bars: 100 µm (overview) and 10 µm (zoomed view). **b. Signal quantification of *WT1-AS* RNAscope RNA ISH staining.** RNA signal was quantified as the number of dots per nucleus compared to the number of dots per cytoplasm. Each dot represents the mean value from one biological replicate containing 100 cells. Statistical significance was assessed using a t-test ($p \leq 0.001$-***). Data are presented as mean ± SEM.

5.5.2. *WT1-AS* knockdown in cultured human podocytes leads to cell death

To investigate the effects of loss of *WT1-AS* lncRNA on human podocytes, we employed a targeted knockdown (KD) strategy using GapmeRs and confirmed the knockdown efficiency via qPCR (**Figure 16 a**). Forty-eight hours post-transfection, we

observed a reduction in cell numbers in the transfected dishes compared to the controls. To assess this further, we conducted live-cell imaging using the Incucyte system (Sartorius), culturing the cells with the cell death marker DiYO1. This analysis revealed extensive cell death in human podocytes following *WT1-AS* knockdown (**Figure 16 b**). Twenty-four hours after knockdown of *WT1-AS*, we performed qPCR to assess the expression levels of seven genes previously identified as differentially expressed in the glomeruli of *Wt1os*$^{-/-}$ mice which were expressed in our cell culture model (**Figure 14 cFigure 14**). Among these, *RGS1*, a gene found to be downregulated in the glomRNAseq of *Wt1os*$^{-/-}$ mice was similarly downregulated after *WT1-AS* knockdown (**Figure 17 a**).

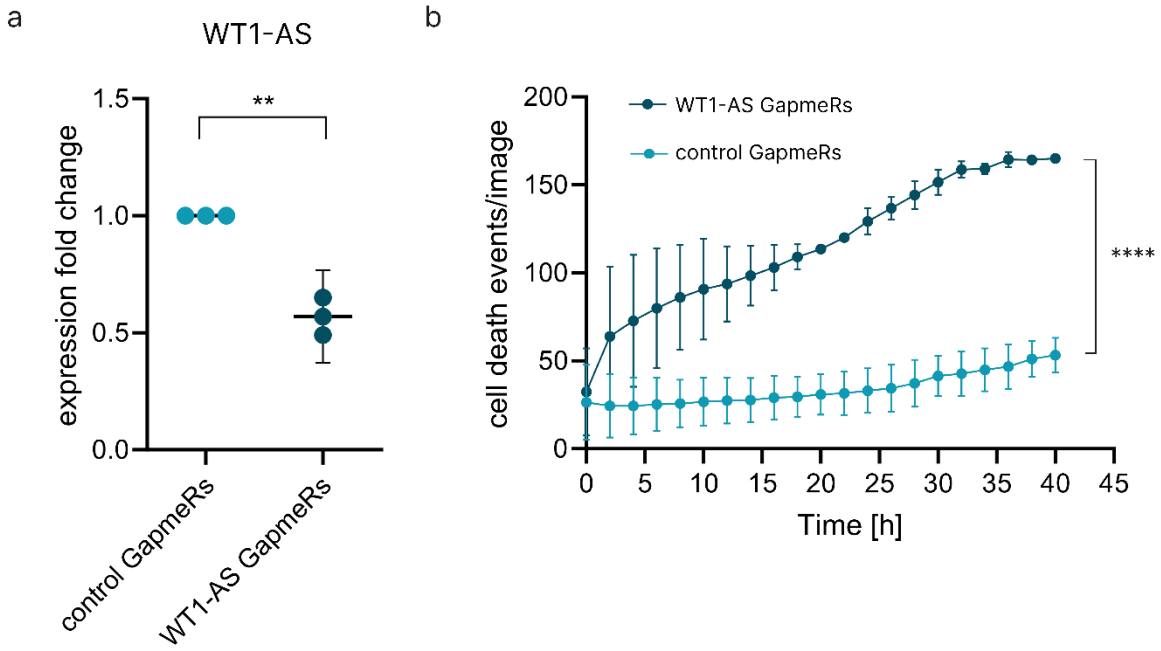

Figure 16. GapmeR-mediated *WT1-AS* knockdown in human cultured podocytes leads to cell death

a. *WT1-AS* expression is significantly downregulated upon GapmeRs-mediated knockdown in human cultured podocytes. *WT1-AS* expression was significantly reduced upon treatment with *WT1-AS* targeting GapmeRs in comparison to treatment with control non-targeting GapmeRs. The graph depicts the qPCR data derived from human cultured podocytes transfected with *WT1-AS*-targeting GapmeRs normalized to the cells transfected with control non-targeting GapmeRs. *WT1-AS* expression was normalized to HPRT1 expression. Data are presented as mean with 95% CI. A T-test was performed to determine statistical significance.

continued on next page

b. *WT1-AS* knockdown in the human cultured podocytes induces cell death. Following the transfection with GapmeRs targeting *WT1-AS*, live-cell imaging was conducted using the cell death marker DiYO1. The analysis revealed a significant increase of cell death post-transfection. The graph depicts the live cell imaging data derived from human cultured podocytes transfected with *WT1-AS*-targeting GapmeRs in comparison to the cells transfected with control non-targeting GapmeRs. Each dot represents the mean number of cell death events (DiYO1 positive green fluorescent signal) averaged from three biological replicates. Nine pictures per replicate were analyzed. Data are presented as mean with SD.

5.5.3. WT1-AS and *RGS1* demonstrate mutual expression regulation in cultured human podocytes

To investigate the effect of *RGS1* gene modulation on *WT1-AS* expression in AB8 cells, we examined *WT1-AS* levels following *RGS1* upregulation. Since *WT1-AS* knockdown led to *RGS1* downregulation and resulted in cell death, we aimed to determine whether *RGS1* upregulation could influence *WT1-AS* expression. To achieve this, we used the AB8.dCas9.VP64 cells to perform CRISPRa-mediated activation of *RGS1* [131–133]. CRISPRa uses the catalytically inactive Cas9 (dCas9) fused to a transcription activation domain guided to the specific transcription start site by the guide RNA (sgRNA) [131–133]. Using the lentiviral transduction, we generated a human podocyte cell line stably expressing dCas9 fused to the VP64 activator domain (AB8.dCas9.VP64). Successful integration and expression of dCas9.VP64 was confirmed by western blotting against Cas9 (**Figure A. 6**). The qPCR results revealed that *RGS1* upregulation leads to *WT1-AS* upregulation (**Figure 17 b**) indicating a potential positive feedback regulation of the two genes.

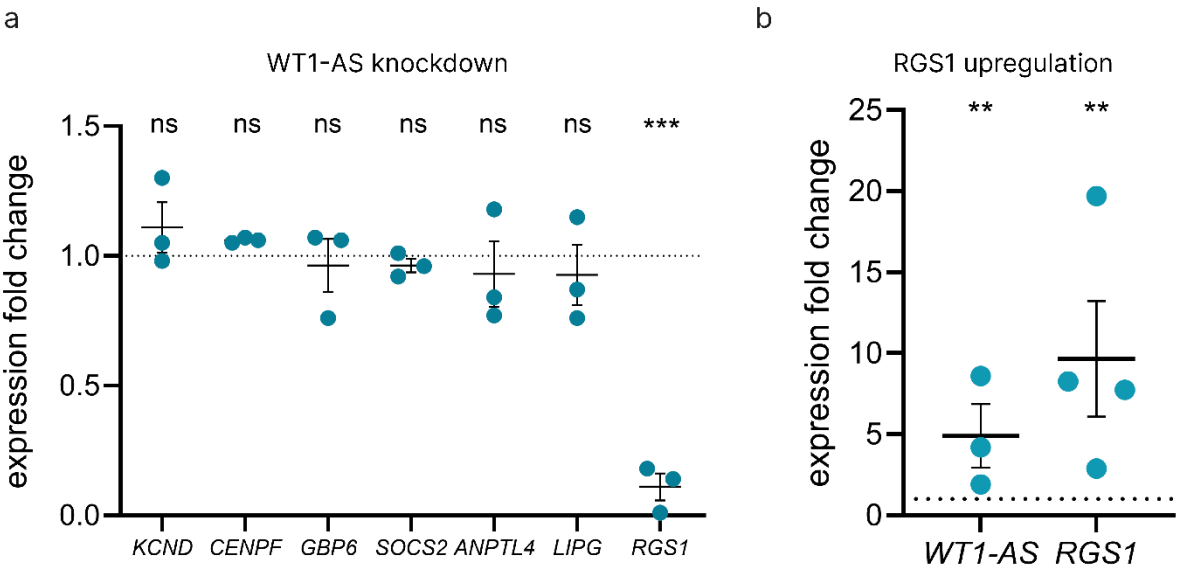

Figure 17. *WT1-AS* and *RGS1* demonstrate mutual expression regulation.

a. *WT1-AS* knockdown in cultured podocytes downregulates *RGS1* expression. The qPCR analysis shows a significant reduction in *RGS1* mRNA levels following the lncRNA knockdown. The figure also includes relative expression levels of genes previously identified as differentially regulated in the glomeruli of *Wt1os*-/- mice. The graph depicts the qPCR data derived from human cultured podocytes transfected with *WT1-AS*-targeting GapmeRs normalized to the cells transfected with control non-targeting GapmeRs. Gene expression was normalized to HPRT1 expression. Data are presented as mean with 95% CI. A T-test was performed to determine statistical significance. **b. Upregulation of *RGS1* leads to upregulation of *WT1-AS*.** The qPCR analysis shows an upregulation of *WT1-AS* lncRNA upon CRISPRa-mediated upregulation of *RGS1*. The graph depicts the qPCR data derived from human cultured podocytes transfected with *RGS1* targeting sgRNA normalized to the cells transfected with control non-targeting sgRNA. The genes' expression was normalized to HPRT1 expression. The dotted line indicates the fold change of control value equal to 1. Data are presented as mean with 95% CI. (p-value: ****≤0.0001, *** ≤0.001, ns – not significant).

5.5.4. CRISPRa-mediated *Wt1os* expression activation

Given that *WT1-AS* knockdown in human podocytes led to cell death, we decided to investigate the function of *Wt1os* further using the cultured mouse podocytes. Due to the very low expression of the lncRNA in this cell line (**Table 30**), we opted to activate its expression using the CRISPRa system [131–133]. Activating the expression of *Wt1os* was accomplished by transient transfection of sgRNA targeting the *Wt1os* promoter. We validated successful gene expression activation using qPCR (

Figure 18 a). We defined the subcellular localization of *Wt1os* using RNAscope RNA ISH and similarly to the results from the human podocytes (**Figure 15**), we observed *Wt1os* mainly in the nucleus (**Figure 18**).

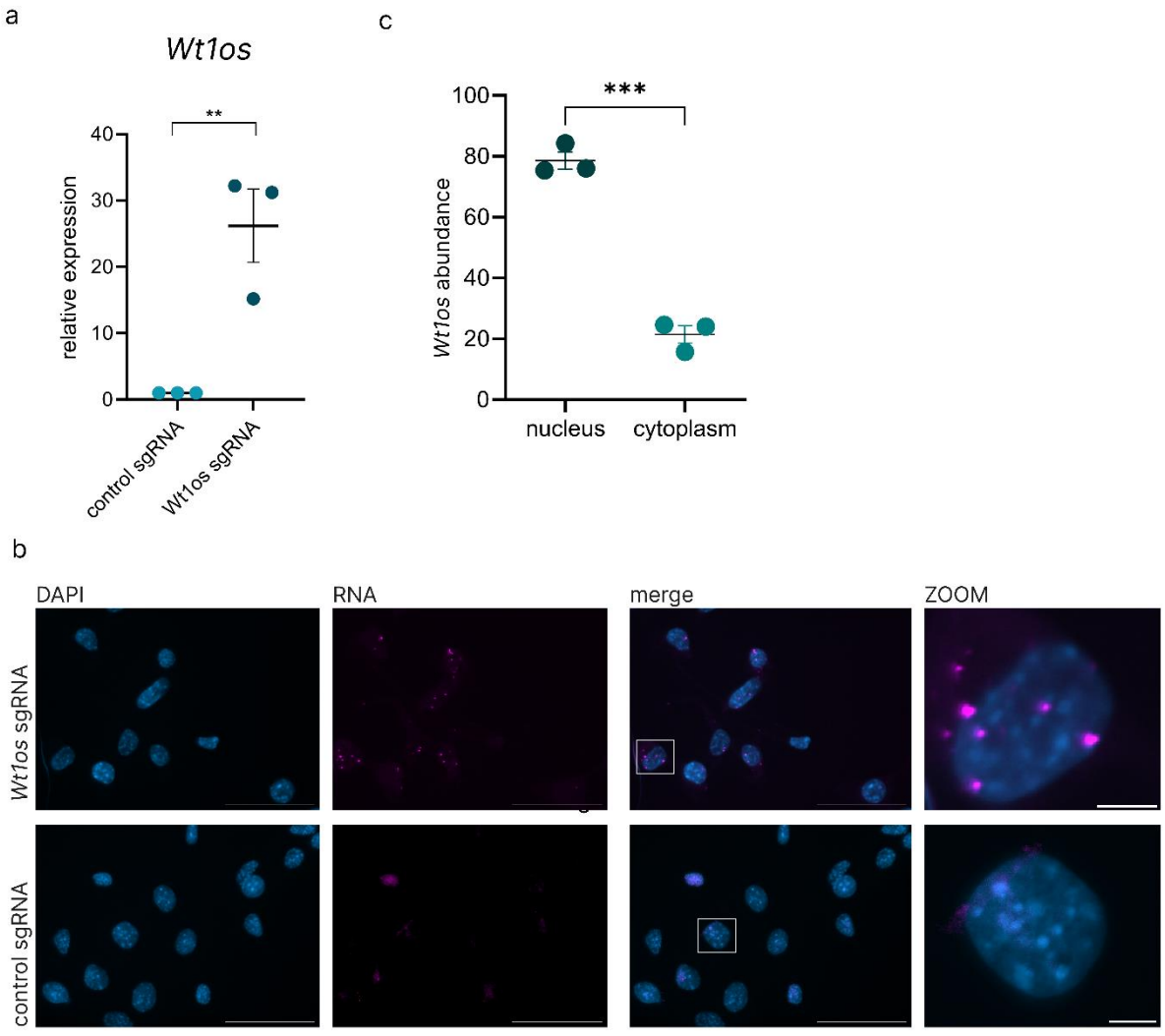

Figure 18. *Wt1os* is a nuclear lncRNA.

a. *Wt1os* is significantly upregulated after CRISPRa-mediated gene expression activation in mouse cultured podocytes. *Wt1os* expression was significantly elevated upon treatment with *Wt1os* targeting sgRNA in comparison to treatment with control non-targeting sgRNA. The graph depicts the qPCR data derived from mouse cultured podocytes transfected with sgRNA targeting the *Wt1os* promoter normalized to the cells transfected with control non-targeting sgRNA. *Wt1os* expression was normalized to Hprt1 expression

continued on next page

b. *Wt1os* is present mainly in the nucleus. Activation of *Wt1os* expression was accomplished by transient transfection of HSMPS.dCas9.VP64 cell line with custom-designed sgRNAs targeting the *Wt1os* promoter. RNAscope RNA ISH staining of *Wt1os* demonstrated nuclear localization of *Wt1os* lncRNA. Nuclei were counterstained with DAPI. Scale bars: 50 µm (overview) and 5 µm (zoomed view). **c. Signal quantification of *Wt1os* RNAscope RNA ISH staining.** RNA signal was quantified as the number of dots per nucleus compared to the number of dots per cytoplasm. Each dot represents the mean value from one biological replicate containing 50 cells. Statistical significance was assessed using a t-test. Data are presented as mean with 95% CI. T-test was performed to determine statistical significance. (p-value **≤0.01, ***≤0.001)

5.5.5. *Wt1os* expression activation leads to *Rgs1* upregulation

After activating *Wt1os* expression in mouse podocytes, we conducted qPCR to evaluate the expression levels of genes previously identified as differentially expressed in the glomeruli of *Wt1os*$^{-/-}$ mice (**Figure 14**). Notably, the *Rgs1* gene was upregulated, consistent with our earlier findings, where *Rgs1* was downregulated in the glomRNAseq analysis of *Wt1os*$^{-/-}$ mice (**Figure 20 a**). Since *Wt1os* and Wt1 share a bidirectional promoter, the CRISPRa-mediated activation is expected to upregulate both genes. To determine whether the *Rgs1* regulation was dependent on *Wt1os* alone or also influenced by Wt1, we measured the expression of *Rgs1* following Wt1 knockdown in the *Wt1os*-expressing cells. We first established siRNA-mediated Wt1 knockdown (**Figure 19 b**). Cells with *Wt1os* activation were transfected with either or a non-targeting control siRNA (*Wt1os*^{act}) or Wt1-targeting siRNA (*Wt1os*^{act} + Wt1^{kd}) to maintain *Wt1os* expression while knocking down Wt1. *Rgs1* expression remained unchanged upon Wt1 knockdown, suggesting that its regulation by *Wt1os* is independent of Wt1 (**Figure 19 c**).

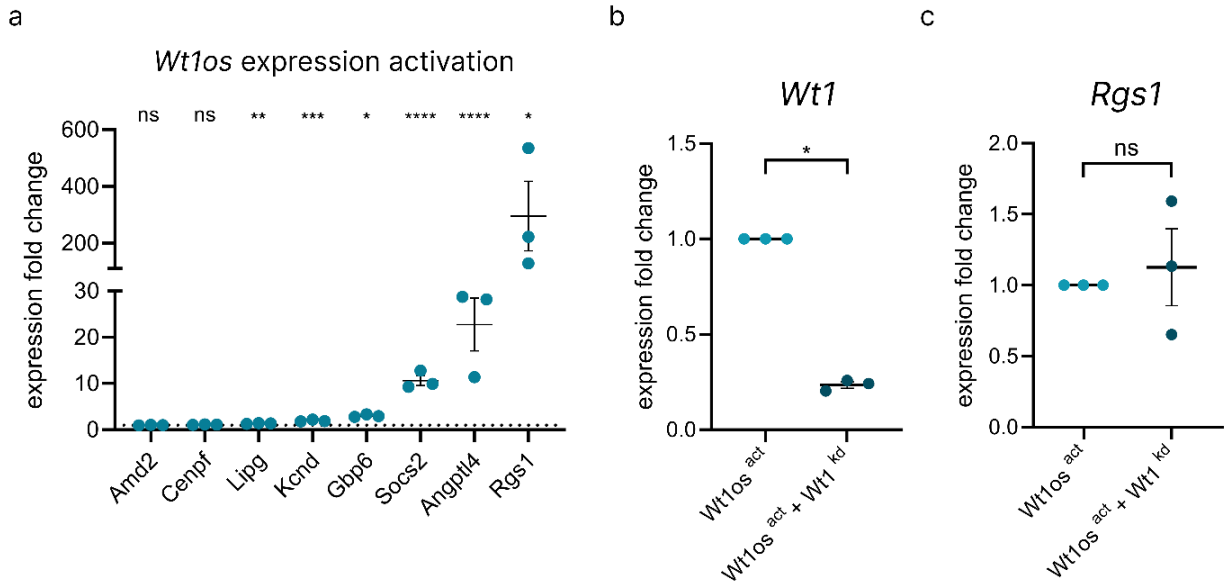

Figure 19. *Wt1os* expression activation leads to *Rgs1* upregulation independently from *Wt1.*

a. Activation of *Wt1os* expression in mouse podocytes leads to *Rgs1* upregulation. The qPCR analysis shows a significant upregulation of *Rgs1* mRNA levels following *Wt1os* expression activation. The figure also includes relative expression levels of genes previously identified as differentially regulated in the glomeruli of *Wt1os*-/- mice. The graph depicts the qPCR data derived from HSMPS.dCas9.VP64 cells transfected with sgRNA targeting *Wt1os* promoter in comparison to the cells transfected with non-targeting sgRNA as control. A T-test was performed to determine statistical significance. The dotted line indicates the fold change of control value equal to 1. **b. Wt1 expression is significantly downregulated upon siRNA-mediated knockdown in mouse cultured podocytes.** Wt1 expression was significantly reduced upon treatment with *Wt1* targeting siRNA in comparison to treatment with control non-targeting siRNA. The graph depicts the qPCR data derived from mouse cultured podocytes expressing *Wt1os* (*Wt1os* ^{act}) transfected with Wt1-targeting siRNA normalized to the cells transfected with control non-targeting siRNA. Wt1 expression was normalized to Hprt1 expression. Data are presented as mean with 95% CI. A T-test was performed to determine statistical significance. **c. *Rgs1* expression is not changed upon siRNA-mediated knockdown in mouse cultured podocytes.** *Rgs1* expression did not change upon treatment with *Wt1* targeting siRNA in comparison to treatment with control non-targeting siRNA. The graph depicts the qPCR data derived from mouse cultured podocytes expressing *Wt1os* (*Wt1os* ^{act}) transfected with Wt1-targeting siRNA normalized to the cells transfected with control non-targeting siRNA. *Rgs1* expression was normalized to Hprt1 expression. Data are presented as mean with 95% CI. A T-test was performed to determine statistical significance.

Rgs1 belongs to the family of G-protein signaling regulators[134]. The protein binds to the GTP-bound G alpha subunits and acts as a GTPase activating protein (GAP)[134,135]. By accelerating the hydrolysis of the GTP to GDP, *Rgs1* attenuates the signaling initiated by G protein-coupled receptors (GPCRs) [134,135]. Given the role of Rgs1 in cell migration [136] and calcium signaling [137,138], we decided to investigate these two cellular phenotypes. Cellular migration was assessed using a wound-healing (scratch) assay, while calcium dynamics was examined with a live cell imaging-based approach.

5.5.6. *Wt1os* promotes podocytes migration independent from *Rgs1*

To investigate the role of *Wt1os* in podocytes migration a scratch was introduced in the cell monolayer, and its surface area was measured immediately and again after 24 hours. We examined four conditions: 1. *Wt1os* expression activation (*Wt1os*^{act}), 2. simultaneous *Rgs1* knockdown alongside *Wt1os* activation (*Wt1os*^{act}+*Rgs1*^{kd}), 3. *Rgs1* knockdown (*Rgs1*^{kd}) and 4. cells transfected with control siRNA and non-targeting control sgRNA (control). Cells with *Wt1os* expression activation (*Wt1os*^{act}) exhibited significantly faster scratch closure compared to control condition, indicating a pro-migratory effect of the lncRNA. Interestingly, cells with both *Wt1os* activation and *Rgs1* knockdown (*Wt1os*^{act}+*Rgs1*^{kd}) displayed a migration rate comparable to that observed with *Wt1os* activation alone. This finding suggests that the pro-migratory effect of *Wt1os* is independent of *Rgs1* (**Figure 20 b**).

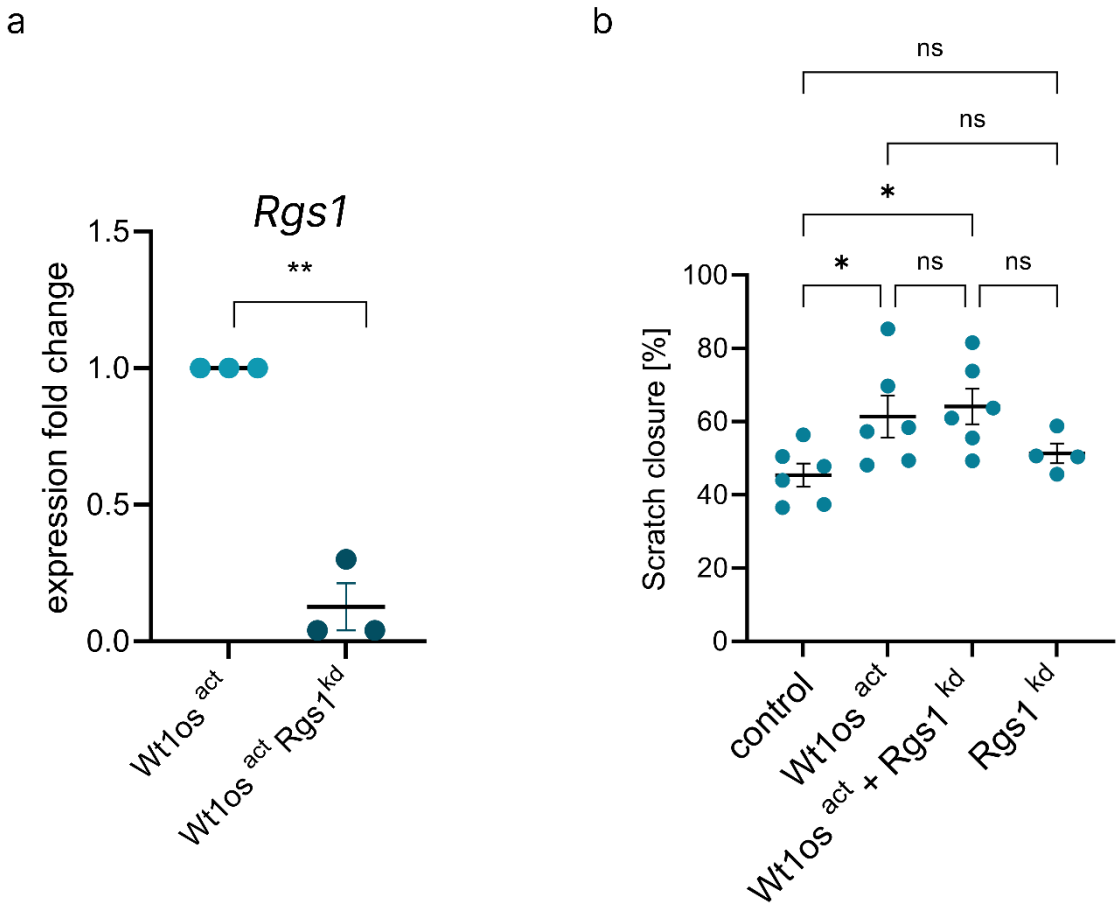

Figure 20. *Wt1os* promotes podocytes migration independently from *Rgs1.*

a. *Rgs1* expression is significantly downregulated upon siRNA-mediated knockdown in mouse cultured podocytes. *Rgs1* expression was significantly reduced upon treatment with *Rgs1* targeting siRNA in comparison to treatment with control non-targeting siRNA. The graph depicts the qPCR data derived from mouse cultured podocytes expressing *Wt1os* (*Wt1os* ^{act}) transfected with *Rgs1*-targeting siRNA normalized to the cells transfected with control non-targeting siRNA. *Rgs1* expression was normalized to Hprt1 expression. Data are presented as mean with 95% CI. A T-test was performed to determine statistical significance**. b. *Wt1os* promotes migration of podocytes.** The wound-healing assay analysis shows a pro-migratory effect of *Wt1os* independently from *Rgs1*. The graph depicts the scratch closure [%] 24h after introducing a scratch in a confluent cell well. control = HSMPS.dCas9.VP64 cells, *Wt1os*^{act} = HSMPS.dCas9.VP64 cells with activation of *Wt1os*, *Wt1os*^{act} + *Rgs1*^{kd}= HSMPS.dCas9.VP64 cells with activation of *Wt1os* and *Rgs1* knockdown, *Rgs1*^{kd} = HSMPS.dCas9.VP64 with *Rgs1* knockdown. One-Way ANOVA was performed to determine statistical significance. (p-value: *≤0.05, **≤0.01, ns – not significant).

5.5.7. *Wt1os* enhances calcium mobilization in response to ATP in a *Rgs1*-dependent manner

To investigate the role of *Wt1os* in Ca^{2+} dynamics, we performed live-cell calcium imaging in ATP-stimulated cultured mouse podocytes. The direct consequence of ATP stimulation is the release of calcium from the endoplasmic reticulum stores into the cytosol[139]. Again, we examined four conditions: 1. *Wt1os* expression activation (*Wt1os*^{act}), 2. simultaneous *Rgs1* knockdown alongside *Wt1os* activation (*Wt1os*^{act} + *Rgs1*^{kd}), 3. *Rgs1* knockdown (*Rgs1*^{kd}) and 4. cells transfected with control siRNA and non-targeting control sgRNA (control). Podocytes were incubated with Fluo-4 AM, a calcium-sensitive probe which indicates intracellular free calcium levels [140]. Cells with *Wt1os* activation, which leads to upregulation of *Rgs1* (as shown in **Figure 19**), exhibited a greater Ca^{2+} store release upon ATP stimulation when compared to control conditions (**Figure 21 a**). The higher signal-to-noise ratio of the fluorescence signal suggests that *Wt1os* activation enhances calcium signaling. However, in cells with both *Wt1os* activation and *Rgs1* knockdown, the signal-to-noise ratio was comparable to that of control conditions (**Figure 21 b**). This finding suggests that *Wt1os*-mediated calcium signaling is dependent on *Rgs1*, indicating a genetic interaction between the two genes.

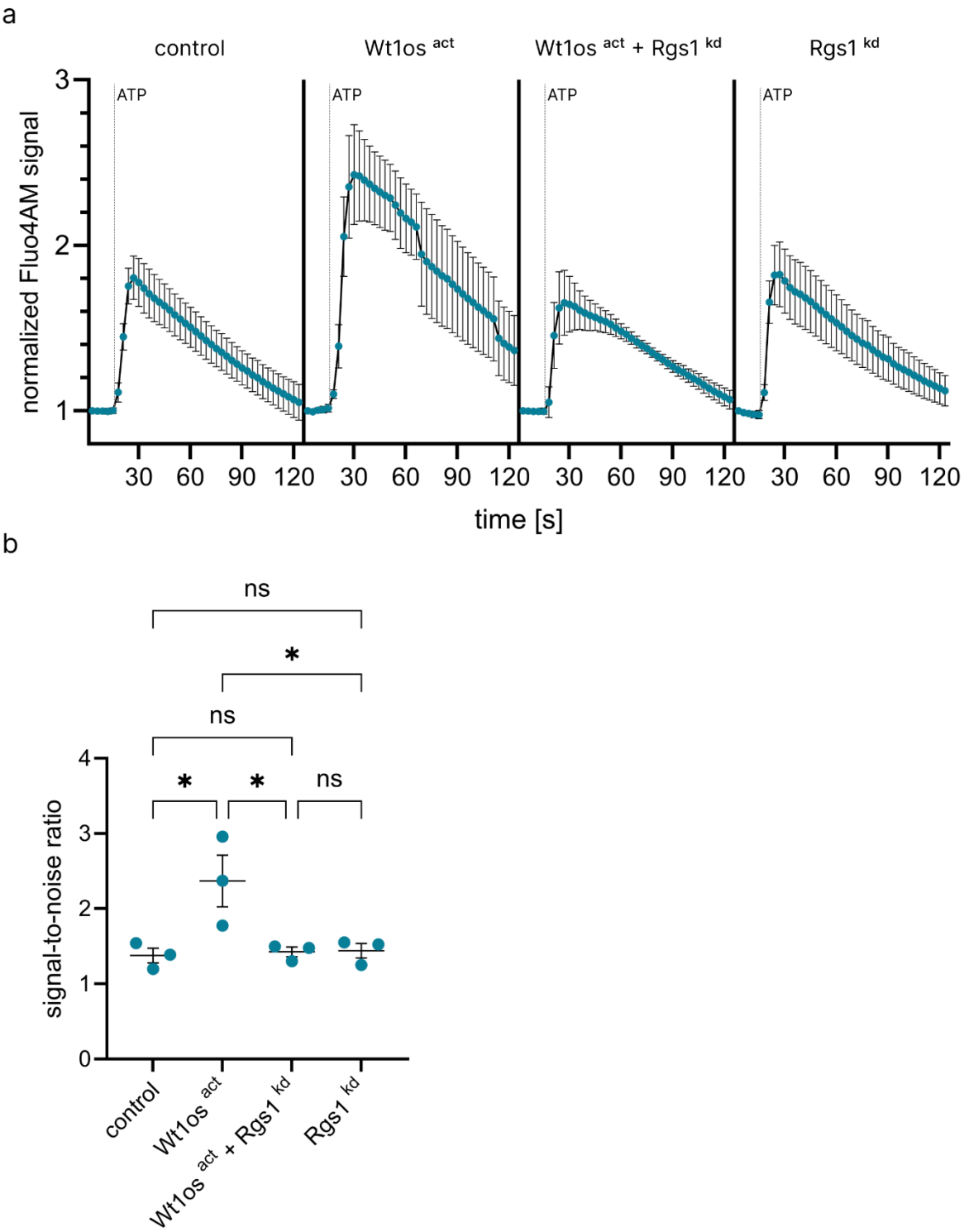

Figure 21. *Wt1os* enhances calcium mobilization in response to ATP in a *Rgs1*-dependent manner.

a. *Wt1os* expression increases ATP-dependent Ca^{2+} store release. Cultured mouse podocytes were loaded with Fluo-4 AM, stimulated with 100 µM ATP, and monitored for changes in green fluorescence indicating cytosolic Ca^{2+} levels.

continued on next page

The graphs display original traces of ATP-induced Ca^{2+} signaling, showing the normalized fluorescence intensity over 120 seconds across tested conditions. The dashed line marks the starting point of ATP stimulation. Each data point represents the mean ±SEM of three biological replicates, with an average 300 cells measured per replicate. **b. Signal quantification of ATP-induced Ca^{2+} signaling.** The average intensity of the five frames before ATP stimulation was set as the baseline fluorescence. The graph displays the ratio between the basal and the maximum (peak) fluorescence measured by Fluo-4 AM imaging. Each data point represents the mean ±SEM of three biological replicates, with an average 300 cells measured per replicate. Tested conditions: control = HSMPS.dCas9.VP64 cells, *Wt1os*^{act} = HSMPS.dCas9.VP64 cells with activation of *Wt1os*, *Wt1os*^{act} + *Rgs1*^{kd} = HSMPS.dCas9.VP64 cells with activation of *Wt1os* and *Rgs1* knockdown, *Rgs1*^{kd} = HSMPS.dCas9.VP64 with *Rgs1* knockdown. One-Way ANOVA was performed to determine statistical significance. (p-value: *≤0.05, ns – not significant).

6. Discussion

In our published study [120], using a novel pipeline *CALINCA* we identified 241 lncRNAs associated with FSGS, including *Wt1os*, which was downregulated in several genetic FSGS mouse models. *Wt1os* is transcribed from a bidirectional promoter shared with *Wt1*, a transcription factor essential for podocyte biology. Notably, *Wt1os* is synthetically conserved with its human orthologue, *WT1-AS*, which has been implicated in cancer biology.

Here, we demonstrate that loss of *Wt1os* in mice leads to podocyte foot process effacement and proteinuria. Transcriptomic analysis of glomeruli from *Wt1os*$^{-/-}$ mice revealed significant gene expression changes. The experiments in cultured mouse podocytes, shown that *Wt1os* localizes to the nucleus and together with *Rgs1* enhances calcium mobilization. In human podocytes, we confirmed the conserved nuclear *WT1-AS* lncRNA localization, shown its crucial role in cell viability and a mutual regulation with *RGS1* gene.

Our findings establish *Wt1os* as a novel regulator of podocyte biology and provide insights into its potential role in FSGS.

6.1. Publication: CALINCA – a novel pipeline for the identification of lncRNAs in podocyte disease

The CALINCA pipeline addresses the unique challenges of studying lncRNAs, which traditional RNAseq analysis tools optimized for coding RNA often overlook. CALINCA automates the analysis of RNAseq data from mouse models of FSGS, enabling the quantification of both annotated and de novo assembled lncRNAs. Beyond expression profiling, CALINCA provides comprehensive insights into the podocyte specificity of identified lncRNAs, their evolutionary conservation, and their expression patterns in human datasets. By integrating these key features, CALINCA serves as a webtool available to the research community for advancing lncRNA research in the context of FSGS.

6.2. Podocyte specific expression of *Wt1os* lncRNA

Mouse *Wt1os* and its human orthologue *WT1-AS* are lncRNAs that share a bidirectional promoter with *Wt1* (or *WT1* in humans), a gene encoding for a transcription factor essential for podocyte biology. Both *Wt1os* and *WT1-AS* are

expressed across various tissues, including the kidneys. Our previous RNAseq experiments identified *Wt1os* in the kidney as a podocyte specific lncRNA[141]. These findings align with the published kidney snRNAseq [142] and scRNAseq [143,144] datasets, which reported the highest expression of *Wt1os* in podocytes. To confirm its podocyte localization, we performed experimental validation by combining *Wt1os* lncRNA staining with immunolabelling of the podocyte marker protein *Wt1* in wild type mouse kidney tissue (

Figure 6). This study represents the first experimental confirmation of the podocyte-specific expression of *Wt1os*.

6.3. Establishing the *Wt1os*$^{-/-}$ mouse line

To analyze the functional role of *Wt1os in vivo,* we aimed to generate a conventional full-body knockout mouse line. Our strategy involved modifying the second exon of the *Wt1os* gene by inserting a strong polyadenylation signal (SPA) derived from the β-globin gene, along with two MAZ elements. MAZ sites are known to activate cleavage and polyadenylation at the polyadenylation site [128]. This was expected to induce early transcription termination from *Wt1os* promoter without disturbing the genomic locus [121,128]. Similar strategies have been successfully used to knock out other lncRNA genes, like *Charme*[121] or MALAT1[145], as well as protein coding genes, like *PPP1R12C* and *NSUN2* [145].

The successful insertion of the SPA into the second exon of *Wt1os* gene was confirmed by PCR (**Figure 7 c**) and Sanger sequencing of the PCR amplicon (**Figure A. 5**). Initial validation of *Wt1os* depletion using qPCR assay targeting exons 1 and 2 shown a strong reduction of the lncRNA expression (**Figure 7 d**) However, the RNA sequencing

conducted later revealed no significant change in the overall *Wt1os* expression levels (**Figure 12**). The discrepancy of those two results arose due to the exon 2 skipping which was targeted by the qPCR assay.

6.3.1. Alternative splicing of *Wt1os* lncRNA

Analysis of the RNAseq data from isolated glomeruli revealed an alternative splicing, specifically exon skipping event (**Figure 12**). The excluded exon was the one carrying the SPA sequence (exon 2), which is a part of three individual *Wt1os* isoforms (*Wt1os*-203, *Wt1os*-204 and *Wt1os*-205). A possible explanation of the exon skipping event is that insertion of the SPA sequence disrupted the exonic splicing regulatory elements within exon 2. This disruption could involve the loss of exonic splicing enhancers or the gain of exonic splicing silencers, either of which could lead to exon 2 being excluded during splicing [146,147]. Since the SPA cassette was introduced in the second half of the exon, the intronic splicing donor and acceptor sites were unaffected [148]. Furthermore, it is plausible that the introduced SPA sequence was recognized as a mutation, triggering a reparative skipping mechanism to bypass the affected exon [149].

The unexpected results can be also explained by the promoter dominance hypothesis [150,151]. Alfonso-Gonzales and colleagues demonstrated, using *Drosophila* brains and human brain organoids, a regulatory link between transcription initiation and 3'end site selection [151]. Their data shown that "dominant promoters" can mediate the skipping of strong poly(A) sites in favor of more distal ones[151]. It is possible that the *Wt1os* promoter favors the native poly(A) site over the synthetic one. This mechanism could potentially explain the observed exon skipping.

6.3.2. *Wt1os* isoform switching in the glomeruli of *Wt1os*$^{-/-}$ mice

Analysis of glomerular RNA sequencing revealed differential transcript usage (DTU) among the *Wt1os* splicing isoforms (**Figure 12**). Specifically, the *Wt1os*-204 isoform was downregulated, while the *Wt1os*-202 isoform was upregulated in the glomeruli of transgenic animals.

The observed isoform switching may be explained by a feedback loop mechanism involving *Wt1os* lncRNA. A significant proportion of lncRNAs function as cis-acting molecules, regulating their own expression or that of neighboring genes through diverse mechanisms [152]. The *Wt1os*-204 isoform could act as a regulatory molecule, either enhancing its own expression or modulating the levels of *Wt1os*-202. Exon 2

skipping may disrupt this feedback loop by altering the function of the *Wt1os*-204 isoform, leading to its downregulation. In turn, the upregulation of *Wt1os*-202 might represent a compensatory mechanism.

The knockout strategy was ineffective in completely abolishing the expression of the *Wt1os* gene. However, exon skipping resulted in a distinct sequence change with functional implications, likely leading to a loss-of-function effect and the observed phenotypic changes in *Wt1os*$^{-/-}$ mice. Function of the regulatory RNAs often depend on their conformation; therefore, the resulting exon skipping was sufficient to disrupt the function of *Wt1os* likely due to structural alterations in the RNA [153]. Additionally, we observe a distinct change in expression pattern, manifested as *Wt1os* lncRNA isoform switching. Further investigation into the molecular functions of each isoform, including their protein interactomes, would provide deeper insight into the regulatory networks underlying these isoform-specific changes.

6.4. *Wt1os*$^{-/-}$ mouse line phenotyping

Although the expression of *Wt1os* was still detectable, phenotypic changes observed in the *Wt1os*$^{-/-}$ mice suggest distinct changes towards lncRNA function. The *Wt1os*$^{-/-}$ mice were viable and genotypes of the offspring from heterozygous crosses followed the expected Mendelian ratios of 1:2:1, indicating no unexpected lethality (**Figure 8 a**). These findings are consistent with previous studies on lncRNA knockout models, which usually do not come with lethality [154]. Homozygous *Wt1os*$^{-/-}$ mice exhibited shortened lifespan with a median survival of 17 months (**Figure 8 c**). The cause of death remains to be elucidated, and it is unclear whether the phenotype arises from dysfunction in a specific organ or from systemic effects. Transcriptomic and histopathological analyses of key organs such as the liver, heart, brain, and kidney of aged animals could provide insight into the physiological consequences of *Wt1os* depletion.

6.4.1. Tissue histology and kidney function

The analysis of kidney function revealed a significantly elevated uACR values indicating increased proteinuria in 30-weeks-old *Wt1os*$^{-/-}$ mice (**Figure 10 b**). Interestingly, the animals did not exhibit changes in plasma urea and creatinine concentrations (**Figure 10 b**), suggesting that despite altered filtration, kidney functions remain stable [10,73]. While plasma urea and creatinine are commonly used as

biomarkers of kidney injury, their limitations in sensitivity and specificity are documented [155]. Both creatinine and urea levels are dependent on nonrenal factors such as age, muscle mass and protein intake [156]. Plasma creatinine increase can be detected when approximately 50% of kidney function is lost [155,156]. In animals with Adriamycin-induced kidney injury, high levels of proteinuria were observed without alterations in blood urea and creatinine levels [157]. These findings support the notion that plasma urea and creatinine are late indicators of glomeruli injury [157] and the observed filtration alterations may not be sufficient to induce changes in plasma parameters.

The ultrastructural analysis of podocytes revealed altered podocyte FP morphology, characterized by significantly reduced SD length and increased FP circularity (**Figure 11**). These parameters are commonly associated with proteinuria and accompany podocyte foot effacement in established mouse models of glomerular diseases [67,71] and patients with FSGS [158]. Our observation of proteinuria in *Wt1os*$^{-/-}$ mice along with the foot process effacement are in line with the glomerular ultrafiltration model. In response to injury, podocytes reorganize their foot processes adopting a more simplified structure with a reduced SD length. As podocytes flatten, their compressing force on the GBM decreases, resulting in increased albumin permeability [11,71]. FP effacement together with the elevated ACRs suggest that the filtration barrier is compromised in *Wt1os*$^{-/-}$ animals. Notably, no evidence of glomerulosclerosis was observed in the analyzed tissue sections from *Wt1os*$^{-/-}$ mice (**Figure 9**). Similarly, in the study from Huber *et al.,* Fyn-/- mice, which develop proteinuria, did not exhibit sclerotic changes in kidney histology [159]. This suggests that the loss of *Wt1os* alone may not induce glomerulosclerosis but could contribute to the disease, potentially acting as a modulator and enhancing susceptibility to glomerular damage under additional stress or injury due to e.g. an administration of a nephrotoxic drug. Our findings suggest that phenotyping changes observed in *Wt1os*$^{-/-}$ mice might portray an early stage of proteinuric kidney disease.

Examination of kidney tissue histology from 30-week-old animals revealed vacuolization in tubular cells throughout the organ (**Figure 9**). The proximal tubule segments are known to reabsorb macromolecules, such as proteins, through endocytosis [160]. The internalized proteins, including albumin, are transported to lysosomes, where they degraded [160,161]. Studies have shown that glomerular

proteinuria can induce gene expression changes along the nephron, leading to tubular injury [161]. Vacuolization is among several hallmarks of tubular cells injury described in many renal diseases and injuries [162]. Wang *et al*. reported a tubular injury induced by urinary proteins in patients with nephrotic syndrome [163]. Further analysis of the nature of tubular vacuoles along with their content is necessary to understand their origin and function in the kidneys of *Wt1os*$^{-/-}$ mice.

6.4.2. Analysis of glomerular transcriptome of *Wt1os*$^{-/-}$ mice

To assess the impact of *Wt1os* loss on the podocyte biology, we performed a differential gene expression (DGE) analysis using the glomerular RNA sequencing data. This analysis identified 16 differentially regulated genes, including 10 downregulated and 6 upregulated genes. The Gene Set Enrichment Analysis (GSEA) revealed associations with pathways related to i.a. spliceosome function, metabolism, and immune pathways (**Figure 14**). These findings suggest that *Wt1os* loss has a modest impact on the glomerular transcriptome. Comparison with publicly available datasets revealed consistent regulation patterns for *RGS1, PILRA, TMEM132C, LIPG, ANGPTL4* and *SOCS2* in kidney biopsy samples from patients with CKD, minimal change disease or FSGS [164,165]. In contrast, *RAB3C, CENPF* and *KCND1* demonstrated an opposite direction of regulation in CKD patients [164,165].

As lncRNAs mainly act as gene expression modulators and some appear to be dispensable, their knockout is generally not expected to have a strong impact on the overall transcriptome [166]. The limited changes observed may be attributed to the ineffective *Wt1os* knockout. The remaining *Wt1os* levels, even lacking exon 2, could retain partial functionality. Additionally, it is also possible that *Wt1os* works in a context-dependent manner and its loss leads to subtle effects. A study involving a complete and efficient *Wt1os* knockout is necessary to elucidate the full its role in the glomerulus and podocyte biology.

6.5. Characterization of *Wt1os* and *WT1-AS* lncRNAs in cultured podocytes

To investigate the function of *Wt1os in vitro*, we employed two cultured podocyte cell lines: mouse (HSMPS – Heat Sensitive Mouse Podocytes) and human (AB8) podocytes. RNA sequencing revealed distinct differences in the lncRNA expression

between these models. While the AB8 cell line expressed the human lncRNA *WT1-AS* at a decent level, the mouse HSMPS cell line exhibited minimal *Wt1os* expression (**Table 30**). Podocytes i*n vivo* are terminally differentiated cells arrested in the G_0 phase of the cell cycle [4,9]. Their unique morphology and specialized functions depend on their interaction with the glomerular basement membrane and neighboring cells [4]. The immortalization process and suboptimal culturing conditions can alter their expression pattern, potentially leading to downregulation of podocyte specific genes [167].

6.5.1. The effect of *WT1-AS* knockdown on cells viability

We first focused on the AB8 cell line for subsequent experiments. Subcellular localization analysis confirmed that *WT1-AS* is predominantly nuclear, consistent with previous studies showing nuclear localization of *WT1-AS* through cell fractionation experiments (**Figure 15**) [168]. To assess the functional role of *WT1-AS*, we employed GapmeR-mediated knockdown in human podocytes. Live cell imaging revealed a significant increase in cell death following the *WT1-AS* knockdown (**Figure 16**). Interestingly, our findings contrast with those reported by Zhang *et al*., who observed opposite effects of *WT1-AS* knockdown in gastric cancer stem cells [168]. In their study, *WT1-AS* overexpression suppressed cell proliferation and induced apoptosis, while knockdown enhanced cell viability [168]. Similarly, Lv *et al.,* reported that *WT1-AS* suppressed proliferation and promoted apoptosis in hepatocellular carcinoma (HCC) cell lines [169]. Both studies implicated *WT1-AS* in the regulation of *WT1*, demonstrating that *WT1-AS* downregulated its expression [168,169]. Our data show no effect on Wt1 expression in *Wt1os*$^{-/-}$ mice (**Figure 13**). *WT1* is a multifaceted gene with diverse biological roles. While it is recognized as a tumor suppressor in Wilms' tumor (nephroblastoma) [170], *WT1* was also reported to play an oncogenic role in various cancers, including leukemia, breast cancer, ovarian cancer and glioblastoma [171,172]. These findings underscore a potential tissue and context specific modes of actions of both *WT1* and *WT1-AS*. The contrasting roles observed in our study and previous cancer-focused research highlight the importance of cellular context in determining the functional effects of *Wt1os* and *WT1-AS*.

6.5.2. The effect of *WT1-AS* knockdown on gene expression

To investigate the effect of *WT1-AS* loss in human cultured podocytes, we performed qPCR analysis following its knockdown, focusing on genes previously identified as differentially regulated in the glomeruli of *Wt1os*$^{-/-}$ mice (

Figure 16). Among these, *RGS1* was significantly downregulated, consistent with the mouse RNA sequencing data, where *Rgs1* also shown reduced expression (**Figure 14**). Since the expression levels of other tested genes remained unchanged, this finding suggests a potential regulatory relationship between *WT1-AS* and *RGS1*, indicating that *RGS1* expression may depend on the presence of *WT1-AS*. Interestingly we found out that upregulation of *RGS1* led to upregulation of *WT1-AS* **(Figure 17)**. Our data indicate a positive feedback regulatory mechanism between *WT1-AS* and *RGS1*. Feedback loops are a common control mechanism in gene circuits' regulation [173]. LncRNAs are known to participate in regulatory feedback loops, for example, *CHD2* regulates its own expression via the lncRNA *Chaserr*, which serves as an indicator of *CHD2* levels [83]. Given that mouse *Rgs1* and human *RGS1* are located on the chromosome 1, while mouse *Wt1os* and human *WT1-AS* are located on the chromosome 2 and 11, respectively, we can exclude the possibility of co-activation due to CRISPRa-mediated gene activation. This supports the argument of a functional link between *Rgs1* and *Wt1os*. Further investigation is needed to elucidate the nature of this bidirectional regulation, particularly in the context of podocyte survival.

6.5.3. CRISPRa-mediated *Wt1os* expression in cultured mouse podocytes

Several strategies are available to enhance the expression of an lncRNA gene in the cultured cell models, including plasmid-based overexpression [174] or stable gene integration via lentiviral vectors and transposons [175]. However, standard overexpression methods commonly used for protein-coding genes have been shown to be inefficient for lncRNA studies [175,176]. Ectopic expression may mislocalize the lncRNA products away from their physiological subcellular compartments [177] or lead to the production of the lncRNA in the improper length [175]. To overcome these limitations, we employed the CRISPRa system, which allowed us to use the endogenous promoter of *Wt1os*, ensuring expression levels and isoform distribution closer to physiological

conditions [178]. Importantly, using the native promoter helped preserve the common regulation of both *Wt1os* and *Wt1* and its potential physiological implications.

Through lentiviral transduction, we successfully integrated dCas9 fused to the VP64 transcriptional activator domain (**Figure A. 6**). To define the subcellular localization of *Wt1os*, we performed RNA in situ hybridization, revealing that, consistently with data from the cultured human podocytes, *Wt1os* is a primarily localized in the nucleus (**Figure 18**). This finding suggests a conserved molecular function between *Wt1os* and its human orthologue, *WT1-AS*.

6.5.4. The effect of *Wt1os* expression in HSMPS cells on gene expression

To investigate the effect of *Wt1os* expression in mouse cultured podocytes, we performed qPCR analysis following its activation, focusing on genes previously identified as differentially regulated in the glomeruli of *Wt1os*$^{-/-}$ mice. The analysis revealed a significant upregulation of six genes: *Lipg*, *Kcnd1*, *Gbp6* (a gene overlapping with *Gm43302*), *Socs2*, *Angptl4* and *Rgs1* (**Figure 20**). Given that *Wt1os* loss of function in *Wt1os*$^{-/-}$ mice led to differential gene regulation in the glomeruli, we aimed to identify genes displaying an opposite pattern of regulation following *Wt1os* activation in cultured podocytes. Notably, this was observed for *Rgs1, Kcnd1, Socs2* and *Gbp6*, suggesting a potential regulatory relationship between *Wt1os* and these genes. Among them, *Rgs1* was of particular interest, as it was consistently differentially regulated in the glomeruli of *Wt1os*$^{-/-}$ mice, and also downregulated in the human podocytes after *WT1-AS* knockdown (**Figure 14** and

Figure 16) pointing towards a conserved regulatory architecture. Of note, we confirmed that *Rgs1* expression was independent from *Wt1* (**Figure 19 c**). These findings suggest that *Rgs1* expression may be dependent on the presence of *Wt1os*, further supporting the potential functional link between the two genes.

6.5.5. The effect of *Wt1os* on podocytes migration

Rgs1 (Regulator of G-protein signaling 1) acts as a GTPase-activating protein (GAP) attenuating the G-protein-coupled receptor (GPCR) signaling[179]. Given its role in cell migration [136] and the fact that podocyte migration is a key characteristic [180] associated with stress response mechanisms [181], we first focused on this cellular phenotype. To investigate the impact of *Wt1os* expression on podocyte migration, we performed a wound-healing assay following *Wt1os* activation, both alone and in combination with

Rgs1 knockdown. Our results indicate that *Wt1os* activation enhances the migratory phenotype of mouse podocytes (**Figure 20**). Notably, this effect appears to be independent of *Rgs1* expression, suggesting that *Wt1os* may influence podocyte migration through alternative pathways.

6.5.6. The role of *Wt1os* expression on calcium signaling

Calcium signaling has been identified as a downstream effector of Rgs1 [137,182]. In podocytes, calcium acts as an important second messenger [183], contributing to foot process morphogenesis, structural maintenance, and cell survival [184]. Notably, both gain- and loss-of-function mutations in *TRPC6,* which encodes for Ca^{2+} channels, have been linked to FSGS [184]. Given these findings, we specifically investigated calcium dynamics in our study. We monitored calcium levels in cultured mouse podocytes following ATP stimulation and observed that cells with *Wt1os* activation responded stronger to the ATP treatment compared to control condition. Our results suggest that *Wt1os* regulates calcium signaling in a *Rgs1*-dependent manner (**Figure 21**). Interestingly, the increase in calcium mobilization observed with elevated *Rgs1* expression was unexpected, given that Rgs1 functions as a negative regulator of GPCR signaling, typically terminating downstream responses. However, this observation aligns with prior findings in macrophages, where *Rgs1* overexpression was shown to enhance calcium signaling by increasing phosphorylation of PLC (phosphoinositide-specific phospholipase C) and the IP3 (inositol-1,4,5-triphosphate) receptor [138], promoting calcium release from ER stores [185]. Further support for *Wt1os* role in calcium signaling comes from our transcriptomics analysis of glomeruli from *Wt1os*$^{-/-}$ mice (**Figure 14**). Among the differentially expressed genes, several were associated with calcium signaling: *Erdr* (upregulated in *Wt1os*$^{-/-}$ mice), *Sosc2* and *Cenpf* (both downregulated in *Wt1os*$^{-/-}$ mice). *Erdr1* has been reported to enhance calcium influx in thymocytes [186], while loss of *Socs2* or *Cenpf* has been associated with reduced calcium dynamics in cardiomyocytes [187,188]. These findings suggest a potential *Rgs1*-dependent role of *Wt1os* in regulating calcium signaling in podocytes.

6.6. Study limitations and outlook

While our findings provide insights into the role of *Wt1os* in podocyte biology, several limitations must be considered. First, our *Wt1os*$^{-/-}$ mice used in this study did not have a complete *Wt1os* knockout, which may allow us to observe the full impact of *Wt1os*

loss. The transcriptomic analysis was limited to bulk glomerular tissue, which includes multiple cell types, potentially diluting podocyte-specific effects. Future studies employing single-cell RNA sequencing could help refine our understanding of the precise role of *Wt1os* in podocytes. The mouse podocyte model we used may not fully recapitulate the physiological regulation of *Wt1os* and *Rgs1*, as *Wt1os* was not expressed at baseline, necessitating artificial expression activation. This could lead to non-physiological interactions. Additionally, our study did not directly assess downstream functional consequences, such as podocyte morphology or adhesion, which could further clarify the biological significance of these changes. Further analyses are necessary to elucidate the nature of the link between *Wt1os* and *Rgs1*, as well as the functional consequences of their mutual regulation. One approach to address this would be to assess calcium signaling activation by measuring the phosphorylation levels of downstream effectors in the calcium signaling pathway, both in isolated glomeruli form *Wt1os*$^{-/-}$ mice and in cultured podocytes following ATP stimulation. To understand the functional impact of *Wt1os*-mediated calcium regulation on podocyte biology, additional experiments should focus on cytoskeleton organization and adhesion dynamics. In-depth proteomics analysis of human cultured podocytes following *WT1-AS* knockdown could help identify pathways disrupted upon lncRNA loss. Additionally, a rescue experiment in human cultured podocytes, involving simultaneous *WT1-AS* knockdown and *Rgs1* upregulation, could determine whether the cell death phenotype is *Rgs1*-dependent. Furthermore, to investigate dynamic calcium signaling in podocytes *in vivo*, *Wt1os*$^{-/-}$ mice could be crossed with mice expressing a podocyte specific calcium reporter. This model would allow live imaging of podocytes in the intact kidney, enabling real-time tracking of calcium flux in response to ATP or Angiotensin II. Identifying further cellular phenotypes regulated by *Wt1os* in the *Rgs1*-dependent manner is crucial to fully characterize its function in podocytes, potentially revealing novel therapeutic targets for podocyte-related kidney diseases.

7. Conclusion

Wt1os is a lncRNA syntenically conserved between mouse and human. Both *Wt1os* and its human orthologue, *WT1-AS*, belong to the class of divergent lncRNAs, which are bidirectionally transcribed from the same promoter as *Wt1*, a key podocyte transcription factor involved in podocyte biology and kidney development[123,190]. While no studies have explored the function of *Wt1os*, its human counterpart, *WT1-AS*, has been implicated in cancer, where it regulates tumor growth, metastasis, and invasion. However, the role of both mouse *Wt1os* and human *WT1-AS* in kidney function, FSGS, and podocyte biology remains unknown.

In our previous study, we identified *Wt1os* as one of 241 differentially regulated lncRNAs in FSGS mouse models, where it was significantly downregulated. Here, we provide experimental evidence demonstrating its podocyte-specific expression in mouse glomeruli. Using a novel *Wt1os*$^{-/-}$ mouse line, we shown that loss of *Wt1os* results in podocyte foot process effacement and proteinuria. Furthermore, our transcriptomic analysis of glomeruli from *Wt1os*$^{-/-}$ mice revealed significant gene expression changes. In cultured mouse podocytes, we found that *Wt1os* is predominantly localized to the nucleus, exerts a promigratory effect and regulates calcium signaling in a *Rgs1*-dependent manner. Consistently, in human podocyte, we confirmed its conserved nuclear localization. Additionally, through GapmeRs-mediated knockdown, we demonstrated its role in cell viability and its impact on gene expression, showing its mutual regulation with *RGS1*.

Further studies are needed to clarify the relationship between *Wt1os* and *Rgs1* and to determine the functional impact of their mutual regulation. Defining the cellular

phenotypes controlled by *Wt1os* in a *Rgs1*-dependent manner is essential for fully understanding its role in podocytes and FSGS pathogenesis.

8. References

1. Radi, Z. A. Kidney Pathophysiology, Toxicology, and Drug-Induced Injury in Drug Development. *Int J Toxicol* **38**, 215–227 (2019).
2. Alan S. L. Yu *et al. BRENNER & RECTOR'S THE KIDNEY*. (Elsevier, 2020).
3. Schnell, J., Achieng, M. & Lindström, N. O. Principles of human and mouse nephron development. *Nat Rev Nephrol* **18**, 628–642 (2022).
4. Kopp, J. B. *et al.* Podocytopathies. *Nat Rev Dis Primers* **6**, 68 (2020).
5. Purbhoo, K. Physiology of the distal convoluted tubule and collecting duct. *Southern African Journal of Anaesthesia and Analgesia* S137–S141 (2020) doi:10.36303/SAJAA.2020.26.6.S3.2559.
6. Shi, J. *et al.* Quantifying Podocyte Number in a Small Sample Size of Glomeruli with CUBIC to Evaluate Podocyte Depletion of db/db Mice. *J Diabetes Res* **2023**, 1–12 (2023).
7. Puelles, V. G. *et al.* Validation of a Three-Dimensional Method for Counting and Sizing Podocytes in Whole Glomeruli. *Journal of the American Society of Nephrology* **27**, 3093–3104 (2016).
8. Meliambro, K., He, J. C. & Campbell, K. N. Podocyte-targeted therapies — progress and future directions. *Nat Rev Nephrol* (2024) doi:10.1038/s41581-024-00843-z.

9. Meyrier, A. Mechanisms of Disease: focal segmental glomerulosclerosis. *Nat Clin Pract Nephrol* **1**, 44–54 (2005).

10. Butt, L. *et al.* A molecular mechanism explaining albuminuria in kidney disease. *Nat Metab* **2**, 461–474 (2020).

11. Benzing, T. & Salant, D. Insights into Glomerular Filtration and Albuminuria. *New England Journal of Medicine* **384**, 1437–1446 (2021).

12. Fissell, W. H. Reconsidering Garth Robinson. *Curr Opin Nephrol Hypertens* **29**, 273–279 (2020).

13. Barutta, F., Bellini, S. & Gruden, G. Mechanisms of podocyte injury and implications for diabetic nephropathy. *Clin Sci* **136**, 493–520 (2022).

14. Huber, T. B. & Benzing, T. The slit diaphragm: a signaling platform to regulate podocyte function. *Curr Opin Nephrol Hypertens* **14**, 211–216 (2005).

15. Kocylowski, M. K. *et al.* A slit-diaphragm-associated protein network for dynamic control of renal filtration. *Nat Commun* **13**, 6446 (2022).

16. Nakatsue, T. *et al.* Nephrin and podocin dissociate at the onset of proteinuria in experimental membranous nephropathy. *Kidney Int* **67**, 2239–2253 (2005).

17. Grahammer, F. *et al.* A flexible, multilayered protein scaffold maintains the slit in between glomerular podocytes. *JCI Insight* **1**, (2016).

18. REISER, J., KRIZ, W., KRETZLER, M. & MUNDEL, P. The Glomerular Slit Diaphragm Is a Modified Adherens Junction. *Journal of the American Society of Nephrology* **11**, 1–8 (2000).

19. Inoue, T. *et al.* FAT is a component of glomerular slit diaphragms. *Kidney Int* **59**, 1003–1012 (2001).

20. Fukusumi, Y. *et al.* Nephrin-Binding Ephrin-B1 at the Slit Diaphragm Controls Podocyte Function through the JNK Pathway. *Journal of the American Society of Nephrology* **29**, 1462–1474 (2018).

21. Sagar, A. *et al.* Targeting Neph1 and ZO-1 protein-protein interaction in podocytes prevents podocyte injury and preserves glomerular filtration function. *Sci Rep* **7**, 12047 (2017).

22. Tossidou, I. *et al.* Tyrosine Phosphorylation of CD2AP Affects Stability of the Slit Diaphragm Complex. *Journal of the American Society of Nephrology* **30**, 1220–1237 (2019).

23. Patrie, K. M., Drescher, A. J., Welihinda, A., Mundel, P. & Margolis, B. Interaction of Two Actin-binding Proteins, Synaptopodin and α-Actinin-4, with the Tight Junction Protein MAGI-1. *Journal of Biological Chemistry* **277**, 30183–30190 (2002).

24. Takamura, S., Fukusumi, Y., Zhang, Y., Narita, I. & Kawachi, H. Partitioning-Defective-6–Ephrin-B1 Interaction Is Regulated by Nephrin-Mediated Signal and Is Crucial in Maintaining Slit Diaphragm of Podocyte. *Am J Pathol* **190**, 333–346 (2020).

25. Kawachi, H. & Fukusumi, Y. New insight into podocyte slit diaphragm, a therapeutic target of proteinuria. *Clin Exp Nephrol* **24**, 193–204 (2020).

26. Yin, L., Yu, L., He, J. C. & Chen, A. Controversies in Podocyte Loss: Death or Detachment? *Front Cell Dev Biol* **9**, (2021).

27. Huber, T. B. & Benzing, T. The slit diaphragm: a signaling platform to regulate podocyte function. *Curr Opin Nephrol Hypertens* **14**, 211–216 (2005).

28. Li, H., Lemay, S., Aoudjit, L., Kawachi, H. & Takano, T. Src-Family Kinase Fyn Phosphorylates the Cytoplasmic Domain of Nephrin and Modulates Its Interaction with Podocin. *Journal of the American Society of Nephrology* **15**, 3006–3015 (2004).

29. Huber, T. B. *et al.* Nephrin and CD2AP Associate with Phosphoinositide 3-OH Kinase and Stimulate AKT-Dependent Signaling. *Mol Cell Biol* **23**, 4917–4928 (2003).

30. Lorenzo, H. K. & Ollero, M. Editorial: Molecular and Cellular Biology of podocytes. *Front Cell Dev Biol* **10**, (2022).

31. Schell, C. & Huber, T. B. The Evolving Complexity of the Podocyte Cytoskeleton. *Journal of the American Society of Nephrology* **28**, 3166–3174 (2017).

32. Tian, X. & Ishibe, S. Targeting the podocyte cytoskeleton: from pathogenesis to therapy in proteinuric kidney disease. *Nephrology Dialysis Transplantation* **31**, 1577–1583 (2016).

33. Haley, K. E. *et al.* Podocyte injury elicits loss and recovery of cellular forces. *Sci Adv* **4**, (2018).

34. Windpessl, M. *et al.* Glomerular Diseases Across Lifespan: Key Differences in Diagnostic and Therapeutic Approaches. *Semin Nephrol* **43**, 151435 (2023).

35. Mejia-Vilet, J. M. & Parikh, S. V. Overview of the Current Approach to Glomerular Disease Classification. in *Glomerulonephritis* 59–85 (Springer International Publishing, Cham, 2019). doi:10.1007/978-3-319-49379-4_5.

36. Korbet, S., Whittier, W. & Gashti, C. Focal Segmental Glomerulosclerosis, Adult. in *Glomerulonephritis* 1–29 (Springer International Publishing, Cham, 2017). doi:10.1007/978-3-319-27334-1_9-1.

37. De Vriese, A. S., Wetzels, J. F., Glassock, R. J., Sethi, S. & Fervenza, F. C. Therapeutic trials in adult FSGS: lessons learned and the road forward. *Nat Rev Nephrol* **17**, 619–630 (2021).

38. Fogo, A. B. Causes and pathogenesis of focal segmental glomerulosclerosis. *Nat Rev Nephrol* **11**, 76–87 (2015).

39. De Vriese, A. S., Sethi, S., Nath, K. A., Glassock, R. J. & Fervenza, F. C. Differentiating Primary, Genetic, and Secondary FSGS in Adults: A Clinicopathologic Approach. *Journal of the American Society of Nephrology* **29**, 759–774 (2018).

40. Wharram, B. L. *et al.* Podocyte Depletion Causes Glomerulosclerosis. *Journal of the American Society of Nephrology* **16**, 2941–2952 (2005).

41. Jacobs-Cachá, C. *et al.* Challenges in primary focal segmental glomerulosclerosis diagnosis: from the diagnostic algorithm to novel biomarkers. *Clin Kidney J* **14**, 482–491 (2021).

42. Shankland, S. J., Rule, A. D., Kutz, J. N., Pippin, J. W. & Wessely, O. Podocyte Senescence and Aging. *Kidney360* **4**, 1784–1793 (2023).

43. Lazzeri, E. & Romagnani, P. Differentiation of parietal epithelial cells into podocytes. *Nat Rev Nephrol* **11**, 7–8 (2015).

44. Vogelmann, S. U., Nelson, W. J., Myers, B. D. & Lemley, K. V. Urinary excretion of viable podocytes in health and renal disease. *American Journal of Physiology-Renal Physiology* **285**, F40–F48 (2003).

45. Rood, I. M., Deegens, J. K. J. & Wetzels, J. F. M. Genetic causes of focal segmental glomerulosclerosis: implications for clinical practice. *Nephrology Dialysis Transplantation* **27**, 882–890 (2012).

46. Woroniecki, R. P. & Kopp, J. B. Genetics of focal segmental glomerulosclerosis. *Pediatric Nephrology* **22**, 638–644 (2007).

47. Lipska, B. S. *et al.* Genotype–phenotype associations in WT1 glomerulopathy. *Kidney Int* **85**, 1169–1178 (2014).

48. Ettou, S. *et al.* Epigenetic transcriptional reprogramming by WT1 mediates a repair response during podocyte injury. *Sci Adv* **6**, (2020).

49. Dong, L., Pietsch, S. & Englert, C. Towards an understanding of kidney diseases associated with WT1 mutations. *Kidney Int* **88**, 684–690 (2015).

50. Wiggins, R.-C. The spectrum of podocytopathies: A unifying view of glomerular diseases. *Kidney Int* **71**, 1205–1214 (2007).

51. Puelles, V. G. *et al.* Human podocyte depletion in association with older age and hypertension. *American Journal of Physiology-Renal Physiology* **310**, F656–F668 (2016).

52. Sharma, M. *et al.* Glomerular Biomechanical Stress and Lipid Mediators during Cellular Changes Leading to Chronic Kidney Disease. *Biomedicines* **10**, 407 (2022).

53. Dupont, S. *et al.* Role of YAP/TAZ in mechanotransduction. *Nature* **474**, 179–183 (2011).

54. Salfi, G., Casiraghi, F. & Remuzzi, G. Current understanding of the molecular mechanisms of circulating permeability factor in focal segmental glomerulosclerosis. *Front Immunol* **14**, (2023).

55. Araya, C. E. *et al.* A case of unfulfilled expectations. Cytokines in idiopathic minimal lesion nephrotic syndrome. *Pediatric Nephrology* **21**, 603–610 (2006).

56. Kemper, M. J., Zepf, K., Klaassen, I., Link, A. & Müller-Wiefel, D. E. Changes of Lymphocyte Populations in Pediatric Steroid-Sensitive Nephrotic Syndrome Are More Pronounced in Remission than in Relapse. *Am J Nephrol* **25**, 132–137 (2005).

57. Youssef, D. M., El-Shal, A. S., Hussein, S., Salah, K. & Ahmed, A. E. R. E. Tumor necrosis factor alpha gene polymorphisms and haplotypes in Egyptian children with nephrotic syndrome. *Cytokine* **102**, 76–82 (2018).

58. Raveh, D., Shemesh, O., Ashkenazi, Y. J., Winkler, R. & Barak, V. Tumor necrosis factor-? blocking agent as a treatment for nephrotic syndrome. *Pediatric Nephrology* **19**, 1281–1284 (2004).

59. Leroy, S. *et al.* Successful Anti-TNFα Treatment in a Child with Posttransplant Recurrent Focal Segmental Glomerulosclerosis. *American Journal of Transplantation* **9**, 858–861 (2009).

60. Hahm, E. *et al.* Bone marrow-derived immature myeloid cells are a main source of circulating suPAR contributing to proteinuric kidney disease. *Nat Med* **23**, 100–106 (2017).

61. Wei, C. *et al.* Circulating urokinase receptor as a cause of focal segmental glomerulosclerosis. *Nat Med* **17**, 952–960 (2011).

62. Deegens, J. K. J., Andresdottir, M. B., Croockewit, S. & Wetzels, J. F. M. Plasma exchange improves graft survival in patients with recurrent focal glomerulosclerosis after renal transplantation. *Transplant International* **17**, 151–157 (2004).

63. Shirai, Y. *et al.* A multi-institutional study found a possible role of anti-nephrin antibodies in post-transplant focal segmental glomerulosclerosis recurrence. *Kidney Int* **105**, 608–617 (2024).

64. Watts, A. J. B. *et al.* Discovery of Autoantibodies Targeting Nephrin in Minimal Change Disease Supports a Novel Autoimmune Etiology. *Journal of the American Society of Nephrology* **33**, 238–252 (2022).

65. Hengel, F. E. *et al.* Autoantibodies Targeting Nephrin in Podocytopathies. *New England Journal of Medicine* **391**, 422–433 (2024).

66. Unnersjö-Jess, D., Scott, L., Blom, H. & Brismar, H. Super-resolution stimulated emission depletion imaging of slit diaphragm proteins in optically cleared kidney tissue. *Kidney Int* **89**, 243–247 (2016).

67. Unnersjö-Jess, D. *et al.* Deep learning–based segmentation and quantification of podocyte foot process morphology suggests differential patterns of foot process effacement across kidney pathologies. *Kidney Int* **103**, 1120–1130 (2023).

68. Kawashima, N., Naito, S., Nagane, M., Yamashita, T. & Nakayama, K. Progression of albuminuria and podocyte injury in focal segmental glomerulosclerosis inhibited by enhanced glycosphingolipid GM3 via valproic acid. *Sci Rep* **13**, 22487 (2023).

69. de Mik, S. M., Hoogduijn, M. J., de Bruin, R. W. & Dor, F. J. Pathophysiology and treatment of focal segmental glomerulosclerosis: the role of animal models. *BMC Nephrol* **14**, 74 (2013).

70. Mollet, G. *et al.* Podocin Inactivation in Mature Kidneys Causes Focal Segmental Glomerulosclerosis and Nephrotic Syndrome. *Journal of the American Society of Nephrology* **20**, 2181–2189 (2009).

71. Butt, L. *et al.* A molecular mechanism explaining albuminuria in kidney disease. *Nat Metab* **2**, 461–474 (2020).

72. Ozdemir, D. D. & Hohenstein, P. Wt1 in the kidney—a tale in mouse models. *Pediatric Nephrology* **29**, 687–693 (2014).

73. Menke, A. L. *et al.* The *wt1* -heterozygous mouse; a model to study the development of glomerular sclerosis. *J Pathol* **200**, 667–674 (2003).

74. Yang, J. W. *et al.* Recent advances of animal model of focal segmental glomerulosclerosis. *Clin Exp Nephrol* **22**, 752–763 (2018).

75. LEE, V. W. & HARRIS, D. C. Adriamycin nephropathy: A model of focal segmental glomerulosclerosis. *Nephrology* **16**, 30–38 (2011).

76. Rider, S. A., Bruton, F. A., Collins, R. G., Conway, B. R. & Mullins, J. J. The Efficacy of Puromycin and Adriamycin for Induction of Glomerular Failure in Larval Zebrafish Validated by an Assay of Glomerular Permeability Dynamics. *Zebrafish* **15**, 234–242 (2018).

77. Nojima, T. & Proudfoot, N. J. Mechanisms of lncRNA biogenesis as revealed by nascent transcriptomics. *Nat Rev Mol Cell Biol* **23**, 389–406 (2022).

78. Dahariya, S. *et al.* Long non-coding RNA: Classification, biogenesis and functions in blood cells. *Mol Immunol* **112**, 82–92 (2019).

79. Mattick, J. S. *et al.* Long non-coding RNAs: definitions, functions, challenges and recommendations. *Nat Rev Mol Cell Biol* **24**, 430–447 (2023).

80. Okazaki, Y. *et al.* Analysis of the mouse transcriptome based on functional annotation of 60,770 full-length cDNAs. *Nature* **420**, 563–573 (2002).

81. Jarroux, J., Morillon, A. & Pinskaya, M. History, Discovery, and Classification of lncRNAs. in 1–46 (2017). doi:10.1007/978-981-10-5203-3_1.

82. Volders, P.-J. *et al.* LNCipedia 5: towards a reference set of human long non-coding RNAs. *Nucleic Acids Res* **47**, D135–D139 (2019).

83. Statello, L., Guo, C.-J., Chen, L.-L. & Huarte, M. Gene regulation by long non-coding RNAs and its biological functions. *Nat Rev Mol Cell Biol* **22**, 96–118 (2021).

84. Quinn, J. J. & Chang, H. Y. Unique features of long non-coding RNA biogenesis and function. *Nat Rev Genet* **17**, 47–62 (2016).

85. Lorenzi, L. *et al.* The RNA Atlas expands the catalog of human non-coding RNAs. *Nat Biotechnol* **39**, 1453–1465 (2021).

86. Lepoivre, C. *et al.* Divergent transcription is associated with promoters of transcriptional regulators. *BMC Genomics* **14**, 914 (2013).

87. Clark, M. B. *et al.* Genome-wide analysis of long noncoding RNA stability. *Genome Res* **22**, 885–898 (2012).

88. Tani, H. *et al.* Genome-wide determination of RNA stability reveals hundreds of short-lived noncoding transcripts in mammals. *Genome Res* **22**, 947–956 (2012).

89. Bridges, M. C., Daulagala, A. C. & Kourtidis, A. LNCcation: lncRNA localization and function. *Journal of Cell Biology* **220**, (2021).

90. Agrawal, S. *et al.* Annotation of nuclear lncRNAs based on chromatin interactions. *PLoS One* **19**, e0295971 (2024).

91. Yip, C. W. *et al.* Antisense-oligonucleotide-mediated perturbation of long non-coding RNA reveals functional features in stem cells and across cell types. *Cell Rep* **41**, 111893 (2022).

92. Yao, R.-W., Wang, Y. & Chen, L.-L. Cellular functions of long noncoding RNAs. *Nat Cell Biol* **21**, 542–551 (2019).

93. Guh, C.-Y., Hsieh, Y.-H. & Chu, H.-P. Functions and properties of nuclear lncRNAs—from systematically mapping the interactomes of lncRNAs. *J Biomed Sci* **27**, 44 (2020).

94. Minajigi, A. *et al.* A comprehensive Xist interactome reveals cohesin repulsion and an RNA-directed chromosome conformation. *Science (1979)* **349**, (2015).

95. Xiang, J.-F. *et al.* Human colorectal cancer-specific CCAT1-L lncRNA regulates long-range chromatin interactions at the MYC locus. *Cell Res* **24**, 513–531 (2014).

96. Hacisuleyman, E. *et al.* Topological organization of multichromosomal regions by the long intergenic noncoding RNA Firre. *Nat Struct Mol Biol* **21**, 198–206 (2014).

97. Arab, K. *et al.* GADD45A binds R-loops and recruits TET1 to CpG island promoters. *Nat Genet* **51**, 217–223 (2019).

98. He, R.-Z., Luo, D.-X. & Mo, Y.-Y. Emerging roles of lncRNAs in the post-transcriptional regulation in cancer. *Genes Dis* **6**, 6–15 (2019).

99. Zhang, B. *et al.* The lncRNA Malat1 Is Dispensable for Mouse Development but Its Transcription Plays a cis-Regulatory Role in the Adult. *Cell Rep* **2**, 111–123 (2012).

100. Tripathi, V. *et al.* Long Noncoding RNA MALAT1 Controls Cell Cycle Progression by Regulating the Expression of Oncogenic Transcription Factor B-MYB. *PLoS Genet* **9**, e1003368 (2013).

101. Tripathi, V. *et al.* The Nuclear-Retained Noncoding RNA MALAT1 Regulates Alternative Splicing by Modulating SR Splicing Factor Phosphorylation. *Mol Cell* **39**, 925–938 (2010).

102. Zeng, C., Fukunaga, T. & Hamada, M. Identification and analysis of ribosome-associated lncRNAs using ribosome profiling data. *BMC Genomics* **19**, 414 (2018).

103. Carlevaro-Fita, J., Rahim, A., Guigó, R., Vardy, L. A. & Johnson, R. Cytoplasmic long noncoding RNAs are frequently bound to and degraded at ribosomes in human cells. *RNA* **22**, 867–882 (2016).

104. Noh, J. H. *et al.* HuR and GRSF1 modulate the nuclear export and mitochondrial localization of the lncRNA *RMRP*. *Genes Dev* **30**, 1224–1239 (2016).

105. Lin, A. *et al.* The LINK-A lncRNA interacts with PtdIns(3,4,5)P3 to hyperactivate AKT and confer resistance to AKT inhibitors. *Nat Cell Biol* **19**, 238–251 (2017).

106. Gezer, U., Özgür, E., Cetinkaya, M., Isin, M. & Dalay, N. Long non-coding RNAs with low expression levels in cells are enriched in secreted exosomes. *Cell Biol Int* **38**, 1076–1079 (2014).

107. Yoon, J.-H. *et al.* LincRNA-p21 Suppresses Target mRNA Translation. *Mol Cell* **47**, 648–655 (2012).

108. Liu, B. *et al.* A Cytoplasmic NF-κB Interacting Long Noncoding RNA Blocks IκB Phosphorylation and Suppresses Breast Cancer Metastasis. *Cancer Cell* **27**, 370–381 (2015).

109. Wang, J. *et al.* CREB up-regulates long non-coding RNA, HULC expression through interaction with microRNA-372 in liver cancer. *Nucleic Acids Res* **38**, 5366–5383 (2010).

110. Fineberg, D., Jandeleit-Dahm, K. A. M. & Cooper, M. E. Diabetic nephropathy: diagnosis and treatment. *Nat Rev Endocrinol* **9**, 713–723 (2013).

111. Hu, M. *et al.* Lnc <scp>RNA MALAT</scp> 1 is dysregulated in diabetic nephropathy and involved in high glucose-induced podocyte injury *via* its interplay with β-catenin. *J Cell Mol Med* **21**, 2732–2747 (2017).

112. Long, J. *et al.* Long noncoding RNA Tug1 regulates mitochondrial bioenergetics in diabetic nephropathy. *Journal of Clinical Investigation* **126**, 4205–4218 (2016).

113. Salazar-Torres, F., Medina-Perez, M., Melo, Z., Mendoza-Cerpa, C. & Echavarria, R. Urinary expression of long non-coding RNA TUG1 in non-diabetic patients with glomerulonephritides. *Biomed Rep* **14**, 17 (2020).

114. Han, R. *et al.* Upregulated long noncoding RNA LOC105375913 induces tubulointerstitial fibrosis in focal segmental glomerulosclerosis. *Sci Rep* **9**, 716 (2019).

115. Xia, W. *et al.* Long Non-coding RNA: An Emerging Contributor and Potential Therapeutic Target in Renal Fibrosis. *Front Genet* **12**, (2021).

116. Hu, S. *et al.* The long noncoding RNA LOC105374325 causes podocyte injury in individuals with focal segmental glomerulosclerosis. *Journal of Biological Chemistry* **293**, 20227–20239 (2018).

117. Wang, J. *et al.* Nuclear paraspeckle assembly transcript 1 promotes the podocyte injury via targeting miR-23b-3p/B-cell lymphoma-2 interacting protein 3 like axis. *Ren Fail* **44**, 1971–1985 (2022).

118. Su, Y., Yao, S., Zhao, S., Li, J. & Li, H. LncRNA CCAT1 functions as apoptosis inhibitor in podocytes via autophagy inhibition. *J Cell Biochem* **121**, 621–631 (2020).

119. DiStefano, J. K. The Emerging Role of Long Noncoding RNAs in Human Disease. in 91–110 (2018). doi:10.1007/978-1-4939-7471-9_6.

120. Talyan, S. *et al.* Calinca—a novel pipeline for the identification of lncrnas in podocyte disease. *Cells* **10**, (2021).

121. Ballarino, M. *et al.* Deficiency in the nuclear long noncoding <scp>RNA</scp> *Charme* causes myogenic defects and heart remodeling in mice. *EMBO J* **37**, (2018).

122. Harshil Patel *et al.* nf-core/rnaseq: nf-core/rnaseq v3.18.0 - Lithium Lynx. Preprint at (2024).

123. Felix Krueger *et al.* FelixKrueger/TrimGalore. Preprint at (2023).

124. Patro, R., Duggal, G., Love, M. I., Irizarry, R. A. & Kingsford, C. Salmon provides fast and bias-aware quantification of transcript expression. *Nat Methods* **14**, 417–419 (2017).

125. Soneson, C., Love, M. I. & Robinson, M. D. Differential analyses for RNA-seq: transcript-level estimates improve gene-level inferences. *F1000Res* **4**, 1521 (2015).

126. Love, M. I., Huber, W. & Anders, S. Moderated estimation of fold change and dispersion for RNA-seq data with DESeq2. *Genome Biol* **15**, 550 (2014).

127. Yu, G., Wang, L.-G., Han, Y. & He, Q.-Y. clusterProfiler: an R Package for Comparing Biological Themes Among Gene Clusters. *OMICS* **16**, 284–287 (2012).

128. Levitt, N., Briggs, D., Gil, A. & Proudfoot, N. J. Definition of an efficient synthetic poly(A) site. *Genes Dev* **3**, 1019–1025 (1989).

129. Ballarino, M. *et al.* Deficiency in the nuclear long noncoding <scp>RNA</scp> *Charme* causes myogenic defects and heart remodeling in mice. *EMBO J* **37**, (2018).

130. Lin, C.-Y. *et al.* Sex- and age-dependent skin mechanics—A detailed look in mice. *Acta Biomater* **175**, 106–113 (2024).

131. Gilbert, L. A. *et al.* Genome-Scale CRISPR-Mediated Control of Gene Repression and Activation. *Cell* **159**, 647–661 (2014).

132. Bester, A. C. *et al.* An Integrated Genome-wide CRISPRa Approach to Functionalize lncRNAs in Drug Resistance. *Cell* **173**, 649-664.e20 (2018).

133. Morelli, E. *et al.* CRISPR Interference (CRISPRi) and CRISPR Activation (CRISPRa) to Explore the Oncogenic lncRNA Network. in 189–204 (2021). doi:10.1007/978-1-0716-1581-2_13.

134. Denecke, B., Meyerdierks, A. & Böttger, E. C. RGS1 Is Expressed in Monocytes and Acts as a GTPase-activating Protein for G-protein-coupled Chemoattractant Receptors. *Journal of Biological Chemistry* **274**, 26860–26868 (1999).

135. Soundararajan, M. *et al.* Structural diversity in the RGS domain and its interaction with heterotrimeric G protein α-subunits. *Proceedings of the National Academy of Sciences* **105**, 6457–6462 (2008).

136. Gibbons, D. L. *et al.* Cutting Edge: Regulator of G Protein Signaling-1 Selectively Regulates Gut T Cell Trafficking and Colitic Potential. *The Journal of Immunology* **187**, 2067–2071 (2011).

137. Feng, Z. *et al.* Epithelium- and endothelium-derived exosomes regulate the alveolar macrophages by targeting RGS1 mediated calcium signaling-dependent immune response. *Cell Death Differ* **28**, 2238–2256 (2021).

138. Yuan, L., Jiang, N., Li, Y., Wang, X. & Wang, W. RGS1 Enhancer RNA Promotes Gene Transcription by Recruiting Transcription Factor FOXJ3 and Facilitates Osteoclastogenesis Through PLC-IP3R-dependent Ca2+ Response in Rheumatoid Arthritis. *Inflammation* **48**, 447–463 (2024).

139. Nayak, A. K., Das, S. L. & Misbah, C. Endothelial calcium dynamics elicited by ATP release from red blood cells. *Sci Rep* **14**, 13550 (2024).

140. Wu, N., Nishioka, W. K., Derecki, N. C. & Maher, M. P. High-throughput-compatible assays using a genetically-encoded calcium indicator. *Sci Rep* **9**, 12692 (2019).

141. Talyan, S. *et al.* CALINCA—A Novel Pipeline for the Identification of lncRNAs in Podocyte Disease. *Cells* **10**, 692 (2021).

142. Sidhom, E.-H. *et al.* Targeting a Braf/Mapk pathway rescues podocyte lipid peroxidation in CoQ-deficiency kidney disease. *Journal of Clinical Investigation* **131**, (2021).

143. Chung, J.-J. *et al.* Single-Cell Transcriptome Profiling of the Kidney Glomerulus Identifies Key Cell Types and Reactions to Injury. *Journal of the American Society of Nephrology* **31**, 2341–2354 (2020).

144. Wu, H., Kirita, Y., Donnelly, E. L. & Humphreys, B. D. Advantages of Single-Nucleus over Single-Cell RNA Sequencing of Adult Kidney: Rare Cell Types and Novel Cell States Revealed in Fibrosis. *Journal of the American Society of Nephrology* **30**, 23–32 (2019).

145. Liu, Y. *et al.* Biallelic insertion of a transcriptional terminator via the CRISPR/Cas9 system efficiently silences expression of protein-coding and non-coding RNA genes. *Journal of Biological Chemistry* **292**, 5624–5633 (2017).

146. Sterne-Weiler, T., Howard, J., Mort, M., Cooper, D. N. & Sanford, J. R. Loss of exon identity is a common mechanism of human inherited disease. *Genome Res* **21**, 1563–1571 (2011).

147. Ohno, K., Takeda, J. & Masuda, A. Rules and tools to predict the splicing effects of exonic and intronic mutations. *WIREs RNA* **9**, (2018).

148. Burset, M. Analysis of canonical and non-canonical splice sites in mammalian genomes. *Nucleic Acids Res* **28**, 4364–4375 (2000).

149. Liu, H.-X., Cartegni, L., Zhang, M. Q. & Krainer, A. R. A mechanism for exon skipping caused by nonsense or missense mutations in BRCA1 and other genes. *Nat Genet* **27**, 55–58 (2001).

150. Alfonso-Gonzalez, C. & Hilgers, V. (Alternative) transcription start sites as regulators of RNA processing. *Trends Cell Biol* **34**, 1018–1028 (2024).

151. Alfonso-Gonzalez, C. *et al.* Sites of transcription initiation drive mRNA isoform selection. *Cell* **186**, 2438-2455.e22 (2023).

152. Gil, N. & Ulitsky, I. Regulation of gene expression by cis-acting long non-coding RNAs. *Nat Rev Genet* **21**, 102–117 (2020).

153. Ganser, L. R., Kelly, M. L., Herschlag, D. & Al-Hashimi, H. M. The roles of structural dynamics in the cellular functions of RNAs. *Nat Rev Mol Cell Biol* **20**, 474–489 (2019).

154. Sauvageau, M. *et al.* Multiple knockout mouse models reveal lincRNAs are required for life and brain development. *Elife* **2013**, (2013).

155. Bonventre, J. V, Vaidya, V. S., Schmouder, R., Feig, P. & Dieterle, F. Next-generation biomarkers for detecting kidney toxicity. *Nat Biotechnol* **28**, 436–440 (2010).

156. Ferguson, M. A. & Waikar, S. S. Established and Emerging Markers of Kidney Function. *Clin Chem* **58**, 680–689 (2012).

157. Scarfe, L. *et al.* Measures of kidney function by minimally invasive techniques correlate with histological glomerular damage in SCID mice with adriamycin-induced nephropathy. *Sci Rep* **5**, (2015).

158. Deegens, J. K. J. *et al.* Podocyte foot process effacement as a diagnostic tool in focal segmental glomerulosclerosis. *Kidney Int* **74**, 1568–1576 (2008).

159. Huber, T. B. Bigenic mouse models of focal segmental glomerulosclerosis involving pairwise interaction of CD2AP, Fyn, and synaptopodin. *Journal of Clinical Investigation* **116**, 1337–1345 (2006).

160. Christensen, E. I., Wagner, C. A. & Kaissling, B. Uriniferous Tubule: Structural and Functional Organization. in *Comprehensive Physiology* 805–861 (Wiley, 2012). doi:10.1002/cphy.c100073.

161. Faivre, A. *et al.* Spatiotemporal Landscape of Kidney Tubular Responses to Glomerular Proteinuria. *Journal of the American Society of Nephrology* **35**, 854–869 (2024).

162. Ding, L. *et al.* Proximal Tubular Vacuolization and Hypersensitivity to Drug-Induced Nephrotoxicity in Male Mice With Decreased Expression of the NADPH-Cytochrome P450 Reductase. *Toxicological Sciences* **173**, 362–372 (2020).

163. Wang, S. *et al.* Massive Proteinuria-Induced Injury of Tubular Epithelial Cells in Nephrotic Syndrome is Not Exacerbated by Furosemide. *Cellular Physiology and Biochemistry* **45**, 1700–1706 (2018).

164. Nakagawa, S. *et al.* Molecular Markers of Tubulointerstitial Fibrosis and Tubular Cell Damage in Patients with Chronic Kidney Disease. *PLoS One* **10**, e0136994 (2015).

165. Ju, W. *et al.* Tissue transcriptome-driven identification of epidermal growth factor as a chronic kidney disease biomarker. *Sci Transl Med* **7**, (2015).

166. Gao, F., Cai, Y., Kapranov, P. & Xu, D. Reverse-genetics studies of lncRNAs—what we have learnt and paths forward. *Genome Biol* **21**, 93 (2020).

167. Chalak, M. *et al.* Cell Immortality: In Vitro Effective Techniques to Achieve and Investigate Its Applications and Challenges. *Life* **14**, 417 (2024).

168. Tong, W. & Zhang, H. Overexpression of long non-coding RNA WT1-AS or silencing of PIK3AP1 are inhibitory to cervical cancer progression. *Cell Cycle* **20**, 2583–2596 (2021).

169. Lv, L., Chen, G., Zhou, J., Li, J. & Gong, J. WT1-AS promotes cell apoptosis in hepatocellular carcinoma through down-regulating of WT1. *Journal of Experimental & Clinical Cancer Research* **34**, 119 (2015).

170. Zhang, Y., Fan, L.-J., Zhang, Y., Jiang, J. & Qi, X.-W. Long Non-coding Wilms Tumor 1 Antisense RNA in the Development and Progression of Malignant Tumors. *Front Oncol* **10**, (2020).

171. Menssen, H. D. *et al.* Wilms' tumor gene (WT1) expression in lung cancer, colon cancer and glioblastoma cell lines compared to freshly isolated tumor specimens. *J Cancer Res Clin Oncol* **126**, 226–232 (2000).

172. Qi, X. *et al.* Wilms' tumor 1 (WT1) expression and prognosis in solid cancer patients: a systematic review and meta-analysis. *Sci Rep* **5**, 8924 (2015).

173. Becskei, A. Positive feedback in eukaryotic gene networks: cell differentiation by graded to binary response conversion. *EMBO J* **20**, 2528–2535 (2001).

174. Lv, L. *et al.* The lncRNA Plscr4 Controls Cardiac Hypertrophy by Regulating miR-214. *Mol Ther Nucleic Acids* **10**, 387–397 (2018).

175. Zhang, Y. *et al.* Overexpression of lncRNAs with endogenous lengths and functions using a lncRNA delivery system based on transposon. *J Nanobiotechnology* **19**, 303 (2021).

176. Uthaya Kumar, D. B. *et al.* A genome–wide CRISPR activation screen identifies SCREEM a novel SNAI1 super-enhancer demarcated by eRNAs. *Front Mol Biosci* **10**, (2023).

177. Liu, S. J. & Lim, D. A. Modulating the expression of long non-coding <scp>RNA</scp> s for functional studies. *EMBO Rep* **19**, (2018).

178. Srinivas, T., Siqueira, E. & Guil, S. Techniques for investigating lncRNA transcript functions in neurodevelopment. *Mol Psychiatry* **29**, 874–890 (2024).

179. Lee, J.-K. & Bou Dagher, J. Regulator of G-protein Signaling (RGS)1 and RGS10 Proteins as Potential Drug Targets for Neuroinflammatory and Neurodegenerative Diseases. *AAPS J* **18**, 545–549 (2016).

180. Rigothier, C. *et al.* IQGAP1 Interacts with Components of the Slit Diaphragm Complex in Podocytes and Is Involved in Podocyte Migration and Permeability In Vitro. *PLoS One* **7**, e37695 (2012).

181. Kriz, W., Shirato, I., Nagata, M., LeHir, M. & Lemley, K. V. The podocyte's response to stress: the enigma of foot process effacement. *American Journal of Physiology-Renal Physiology* **304**, F333–F347 (2013).

182. Patel, J., Chuaiphichai, S., Douglas, G., Gorvin, C. M. & Channon, K. M. Vascular wall regulator of G-protein signalling-1 (RGS-1) is required for angiotensin II–mediated blood pressure control. *Vascul Pharmacol* **108**, 15–22 (2018).

183. Koehler, S. *et al.* Single and Transient Ca2+ Peaks in Podocytes do not induce Changes in Glomerular Filtration and Perfusion. *Sci Rep* **6**, 35400 (2016).

184. Tu, Y.-C. *et al.* The Physiopathologic Roles of Calcium Signaling in Podocytes. *Frontiers in Bioscience-Landmark* **28**, (2023).

185. Taylor, C. W. Regulation of IP3 receptors by cyclic AMP. *Cell Calcium* **63**, 48–52 (2017).

186. Kim, M. S. *et al.* Erythroid differentiation regulator 1 strengthens TCR signaling in thymocytes by modulating calcium flux. *Cell Immunol* **336**, 28–33 (2019).

187. Lebrun, P. *et al.* The suppressor of cytokine signalling 2 (SOCS2) is a key repressor of insulin secretion. *Diabetologia* **53**, 1935–1946 (2010).

188. Rocha-Resende, C. *et al.* Absence of suppressor of cytokine signaling 2 turns cardiomyocytes unresponsive to LIF-dependent increases in Ca^{2+} levels. *American Journal of Physiology-Cell Physiology* **312**, C478–C486 (2017).

189. Kann, M. *et al.* Genome-Wide Analysis of Wilms' Tumor 1-Controlled Gene Expression in Podocytes Reveals Key Regulatory Mechanisms. *Journal of the American Society of Nephrology* **26**, 2097–2104 (2015).

190. Filippo M. Massa *et al.* MAFB drives differentiation by permitting WT1 binding to podocyte specific promoters. *Elife* **12**, (2023).

12. Appendix

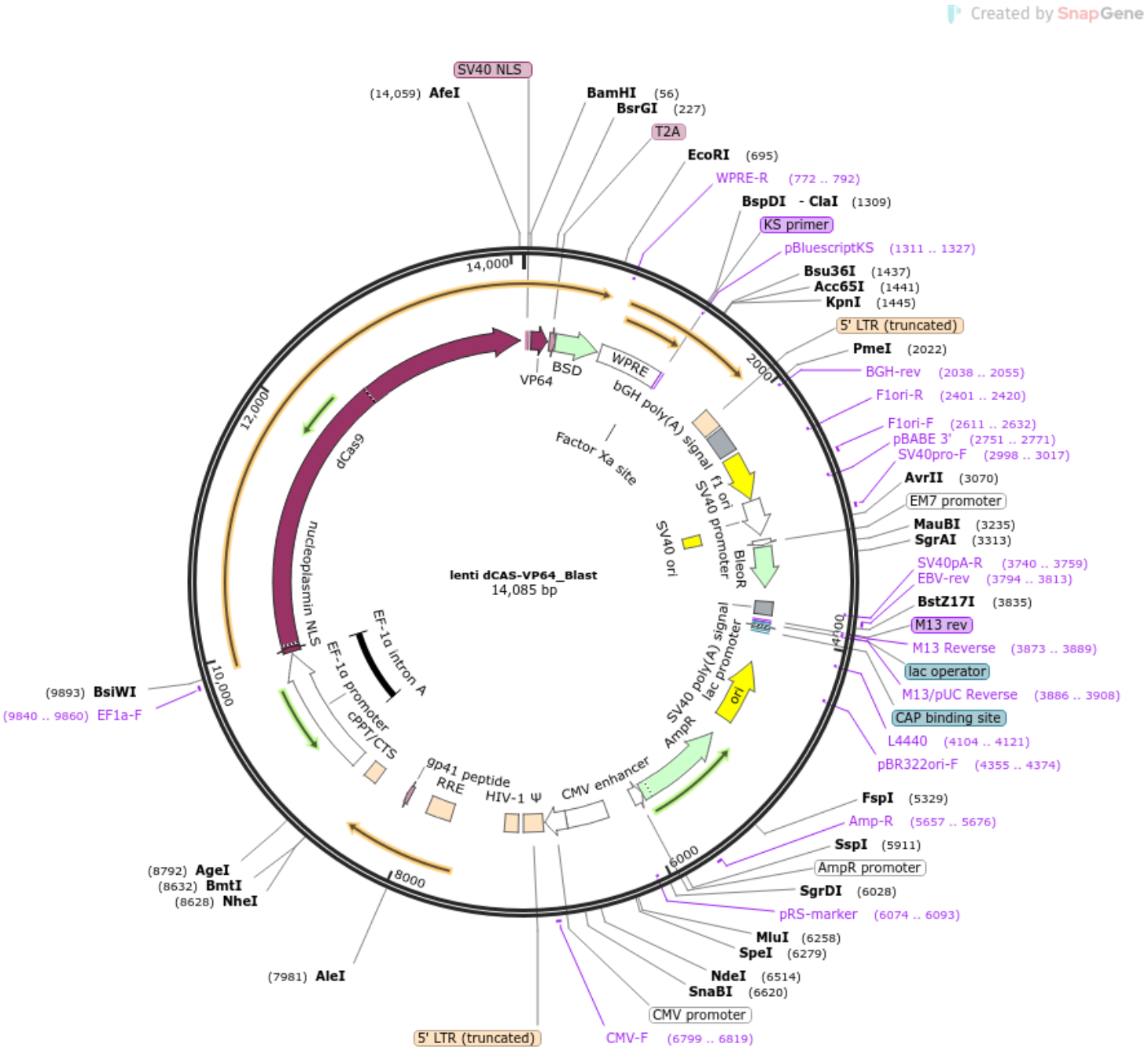

Figure A. 1 Map of pLenti6 dCAS-VP64 plasmid

3rd generation lenti vector encoding dCas9-VP64. Expression of *dCas9-VP64* in mammalian cells is driven by the EF1A promotor. Bacterial selection is enabled by expression of an ampicillin resistance gene. Mammalian selection is enabled by expression of a blasticidin resistance gene.

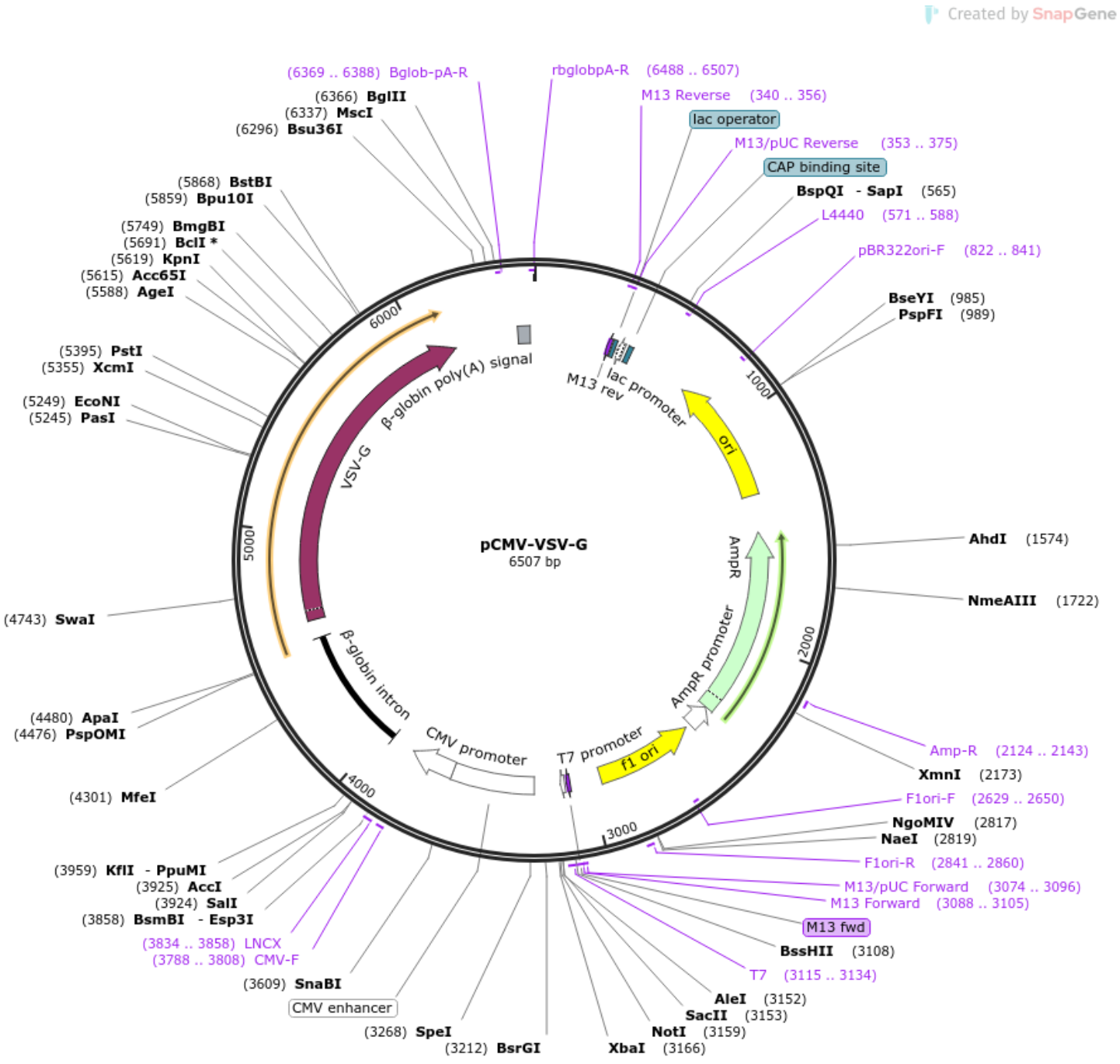

Figure A. 2 Map of pCMV-VSV-G plasmid

3rd generation lenti vector encoding for the envelope VSV-G protein for producing lentiviral particles. Expression of *VSV-G* in mammalian cells is driven by the MCV promotor. Bacterial selection is enabled by expression of an ampicillin resistance gene.

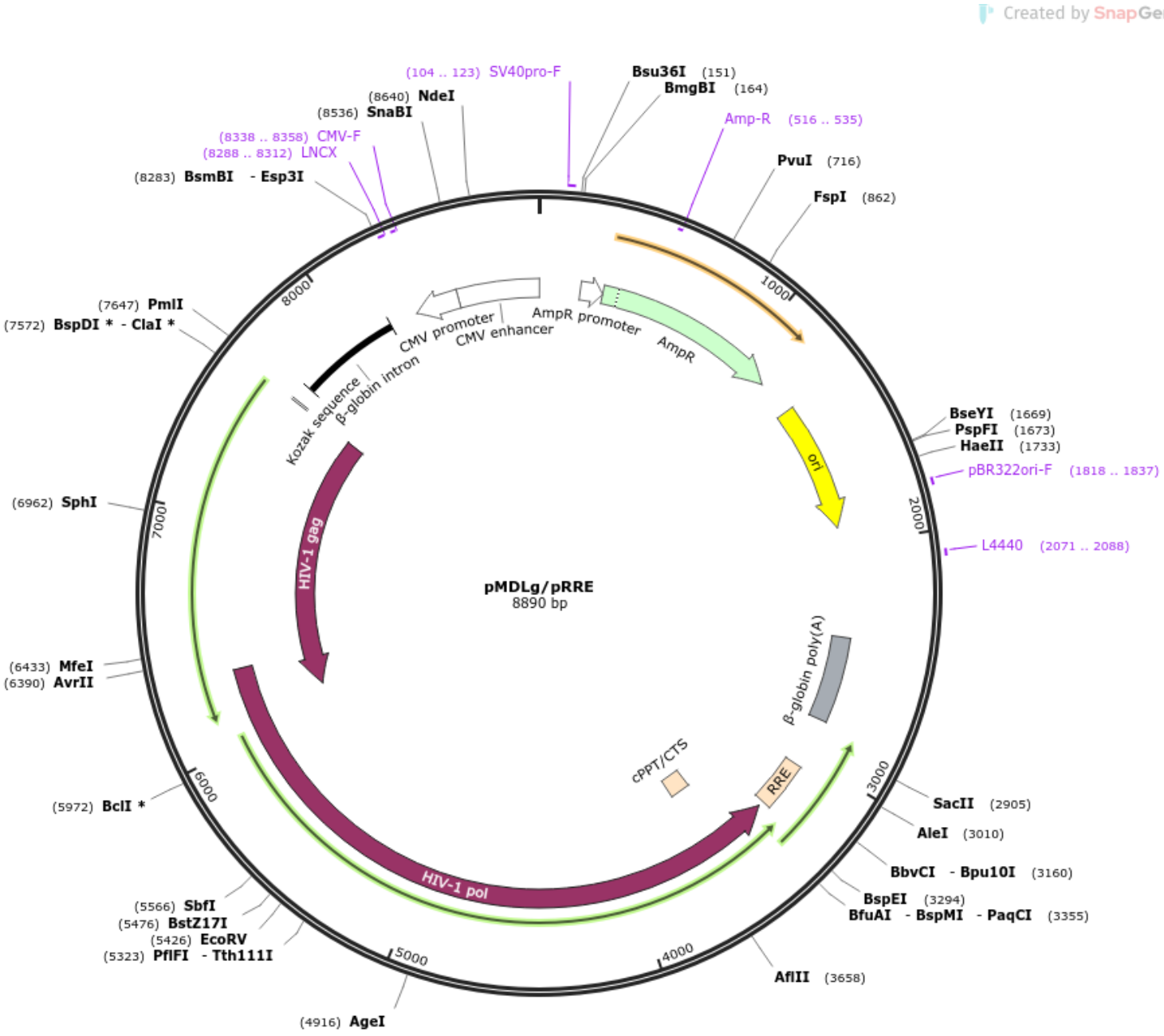

Figure A. 3 Map of pMDLg/pRRE 3rd generation lentiviral packaging plasmid.

3rd generation lenti vector encoding for *HIV-1 Gag* (virion structural proteins), *HIV-1 Pol* (retrovirus-specific enzymes), and *RRE* (Rev protein binding site facilitating export of the RNA to cytoplasm). Expression of the genes in mammalian cells is driven by the MCV promotor. Bacterial selection is enabled by expression of an ampicillin resistance gene.

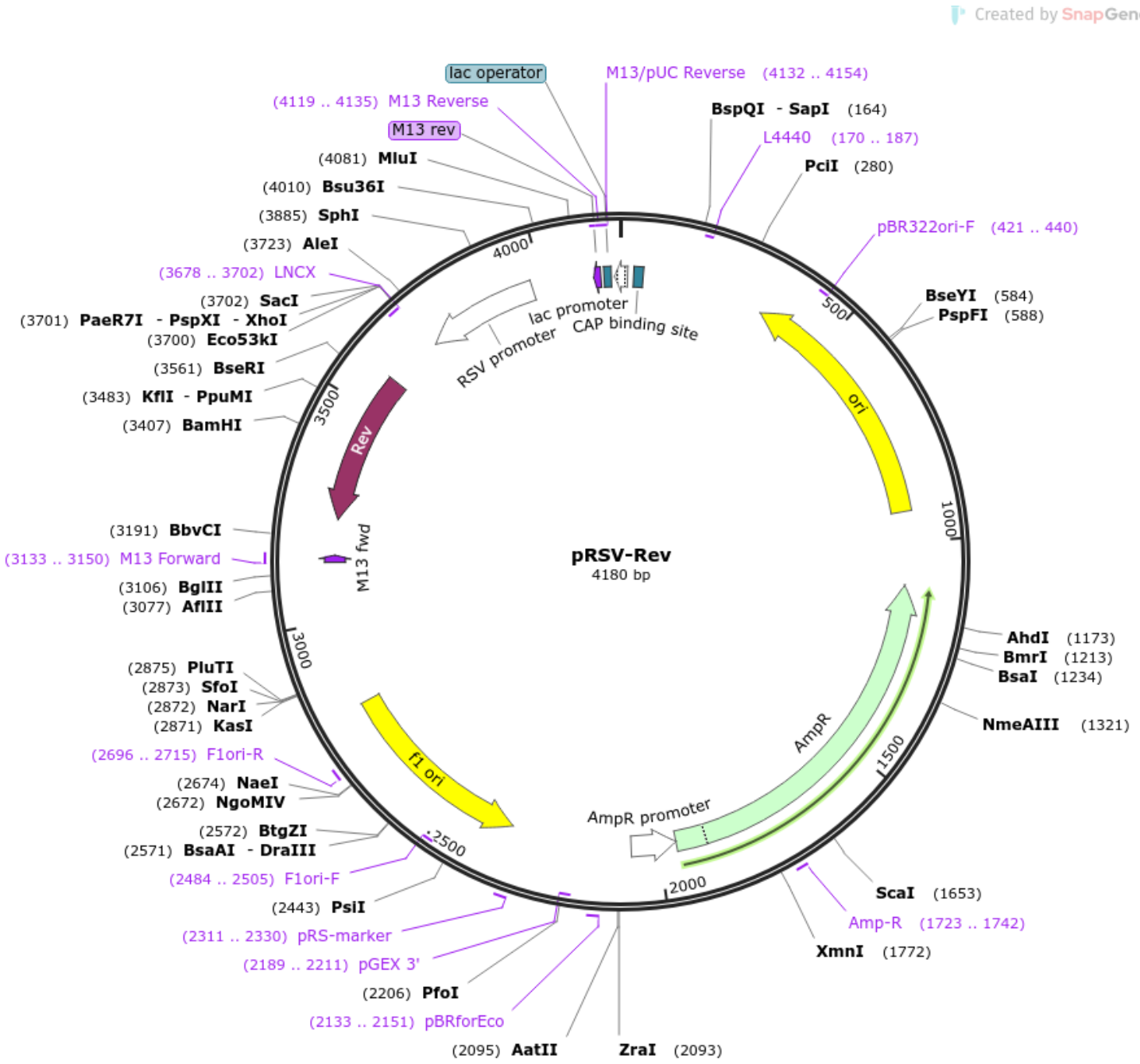

Figure A. 4 Map of pRSV 3rd generation lentiviral packaging plasmid.

3rd generation lenti vector encoding for *Rev* (Rev protein). Expression of the genes in mammalian cells is driven by the U3 promotor. Bacterial selection is enabled by expression of an ampicillin resistance gene.

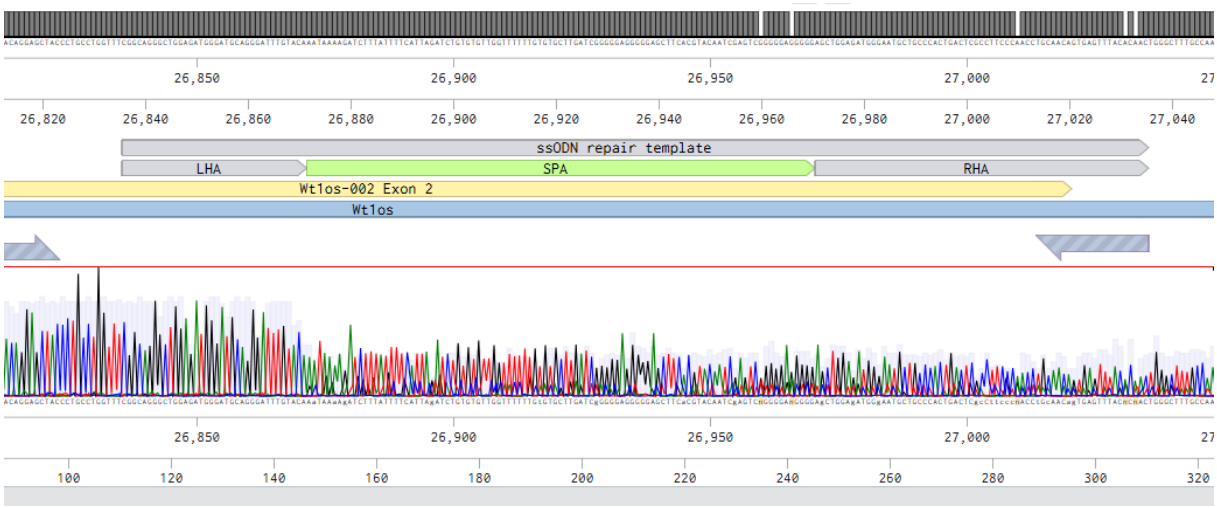

Figure A. 5. Sanger sequencing confirmed the SPA integration into the 2 exon of *Wt1os* gene.

Sanger sequencing of the genotyping PCR product confirmed the correct integration of the SPA insert in the 2 exon of the *Wt1os* gene.

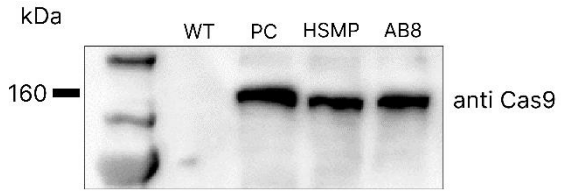

Figure A. 6. Western blotting confirmed the dCas9 expression in HSPMs.dCas9.VP64 and Moins.dCas9.VP64 cell lines.

Western blot analysis of lysates from wild-type HSMPS cells (WT), the GeneHero™ CRISPRa Stable Cell Line HEK293T.dCas9-VP64/MPH (PC), HSMPS.dCas9.VP64 (1) and Moins.dCas9.VP64 (2) cell lines shown no Cas9 band in WT cells, while both (1) and (2) samples displayed a band at the same level as the positive control (PC).